Dissertation

Enhancement of the critical heat flux in pool boiling by honeycomb porous plate and nanofluid
（ハニカム多孔質体とナノ流体によるプール沸騰限界熱流束の向上）

Graduate School of Engineering

Yokohama National University

Suazlan Bin Mt Aznam

（スアズラン　ビン　エムティ　アズナム）

March 2017

Abstract

The subject of critical heat flux (CHF) has received particular attention by many scholars due to its direct implication to safety caused by a rapid rise in wall temperature, and the sudden decreased of heat transfer coefficient that possibly jeopardizes the system. CHF enhancement is vital to increase the safety margin, for example, the in-vessel retention (IVR) method to cool down the reactor vessel during severe accidents at the nuclear power plant which requires a very high heat flux removable. This study proposes a new method of combining a few surface modification techniques to enhance the CHF further in comparison to CHF of the plain surface under saturated and atmospheric conditions. A simple method of attaching a honeycomb porous plate on a ϕ30 mm heated surface enhanced CHF about 2.5 times compared to non-modified heated surface in a saturated pool boiling of water. A significant CHF enhancement using nanofluid either as a nanoparticle deposited surface or as the working fluid have been reported by many because of improvement of surface wettability and capillary wicking performances due to surface roughness changes on the heated surface. Combination both of the methods, honeycomb porous plate, and nanoparticle deposited surface in saturated pool boiling of water show a significant CHF enhancement in all heater sizes used in the present study, 10 mm, 30 mm and 50 mm in diameter. Further enhancement of CHF with honeycomb porous plate attachment on ϕ30 mm heated surface is achieved in a high concentration of nanofluid (0.1 vol.%) boiling. The CHF was three times of that plain surface in water boiling, and surprisingly, nanoparticle deposition on the

honeycomb porous plate did not affect the liquid supply by the porous part. However, with the increased size of the heated surface, ϕ 50 mm, the same amount of enhancement (three times) could not be achieved with the combination of honeycomb porous plate attachment in the nanofluid. The idea of increasing the vapor jets by a square-shaped metal structure is adopted. Several dimensions of the metal structure were fabricated, and the best performance of it used to further the investigation. Experiment results show that a high heat flux about 3.1 MW/m^2 is removable with the combination of honeycomb porous plate and square-shaped metal structure in the nanofluid. ϕ 50 mm of the heated surface can be considered as an infinite heater surface because the dimensionless heater size of ϕ 50 mm has a value of 20. These experimental results indicate that the possibility of improving the CHF of a large heated surface by this method. Heater orientation is another primary concern in the real application because CHF tends to decrease with the increase of heater orientation approaching downward-facing surface. Experiments were conducted under saturated, and atmospheric conditions using water as a working fluid from upward-facing (0°) to the downward-facing (180°) heated surface. A small heated surface of the ceramic heater, 12 mm × 12 mm is used, and the heated surface is modified with nanoparticle deposited surface, honeycomb porous plate attachment and its combination. The experimental results show that the CHF is significantly increasing by the combination of the honeycomb porous plate attachment on the nanoparticle deposited surface, even under downward-facing heater conditions. Additionally, the CHF enhancement increases as the orientation of the heated surface approach downward-facing.

Table of contents

List of tables

List of figures

Chapter 1 Introduction

1.1 Background

Heat transfer with two-phase such as pool boiling is fond by many because an enormous amount of heat energy could be dissipated, passively, while sustaining a low surface temperature in the system. Figure 1-1 shows a typical of a pool boiling curve with increasing of wall superheat. The boiling curve is divided into four boiling regimes. There are free convection boiling, nucleate boiling, transition boiling, and film boiling. During free convection boiling (to the point A), heat transfer occurs due to the liquid is superheated and evaporates once it reaches the surface. From point A to B, isolated bubbles form at nucleation site and detach from the surface. Nucleate boiling is the most favorable regime in practicality because it sustains high cooling performance. As superheat wall increasing, the isolated bubbles join to each other and form a coalesced bubble. In regime B to C, approaching to the point C, the high rate of evaporation forms jets or columns that cover most of the heater surface. As a result, the liquid is getting harder to reach the heater surface. Point P indicates the inflection point where the heat transfer coefficient is at maximum and start to decrease with increasing of wall superheat. As superheat wall exceeds the point of C, the sudden decrease of heat flux can be seen because the heat transfer

coefficient dropped drastically. At this time vapor blanket is fully covering the heater surface acts as an insulation layer. This blanket hinders liquid to rewet the heated surface continuously. Hence, the superheat temperature rises from point C to E. Phenomena that occur between these two points is known as boiling crisis or burn out. CHF occurs at the point of C and q''_{max} is known as critical heat flux (CHF). In the case of water under saturated and atmospheric conditions, the CHF is approximately 1 MW/m^2. Critical heat flux (CHF) represents an important aspect in the boiling curve because many of the application in the real world concerns CHF. New heat dissipation technology is required to fulfill the rapid growth of heat generation in the industries, for example in nuclear power plant industries during emergency events and thermal management systems to protect electronic components. Beyond the point of CHF, the undesirable temperature arises and may affect the system's integrity.

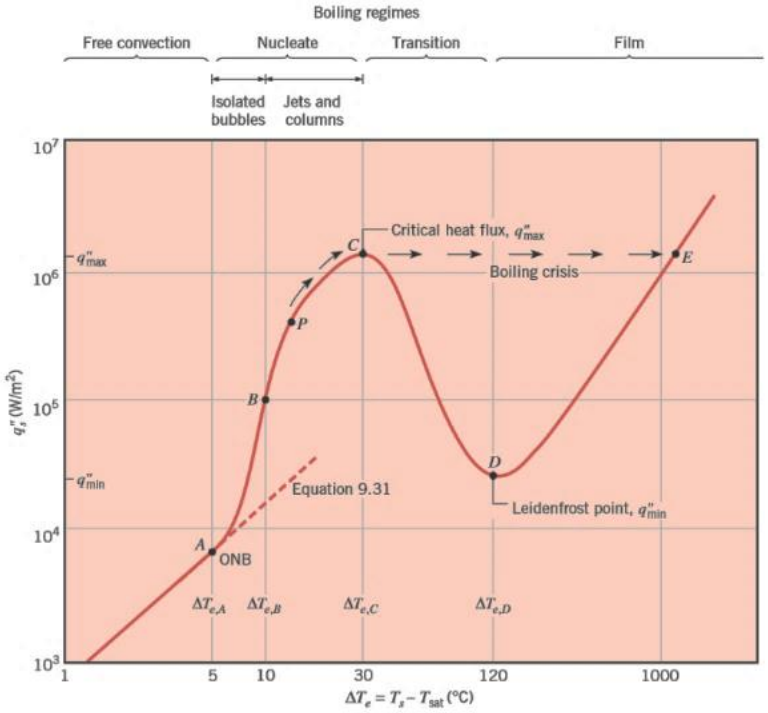

Figure 1-1 General pool boiling curve with increasing superheat temperature for water at atmospheric temperature (Incropera & DeWitt, 2007).

The CHF occurrence has brought many researchers to study its mechanism. One of the most widely known is by hydrodynamic instability theory by Zuber (1959). He develops a model analysis which considering the Helmholtz stability and the idea of Taylor critical wavelength. He postulated that continuous vapor column is accumulated on the heater surface with a diameter of Rayleigh-Taylor critical wavelength, λ_C during vigorous boiling. λ_C is defined as follows:

$$\lambda_C = 2\pi \left(\frac{\sigma}{g(\rho_l - \rho_g)} \right)^{1/2}. \tag{1-1}$$

He also considered the magnitude of λ_H to be defined as

$$\lambda_H = \frac{\pi\lambda_C}{2}. \tag{1-2}$$

The CHF is triggered when the interface of the large vapor column detaching the heated surface becomes Helmholtz unstable. From the analysis, the following CHF model is proposed.

$$q_{\text{CHF,Zuber}} = \frac{\pi}{24} p_v^{1/2} h_{fg} [\sigma g(\rho_l - \rho_v)]^{1/4} \tag{1-3}$$

This model does not account the size of heater surface condition, heater orientation, and heater size because it was developed by the assumption of the hydrodynamic of fluid, infinite, upward facing and flat horizontal surface.

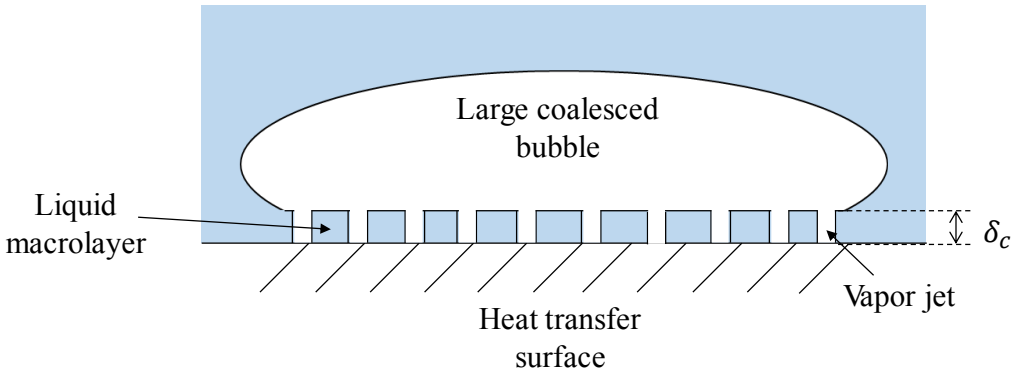

Figure 1-2 Large coalesced bubble and liquid macrolayer near CHF (Haramura & Katto, 1983).

Later on, Haramura and Katto (1983) proposed a macrolayer dryout model which considering an existence of a thin liquid macrolayer underneath a largely coalesced bubble as illustrated in Figure 1-2. The energy balance considering this situation yield an expression as below.

$$\tau_d q_{\mathrm{CHF}} A_l = \rho_l \delta_c (A_l - A_v) h_{fg} \tag{1-4}$$

where τ_d, A_l, A_v and δ_c are hovering period, the area of the liquid, the area of vapor and the thickness of liquid macrolayer. The thickness of the macrolayer, δ_c is assumed to be equal to $\lambda_H/4$. The liquid macrolayer nourishes the heater surface and immediately replaces as soon as the coalesced bubble leaves the heater surface (Figure 1-3). CHF occurs when the liquid macrolayer is completely evaporated during coalesced bubble hovering period, τ_d.

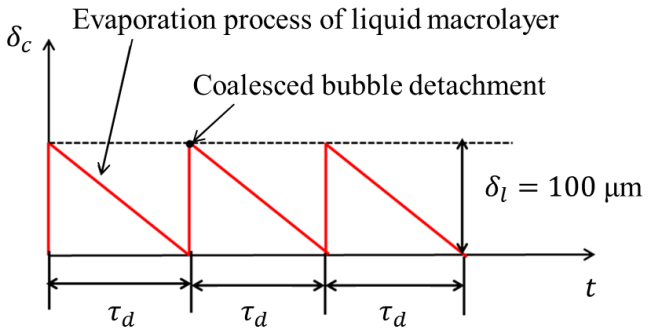

Figure 1-3 Evaporation process of liquid macrolayer versus time.

CHF model by Kandlikar (2001) unlike abovementioned model because it does not base on the hydrodynamic wave instability. He proposed a new model by considering a few forces exerted on a single bubble on the heater surface such as surface tension force, gravitational force, and momentum of the bubble. To express the forces, a physical parameter of bubble such as height and diameter of a bubble gives new factors considered in the CHF model. They are heater orientation, θ and contact angle, β of the working fluid on the heater surface. The CHF model is shown in below equation.

$$q_{\text{CHF,Kandlikar}} = h_{fg} p_v^{1/2} \left(\frac{1+\cos\beta}{16}\right)\left[\frac{2}{\pi}+\frac{\pi}{4}(1+\cos\beta)\cos\theta\right]^{1/2} \times[\sigma g(\rho_l-\rho_v)\sigma]^{1/4} \quad (1\text{-}5)$$

This CHF model is much expected as it helps to have a better understanding of the effect of heater surface characteristic and the heater orientation towards the application. Experiments were performed with different surface wettability which gives a variation of contact angle (β). The experimental results show a decrease in CHF with the increase of contact angle. However, this model only valid for the orientation of heater surface from upward facing to vertical facing heater surface. Moreover, the contact angles used in the calculation are taken from static measurements. He suggested that CHF is reached when the force of bubble interface pulling liquid parallels to heater surface is larger than the forces of holding the bubble on the heater surface.

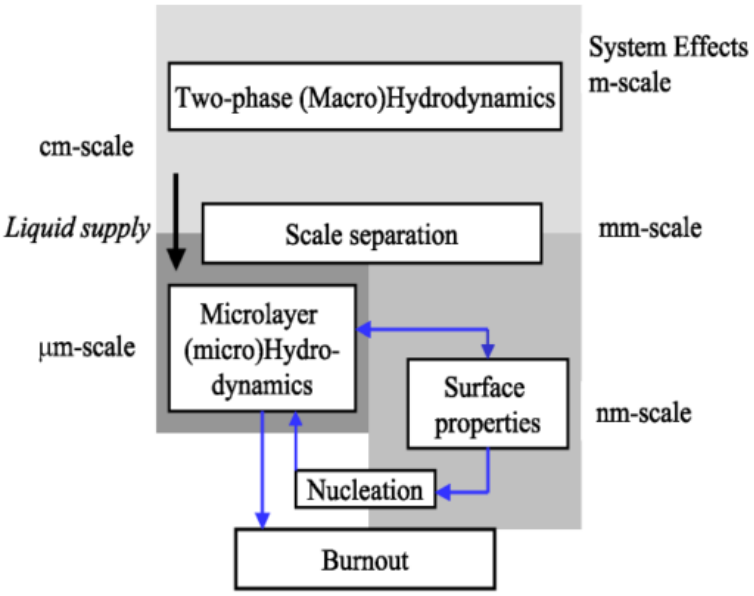

Figure 1-4 Scales and scales separation phenomenon in pool boiling

Theofanous et al. (2002).

Theofanous et al. (2002; 2002) summoned that hydrodynamics studies proposed by Zuber (1959) mainly is irrelevant to explain the CHF occurrence in pool boiling. Instead of the hydrodynamics aspect, they suggested that microlayer hydrodynamic is directly related to the burnout occurrence as shown in Figure 1-4. They conducted an extensive and thorough experiment to justify the argument by examining the behavior of dry region using infrared thermometry (IR) camera. The images from IR camera revealed the dry-hot spot is closely related to the density of nucleation site. Higher heat flux activates more nucleation sites. These nucleation sites promote rewetting process and are related to replenishment of liquid to the microlayer liquid underneath a largely coalesced bubble. As long as the rewetting process is reversible CHF does not occur. Irreversible rewetting of dry spot triggers CHF.

In 2003, Arik & Bar-Cohen formulated a CHF correlation as shown in Eq. (1-6), that depends on heater thermal effusivity and heater thickness (Eq. (1-7)).

$$\begin{aligned} q_{\mathrm{CHF,Arik}} = \frac{\pi}{24} p_v^{1/2} h_{fg} [g(\rho_l - \rho_v)\sigma]^{1/4} \times \left(\frac{S}{S+0.1}\right) \\ \times [1 + \langle 0.3014 - 0.01507 L' \rangle] \\ \times \left(1 + 0.030 \left[\left(\frac{\rho_l}{\rho_v}\right)^{0.75} \frac{c_{p_l}}{h_{fg}}\right] \Delta T_{\mathrm{sub}}\right) \end{aligned} \tag{1-6}$$

where

$$S = \delta \sqrt{\rho_{\mathrm{h}} c_{\mathrm{h}} k_{\mathrm{h}}}, \tag{1-7}$$

$$L' = \frac{L}{\sqrt{\frac{\sigma}{g(\rho_l - \rho_v)}}}. \tag{1-8}$$

The right side of Eq. (1-6) consists of four parts. The first term is CHF prediction by Zuber theoretical model. The second term considers the heater thickness and its thermal properties

where S is shown in Eq. (1-7). The third term represent the effect of heater length on CHF in terms of dimensionless heater size, L' as shown in Eq. (1-8). It is the ratio of the heater size and capillary length which can be determined by the fluids properties. The liquid supply to the heated surface is influenced by the capillary length which depends on the fluid properties such as surface tension and the density. For the case of small heater surface, liquid supply from sides or edges of heater surface or known as end effects are dominant. These end effects weaken when the heater size becomes bigger. According to Arik & Bar-Cohen (2003), if the heated surface has dimensions that are 20 times of the capillary length, the end effects could be eliminated and can be considered as an infinite heated surface. In the present study, distilled water is used, and the experiments were performed under saturated and atmospheric conditions. Under these circumstances, the capillary length has a value of 2.5 mm, and heater surface of 50 mm could demonstrate the infinite heated surface. The last term indicates the effect of subcooling on CHF. They reported that CHF reduction decreases with the increase of heater size. Figure 1-5 show the relationship between CHF and dimensionless heater size L'. It can be seen from the figure that the trend of CHF reduction with heater size is becoming constant at a certain point. Beyond this point, the CHF is not affected by the size of heater surface any longer and is said to be representing infinite heater surface size. From experimental results, the heated surface size can be regarded as infinite when L' exceeds approximately value of 20.

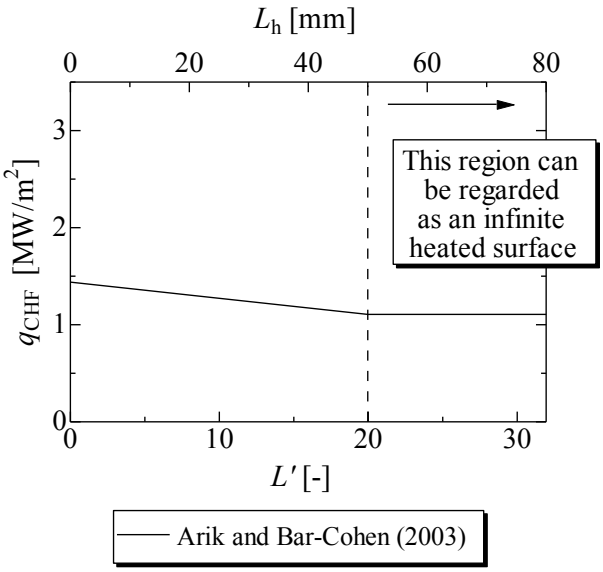

Figure 1-5 Relationship between CHF and dimensionless heater size, L'.

All literature mentioned above have a common point in which can be concluded that the failure of liquid supply to the heat transfer surface is the main reason CHF occurs. At high heat flux prior to CHF, largely coalesced bubble is generated on top of heat transfer surface.

1.2 Critical heat flux enhancement

CHF enhancement through boiling investigation can be categorized into two categories. There are a passive method and an active method. Surface modification of a heat transfer surface by nanofluid, porous layer, micro fins, egg crate attachment and, the polymer solution in a pool boiling are an effective technique for enhancing CHF passively. While active method needs an external source to create motion in the working fluid. Among well-known example in an active method is the flow boiling (external flow boiling), forced

convective boiling in a tube or channel (internal flow boiling), jet impingement, and spray cooling. In the case of external flow boiling, it combines the effects of convection and pool boiling. The higher the velocity of the working fluid, the higher the CHF and nucleate boiling heat flux will be. The jet impingement and spray cooling method are a strong combination of each method with boiling. Generally, the contact between solid and liquid is improved, and CHF is enhanced by breaking through the bubble layer. Active methods to enhance CHF is not discussing in detail as a passive method is a major work in this thesis.

From the theoretical knowledge of evaporation heat transfer, the heat flux of evaporation at the liquid-vapor interface under saturated and atmospheric conditions has a limitation (Gambill & Lienhard, 1989). The theoretical analysis yields the following equation.

$$q_{\max} \equiv \rho_g h_{fg} \sqrt{RT/2\pi} \tag{1-9}$$

where ρ_g, h_{fg} and R are density of saturated vapor, latent heat of vaporization and ideal gas constant on a unit mass basis respectively. In the case of water, under saturated and atmospheric conditions, Eq. (1-9) gives a value of 223 MW/m^2 for the theoretical maximum heat flux. However, from an experiment result of water pool boiling, the CHF is approximately 1 MW/m^2. These gaps give more margin to enhance CHF and has motivated many researchers to find method to obtain higher maximum heat flux.

Surface modification of the heat transfer surface is an effective method to enhance CHF. It could be categorized into two types of surface modification; there are by (1) porous coating or by (2) structures attached on the heated surface.

1.2.1 Porous coating

In the classification of porous coating, there are uniform porous coating and modulated porous coating. A uniform porous coating can be produced by deposition of nanoparticle onto heated surface by nanofluid, electrolytic deposition, welding or sintering. While, modulated porous coatings are coatings with periodic and vary in the layer thickness (Liter & Kaviany, 2001).

You et al. (2003) were the first introduced a novel method enhancing 200% CHF using water-based alumina nanofluid in pool boiling. Nanofluids are colloidal mixtures of a nanometer-sized particle in a base liquid. The based liquid could be water, refrigerant or a high viscous liquid such as ethylene glycol (EG), mineral oil or a mixture of different types of liquid (EG + water, ethanol + isopropanol, etc.) They hypothesize that nanoparticle deposition formed during evaporation of microlayer near the heater surface during vigorous boiling. Kwark et al. (2010) conducted a simple experiment by submerging a copper heater in an Al_2O_3 nanofluid with a single nucleation site is generated on the heated surface to demonstrate the hypothesis. A single of circular spot of the coating formed can be seen at the very same location to the nucleation site. This outcome confirmed the deposition of the nanoparticle as a result of liquid microlayer evaporation. Many researchers agree that the deposition of nanoparticle change the surface roughness and enhance CHF. This deposition which is porous-in-form enhances the wettability and the capillary wicking of liquid. Kim and Kim (2007) studied the relationship by capillary and wicking that affecting CHF. The increase of liquid supply by water absorption layer of nanoparticle deposited surface with the capillary wicking. The contact angle of a droplet is another particular of interest, where modified surface shows the contact angle is decreasing compared to the unmodified surface.

Ahn et al. (2012) modify the heated surface by anodic oxidation modification on a zirconium surface. The micro- and nanostructured surfaces absorb more water compared to the bare surface due to effective capillary wicking that enhanced CHF. They visualized the initial penetration of liquid onto a dry surface and modified surface. They mentioned that strong capillary wicking on heater surface accountable for liquid supply and it delays the appearance of dry spot region. Forrest et al. (2010) used a polymer solution to create a coating described as hydrophilic, superhydrophilic, or hydrophobic. The largest CHF enhancement is approximately 101% with the thickest and calcinated coating. However, working fluid other than pure liquid which contains particles in the order of micron or millimeter has a major concern in the real application. Some of the problems that could be highlighted are erosions of components, sedimentation of particles and blockage in the passage.

Liter and Kaviany (2001) reported a theory and experimental result of CHF enhancement by the periodically non-uniform thickness of porous-layer coatings. Figure 1-6 show the SEM images of modulated porous-layer coating from the side view on the left and the top view on the right. The diameter of 200 μm of spherical copper particles is molded into conical stacks.

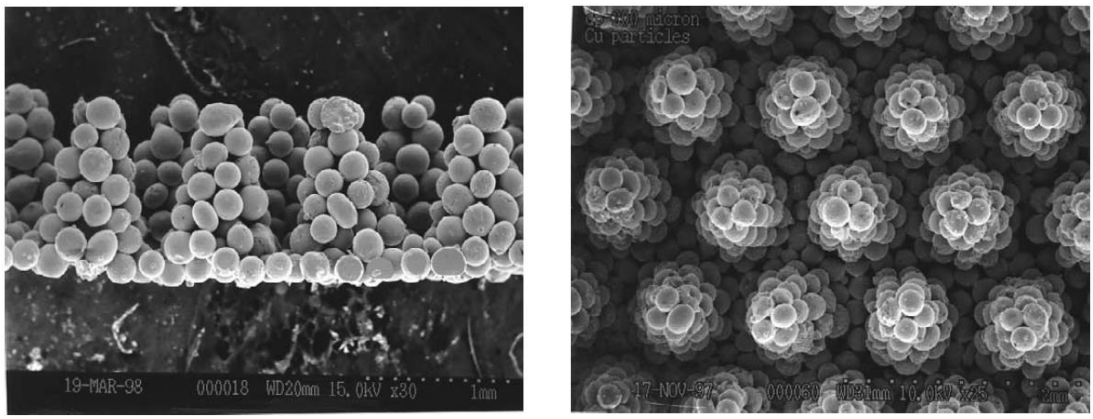

Figure 1-6 SEM images of modulated porous-layer coating from the side view on the left and the top view on the right in a conical stack (Liter & Kaviany, 2001).

The coating structures separate the path of liquid and vapor hence reducing the two-phase counterflow resistance neighboring the heated surface. They modify the Zuber hydrodynamic theory to evaluate the effect of the coating modulation-wavelength for stable vapor layer development above the heated surface.

Figure 1-7 shows an illustration of the physical model of the hydrodynamic instability limit to the liquid supply to the surface for the case of plain surface and for a surface with a modulated porous-layer coating. The modification of Zuber model gives the CHF prediction as following:

$$q_{\mathrm{CHF,h}} = \frac{\pi}{8} h_{fg} \left(\frac{\sigma \rho_g}{\lambda_m} \right)^{1/2} \tag{1-10}$$

where λ_m is a modulation wavelength depends on the macro-scale geometry. They achieved an enhancement about three times compared to a plain surface.

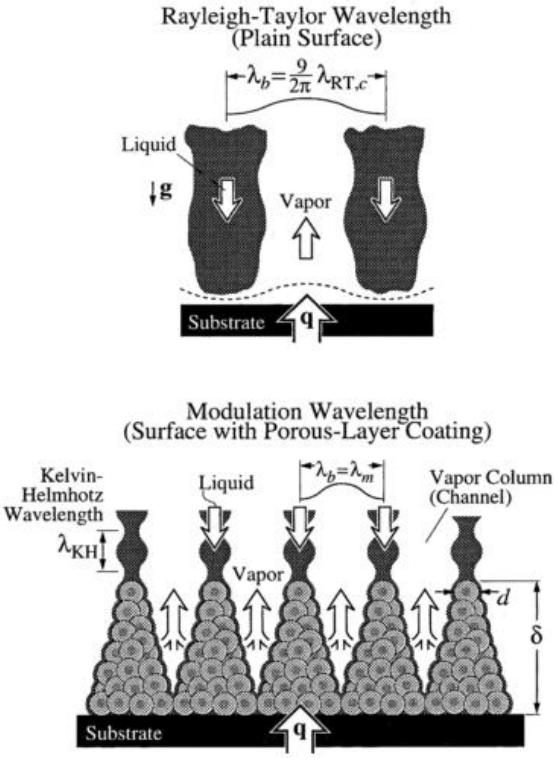

Figure 1-7 A rendering of the physical model of the hydrodynamic instability limit to the liquid reaching the surface, for a plain surface, and for a surface with a modulated porous-layer coating (Liter & Kaviany, 2001).

In another study, Mori and Okuyama studied a passive method by attaching a honeycomb porous plate on a diameter of 30 mm horizontal heated surface (Mori & Okuyama, 2009; Mori, Okuyama, & Shen, 2010). The porous plate is commercially available and widely used as a gas filtration. From experimental result, they found that with the decrease of honeycomb porous plate thickness, the CHF is significantly enhanced as shown in Figure 1-8.

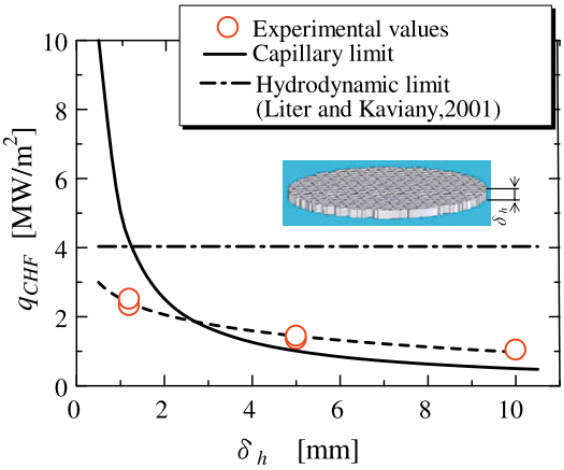

Figure 1-8 Relationship between CHF and the height of honeycomb porous plate.

The CHF of the modified surface with honeycomb porous plate thickness of 1.0 mm was approximately 2.5 MW/m^2 which is more than twice of the plain surface, 1.0 MW/m^2. They proposed a CHF model derived from a capillary limit by the porous plate, which states that CHF occurs when the maximum capillary pressure is equal to the sum of pressure loss between the two phases path. Experimental results were compared to the model, and the results are in good agreement with the calculation results. They concluded that using a honeycomb porous plate provides strong capillary suction and the separation path of liquid and vapor flow paths by vapor escape channels is the key in CHF enhancement. Heater surface area in the study is relatively large compared to the mainstream which the value of L' is 12. This method need to be demonstrated in a larger heater surface (L'>20).

1.2.2 Structures attached on heater surface

Lienhard et al. (1973) installed an egg-crate solid structure on the heated surface, and the CHF is increased about 2.36 MW/m^2. They extended the hydrodynamic instability

theory model by Zuber (1959) to consider geometry and size effect of heater surface. They proposed a CHF model to represent infinite horizontal heater surface as shown in Eq. (1-11).

$$\frac{q_{\text{CHF,Lienhard}}}{q_{\text{CHF,Zuber}}} = 1.14\frac{N_j}{A_s/\lambda_D^2} \tag{1-11}$$

where N_j is the number of vapor jet that could exist on a heater surface and A_s is an area of heater. With the aid of an egg crate the, number of vapor jet is increased. CHF is triggered when the diameter of vapor columns reaches the most dangerous wavelength λ_D (as in Eq. (1-12)). In the case of water, under saturated and atmospheric conditions, the λ_D is approximately 27 mm.

$$\lambda_D = 2\pi\left(\frac{3\sigma}{g(\rho_l - \rho_g)}\right)^{1/2} \tag{1-12}$$

They performed an experiment with a few different parameters in heater surface sizes and working fluids as well on a finite horizontal flat plate. Heater sizes vary from 8.9 mm to 21.6 mm, and working fluids are benzene, ethanol, isopropanol, and methanol. Variations in heater sizes and working fluids give an insight of relationship between CHF and heater. Additionally, they suggested that the CHF could be enhanced if the critical wavelength of the vapor column is reduced to half of the most dangerous wavelength.

Xu & Zhao (2013) used several dimensions of trapezoid-shaped copper foam fins with high pore densities to study the pool boiling heat transfer performances. The present of fin spaces reduces the bubble escaping resistance. While in another study, Yang et al. (2010) attach a copper foam by welding onto the heated surface. Both studies show a significant heat transfer coefficient and increasing the CHF. High pore densities provide large bubble

nucleation sites, however, generates a high resistance of vapor release to hamper heat transfer.

Table 1-1 and Table 1-2 provide a summary of several studies available in literature related to the effect of surface modification and the effect of nanofluid in a pool boiling. Figure 1-9 shows the current situation of CHF enhancement ratio in the literature as a function of capillary length with various surface modifications. The CHF enhancement ratio is between CHF values obtained with nanofluid boiling and water boiling. The common points for data in the figure are the usage of nanofluid to modify the heated surface conditions during vigorous boiling, and all the experiments were performed under saturated pool boiling and atmospheric conditions. A declining trend of CHF could be observed with the increase of the dimensionless heater length. A high heat flux removal with infinite heater surface should be explored.

The combination of the nanofluid and honeycomb porous plate may be the solution to increase further CHF. These two elements have shown a promising result in removing high heat flux as mentioned above. However, the CHF enhancement that considers these combinations has not been clarified yet. Furthermore, toward the application of a new cooling technology, studies should be conducted to examine the relationship between the effect of surface modification by honeycomb porous plate and nanofluid and the other effect such as heater orientation and heater sizes.

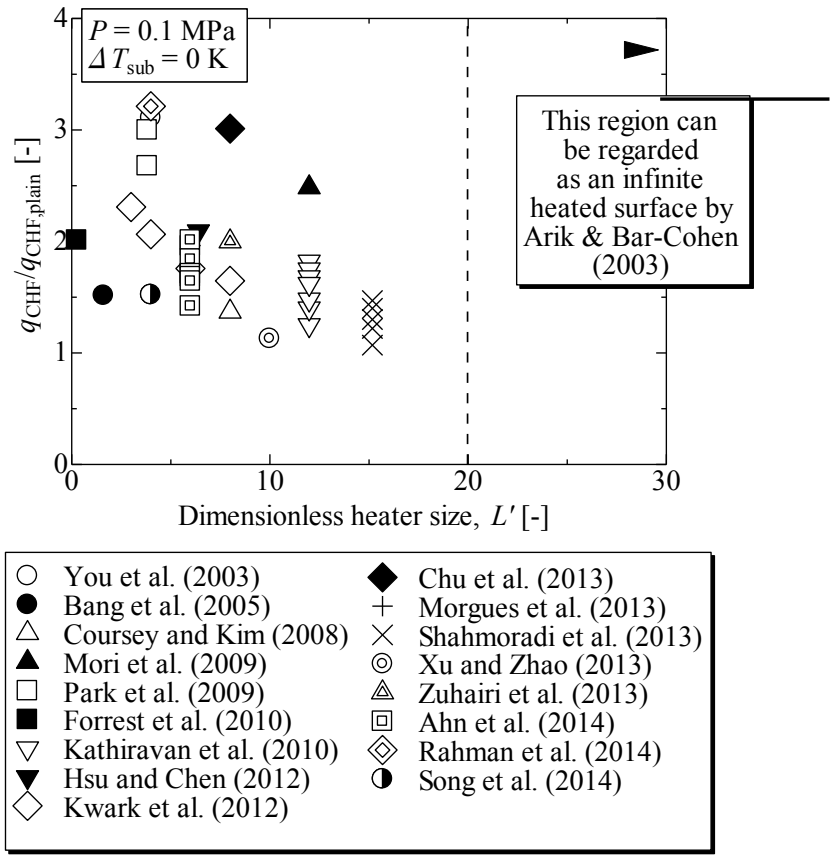

Figure 1-9 Current situation of CHF enhancement ratio in the literature as a function of capillary length with various surface modifications.

Table 1-1 Effect of surface modification

Literature	Heater (mm) Working fluid	Surface Modification	CHF_{mod} / CHF_{ref} (MW/m^2)	Remarks
Ahn et al. (2012)	25 × 15 × 0.7 Zirconium alloy bar	Micro, nano, and combination of micro-nano	1.9 / 1.0	Liquid spreading was induced by modified surface.
Rahman et al. (2014)	10 × 10 Aluminum, copper, stainless steel, gold coated silicon	Fabricated nanostructures, Microfabrication and hierarchical surfaces, CuO nanostructures	2.57 / 0.8	The relation between wicked volume flux and CHF. Best performance hierarchical with wicked volume flux 5 mm/s
Forrest et al. (2010)	0.25 Bare and coated nickel wire	Superhydrophilic thin-film coating	1.735 / 0.862	resulted in low receding contact angles related to higher CHF.
Hsu and Chen (2012)	16 × 16 copper block	Nano-silica particles coating	1.483 / 0.709	Varies the wettability by modifying surface topography. Growth bubble size on the superhydrophilic surface is

				smaller. It helps rewetting process during boiling.
Xu and Zhao(2013)	25 × 25 × 20 copper block	Trapezoid-shaped copper foam with different	1.47 / 1.3	CHF enhanced as extended surface and liquid suction capability by metallic foam
Chu et al. (2013)	20 × 20 copper	Hierarchically structured surface of copper microstructure covered with CuO nanostructure varies in surface roughness	2.5 / 0.83	The liquid supply is enhanced as roughness-augmented capillary forces increased. The best performance Cu-CuO-based (r=13.3) vs. SiO_2 smooth surface (r≈1)

Table 1-2 Effect of nanofluid in pool boiling

Literature	Heater (mm)	Nanofluid(s)	Concentration	Max. CHF_{exp} / $CHF_{water,plain}$ (MW/m^2)	Remarks
You et al. (2003)	10 × 10	Al_2O_3-water	0 g/L ~ 0.05 g/L	1.68 / 0.54	The first study reported. Trapped particles on heater surface change heating surface characteristics.
Kwark et al. (2012)	10 × 10 × 3 copper block	Al_2O_3-water	0.001 g/L ~1 g/L	2.0 / 0.3	Further increase beyond 0.025 g/L did not increase CHF
Bang et al. (2005)	4 × 100 × 1.9	Al_2O_3-water	0.5 % ~ 4 %	2.64 / 1.74	The heat transfer coefficient was decreased by increasing particle concentration.
Zuhairi et al. (2013)	ϕ20 Copper block	TiO2-water	0.004 kg/m^3 ~ 0.4 kg/m^3	2.0 / 1.0	Investigate dependency of nanofluid boiling time during the preparation of nanoparticle deposition surface. Improve surface wettability contributes to higher CHF.
Coursey and Kim. (2008)	ϕ20 Copper and copper oxide	Al_2O_3-water Al_2O_3-ethanol	0.001 g/L ~ 10 g/L	0.84 / 0.5	Reduction of receding contact angle by nanoparticle deposited surface. Interestingly oxide copper plate shows similar CHF enhancement.
Kathiravan et al. (2010)	30 × 30 × 0.44 stainless steel	Copper nanoparticles-water	0.25 wt% ~ 1 wt. %	1.54 / 1.044	Heat transfer coefficient is decreased as the concentration of nanofluid increases. Average surface roughness is reduced from 0.167 to 0.099 μm after the experiments.
Song et al. (2014)	10 × 50 × 0.4 50 × 50 × 0.4 Stainless steel	SiC-water	0.01% 0.001% 0.0001%	1.60 / 1.05 1.34 / 0.65	CHF enhancement dependent on nanoparticle concentration.
Mourgues et al. (2013)	ϕ15 mm SS 304	ZnO-water	0.01 vol.%	2.16 / 1.1	Test in distilled water with an initial coating of ZnO. The thickness of 70 μm nanoparticle layer improves porosity, capillary wicking, and wettability. However, increased wall temperature.
Park et al. (2009)	9.53 × 9.53 copper	CNTs-water	0.0001% 0.001% 0.01% 0.05%	1.50 / 0.56 1.68 / 0.56 1.40 / 0.56 0.90 / 0.56	The optimum concentration of 0.001% and CHF decrease with the increase of concentration due to CNTs were conglomerated. CNTs deposited on heater surface and decreased the contact angle.
Pham et al. (2012)	200 × 50 × 1 Stainless steel 316	Al_2O_3-water CNTs-H_3BO_3-water Al_2O_3-CNTs-water	0.05% 0.05%+10% 0.05%+0.05%	1.5 / 1.36 1.7 / 1.36 1.76 / 1.36	Noted that the CHF is for vertical orientation. Deposition of nanoparticle affects contact angle and surface roughness.

Shahmoradi et al. a(2013)	ϕ38 copper	Al_2O_3-water	0.001 vol.% 0.002 vol.% 0.02 vol.% 0.05 vol.% 0.1 vol.%	1.07 / 1.00 1.22 / 1.00 1.30 / 1.00 1.40 / 1.00 1.47 / 1.00	CHF is increased with a volume concentration of nanoparticles. Nanoparticles deposition surface acts as porous layer enhancing surface wettability and delays CHF.

The in-vessel retention (IVR) method is the latest strategy in the management of severe accidents at nuclear power stations. It is reported that high heat flux at about 4 MW/m^2 of heat removal technology is required. As far for today, the IVR concept has been implemented in the current LWRs of generation 3, for example, AP600, AP1000 by the USA and APR1400 by South Korea (Knudson et al., 2004).

(a)

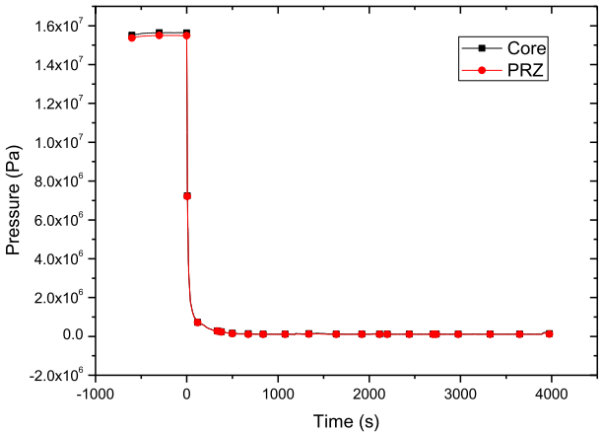

(b)

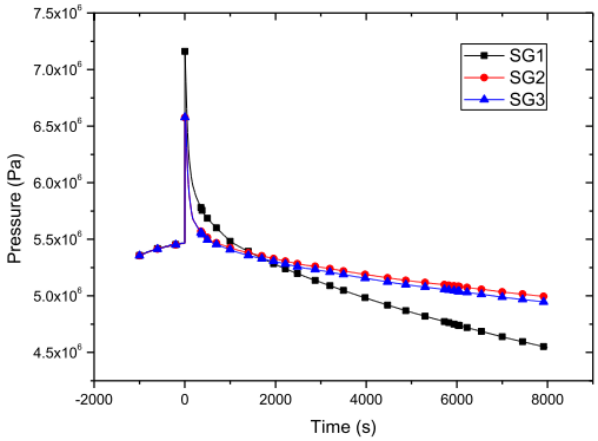

Figure 1-10 Pressure of (a) primary system and (b) secondary system during severe events started at 0 s in a pressurized water reactor (PWR) (Jin et al., 2015).

Figure 1-10 shows the pressure changes for (a) primary system (reactor core region and pressurizer), and (b) secondary system (steam generators) during severe event started at 0 s in a pressurized water reactor (PWR). Before 0 s, the normal operation of both systems are at 15.51 MPa and 5.8 MPa respectively. After 0 s, due to loss of coolant accident (LOCA) and station-black-out (SBO), the pressure dropped dramatically in the primary system. At

the same time, maximum pressured occurred up to 7.2 MPa in the secondary system and reduced gradually.

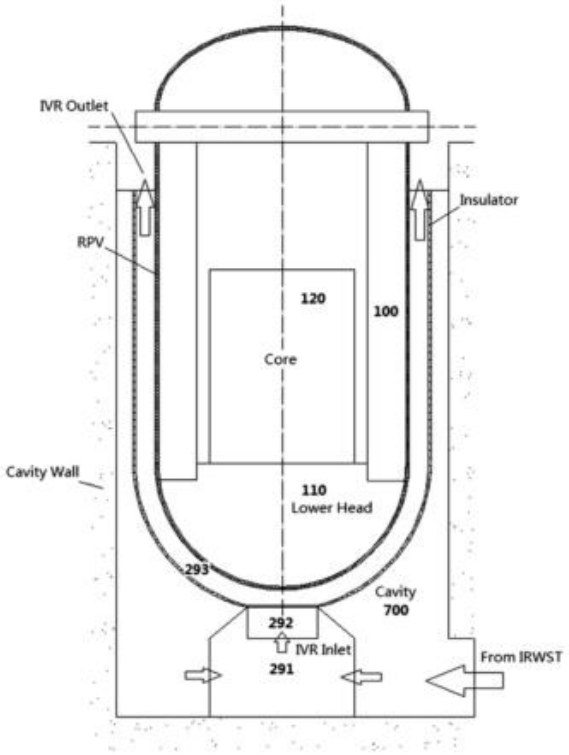

Figure 1-11 IVR flow path in a large pressurized water reactor (PWR) (Jin et al., 2015).

Figure 1-11 shows the schematic diagram of IVR flow path (Jin et al., 2015). In the event of an emergency, water is flooded into the cavity from the in-containment refueling water storage tank (IRWST) when received a safety injection signal at 6.5 s. The decay heat in the lower head is cooled by boiling and resulted in natural circulation in the cooling channel from IVR inlet due to density difference. Boiling occurred at the vertical heated surface (90°) is the most severe due to low pressure and low mass flux. According to Aoki et al. (2015), the test matrix that is designed to demonstrate the most severe case: the pressure and the mass flux are 0.1 MPa and 640 kg/(m^2s) respectively. In the present study,

the experiments were performed under a saturated and atmospheric condition in a pool boiling which can be considered as a severe condition too.

Coolability by water pool boiling has a limit, and it drops drastically at the occurrence of critical heat flux condition. Therefore, CHF enhancement is crucially essential to satisfy the demand for the cooling technology with high heat flux. Increasing the CHF is of keen interest as a method of enhancing the safety margin of nuclear power plant, particularly in IVR. (Buongiorno et al., 2009; S. D. Park, Lee, Kang, Kim, & Bang, 2012; Pham et al., 2012; Zhang, Qiu, Su, & Tian, 2010). The effect of heater surface orientation on CHF is another concern. Heat transfer surface orientation of reactor vessels in the LWRs are changing from vertical surface until it faces completely downward. Therefore, heat transfer in an inclined heater surface is a crucial consideration in the thermal management of nuclear power plant reactors during the cooling down process undertaken in response to a state of emergency. The CHF is heavily affected by the heater orientation because it is hard for coalesced bubbles generated in high heat fluxes to escape from downward-facing heated surfaces. Howard and Mudawar (1999; 1997) reported a comprehensive study on the effect of surface orientation on the CHF for a near-vertical heated surface in FC-72. They concluded that a single CHF model could not represent all heater orientations and suggested an accurate model could be developed by dividing the possible heater orientations into three regions. For a near-vertical heated surface, the CHF is triggered by the lift-off criterion, under which the wetting front is detached from the heater surface because of the difference in the interfacial curvature pressure. Conversely, for downward-facing heated surfaces, the longer hovering period of coalesced bubbles at high heat fluxes accounts for the significant reduction in the CHF. Sakashita et al. (2004; 2007; 2012; 2009) also concluded that the

vapor mass detachment period is responsible for the decrease in the CHF as the heater orientation approaches downward-facing.

1.3 Research objectives

The literature review in the previous section shows that a noticeable effect on CHF enhancement can be anticipated with the combination of honeycomb porous plate and nanofluid. However, the combined effect and the mechanism of the CHF enhancement have not been clarified yet. Therefore, the paramount objective of this study is to enhance CHF by modifying the heat transfer surface using honeycomb porous plate and nanofluid in different sizes of heater surface. In a large heater surface (ϕ 50 mm) a square-shaped metal structure is adopted to enhance CHF further. All pool boiling experiments are conducted under the saturated temperature at atmospheric in water or water-based nanofluid. The mechanism by each element of the surface modification that is contributing to CHF enhancement is studied. A parametric investigation involving variation in (a) heater size, (b) water-based nanofluid concentration, (c) dimensions of the square-shaped metal structure and heater orientation are performed.

1.4 Thesis organization

This thesis is organized as follows. It consists of five chapters including this chapter.

Chapter 1 provides an overview of the background of this study. Critical heat flux is introduced from a typical pool boiling curve, and a few prominent CHF models are presented. Literature regarding CHF enhancement by nanofluid including previous work using

honeycomb porous plate is reviewed. Issues in IVR for having marginal safety is described in this chapter as the motivation of this research. Research objectives are outlined at the end of this chapter.

Chapter 2 reports the effect of surface modification by nanoparticle deposited surface and honeycomb porous plate on CHF enhancement. The mechanism for nanoparticle deposition during boiling and factors that contribute to CHF enhancement is reviewed here. Additionally, several sizes of the heated surface were considered to examine the characteristic of hydrodynamic length. Pool boiling experiment has been conducted with three different sizes of heat transfer surface namely, 10 mm, 30 mm and 50 mm in diameter. The combination effect of honeycomb porous plate and nanoparticle deposited surface for each heater size surfaces are reported in this chapter.

Chapter 3 reports the CHF enhancement on the honeycomb porous plate attachment using nanofluid. There are two sizes of heated surface reported in this chapter, ϕ30 mm and ϕ50 mm. Pool boiling experiment with ϕ30 mm used to examine the different concentration of nanofluids with and without attachment of honeycomb porous plate. While, with a bigger ϕ50 mm heated surface, further enhancement of CHF is investigated using a square-shaped metal structure. Differences of CHF enhancement in several surface modifications by honeycomb porous plate attachment and square-shaped metal structures in nanofluids are used to examine the mechanism of CHF.

Chapter 4 reports the effect of heater surface orientation on CHF enhancement at honeycomb porous plate attachment. The experiment has been conducted using a plain surface or nanoparticle deposited surface with honeycomb porous plate attachment for each

heater surface orientation from upward-facing (0°) to downward-facing (180°). The results from the boiling configuration and rewetting investigation are used to explain the CHF enhancement.

Chapter 5 summarizes the overall works and contribution of the study in the literature. Based on the outcome of the present research, some recommendation is made for future work.

Chapter 2 CHF enhancement on the nanoparticle deposit surface attached a honeycomb porous plate

2.1 Introduction

This chapter reports the effect of surface modification by nanoparticle deposited surface and honeycomb porous plate on CHF enhancement. Figure 2-1 shows the mechanism of nanoparticle deposition on the heated surface by microlayer evaporation during the nanofluid boiling process (Kwark, Moreno, Kumar, Moon, & You, 2010). Nanoparticle which is suspended in the solvent such as water or FC-72 is accumulated on top of the heater surface when the solvent is evaporated. As the bubble detach the heated surface, it leaves the concentration of nanoparticles under the bubble. The repetition of this mechanism during vigorous boiling forms a layer of nanoparticle deposition surface. This process has been hypothesized by You et al. (2003) who was the pioneer modifying the heated surface using nanofluid. The nanocoated layer plays a major role in enhancing CHF because it enhances the surface wettability.

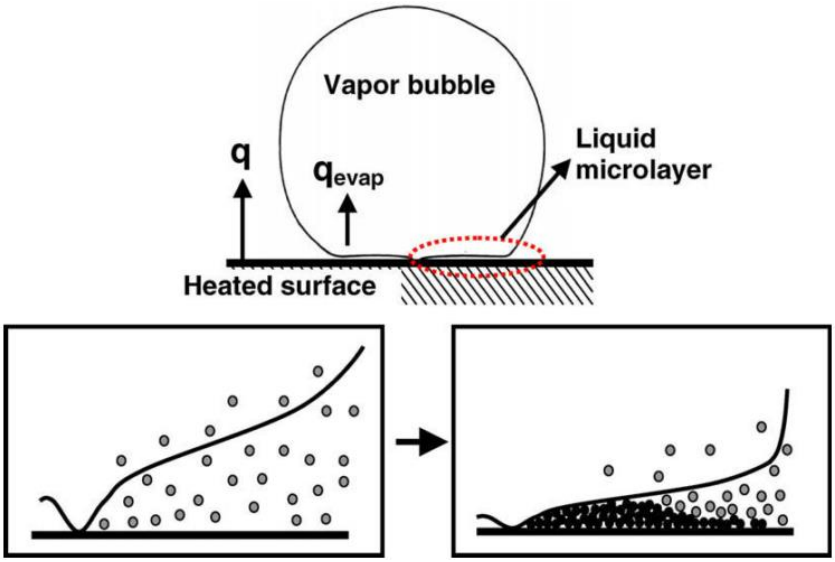

Figure 2-1 Mechanism of nanoparticle deposition on the heated surface by microlayer evaporation (Kwark, Moreno, et al., 2010).

Okawa et al. (2012) have reported the dependency of boiling time of titania nanofluid on the surface wettability and CHF. From the investigation, they found that an increase in boiling time contributes to higher CHF value and decrease the contact angle. Strong correlation between contact angle and CHF indicates nanoparticle deposition throughout the nucleate boiling was one of the main reasons of the CHF enhancement. Moreover, the boiling time required for maximum CHF enhancement were varied with the concentration of nanofluid. The lowest concentration of nanofluid (0.004 kg/m^3) needed 60 minutes while the highest concentration (2 kg/m^3) only needed 1 minute for maximum CHF. Kwark et al. (2012) also conducted an experiment with alumina nanofluid with several concentrations. However, they reported that further increase in the concentration of nanofluids (0.025 g/L) do not enhance CHF which contradicts with Okawa et al. (2012).

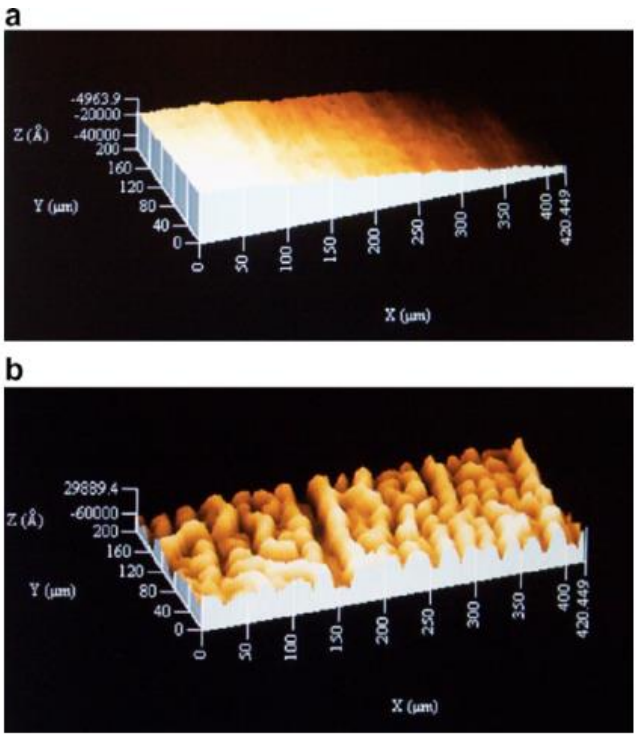

Figure 2-2 Profilometer images of the flat heater surface after boiling (a) pure water and (b) 0.01%v alumina nanofluid. The rms roughness values are ~0.1 μm and ~2 μm, respectively. Similar results were obtained with the other nanofluid (S. J. Kim et al., 2007).

Kim et al. (2007) examine the surface wettability change during pool boiling of nanofluid on CHF. They used a few types of nanoparticles such as alumina, zirconia, and silica with different nanoparticle concentration on CHF. Figure 2-2 shows profilometer images of the heated surface after boiling in (a) water boiling and (b) alumina boiling. It displays that surface boiled in pure water is smooth, while the surface boiled in the nanofluid creates a porous layer. This indicates that the surface roughness is changed due to nanoparticle deposition on the heated surface. From the analysis, the roughness and total area of the surface boiled in nanofluid are increased about twenty times and five times

respectively, compared to the heated surface boiled in pure water that contributes to CHF enhancement.

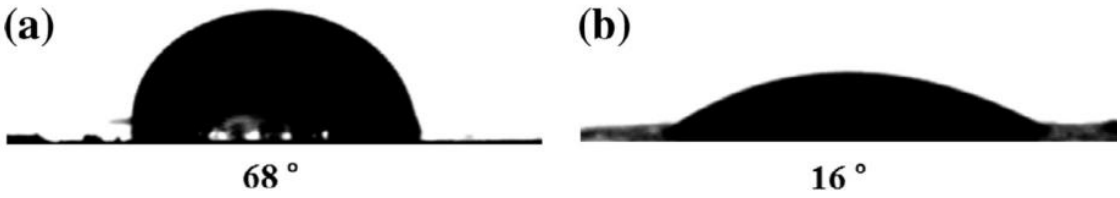

Figure 2-3 The contact angle of 1 μL water droplet: (a) plain surface and (b) after alumina nanofluid boiling (Ahn & Kim, 2013).

Ahn & Kim (2013) conducted an experiment using upward facing, 10 mm diameter of copper heat transfer surface in a saturated and atmospheric condition with alumina nanofluid boiling. Figure 2-3 shows a reduction of contact angle from 68° for the plain surface to 16° for a surface after alumina nanofluid boiling, and the CHF were 2096 kW/m^2 and 1532 kW/m^2 respectively. From high speed visualization, they found that the macrolayer on the nanoparticle-coated heater was thicker compared to the non-coated surface that enhanced CHF. Even tough they could not measure the thickness accurately, but the finding is supported by the measurement made by Sakashita (2012) using conductance probe.

The enhancement of surface wettability in the nanocoated surface can be explained using the Young equation in Eq. (2-1) and modified Young equation in Eq. (2-2) (Carey, 2008). Figure 2-4 shows interfacial tensions acting on a contact angle at equilibrium state for a smooth surface.

$$\cos\theta = \frac{\sigma_{sv} - \sigma_{sl}}{\sigma_{lv}} \tag{2-1}$$

$$\cos\theta_r = r\frac{\sigma_{sv} - \sigma_{sl}}{\sigma_{lv}} \tag{2-2}$$

Figure 2-4 shows interfacial tensions acting on a contact angle at equilibrium state for a smooth surface. There are three interfaces, σ_{sv} for between solid and vapor, σ_{sl} for between solid and liquid and σ_{lv} for between liquid and vapor.

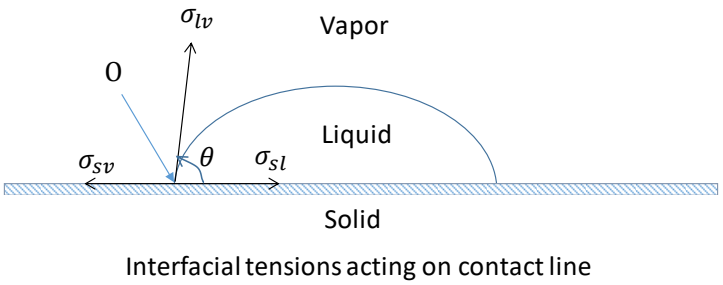

Figure 2-4 Interfacial te at equilibrium state for a smooth surface.

The difference of $\sigma_{sv} - \sigma_{sl}$ is called adhesion tension. r is the roughness area ratio which is the ratio of the actual surface area to the smooth surface area that modifies the wetting characteristics (Wenzel, 1986). θ and θ_r define as an angle between the liquid-vapor interface and solid surface of smooth surface and roughness surface respectively. Eq. (2-1) and Eq. (2-2) can be rewritten as follow

$$\cos\theta_r = r\ \cos\theta \tag{2-3}$$

r is always greater than one due to increase of effective surface area. Therefore $\cos\theta_r > \cos\theta$ indicates that θ_r is smaller than θ. The reduction of contact angle and the increase of surface area will give a rise in adhesion tension which the contact line is pulled away by σ_{sv} and spreading the liquid on the surface.

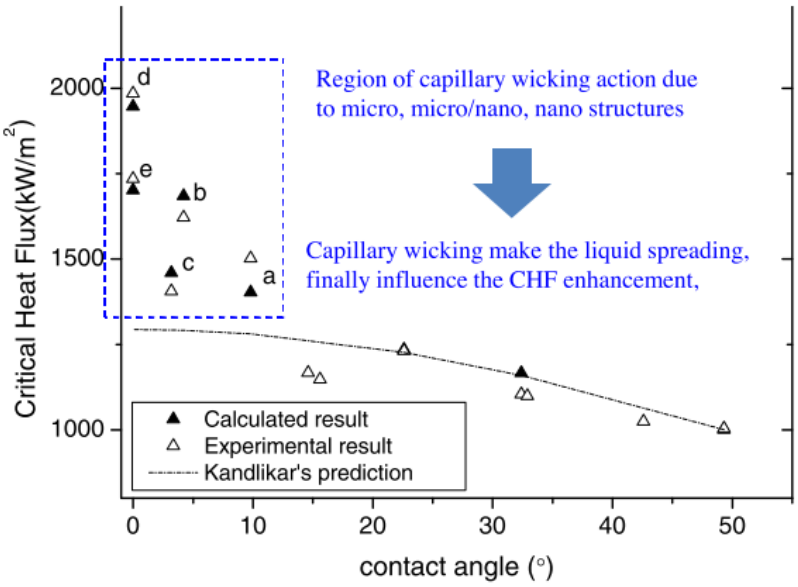

Figure 2-5 Experimental and calculated CHF values of modified surface (Ahn et al., 2012).

Ahn et al. (2012) explained the CHF enhancement of nanoparticle deposition surface by conducting an experiment to examine the effect of capillary wicking. Figure 2-5 show the experimental and calculated results of CHF values compared to Kandlikar prediction as shown in Eq. (1-5). It is evident from the figure that the prediction by Kandlikar could not explain the CHF enhancement for contact angle below 10°. The structure of the modified surface influence the liquid-spreading ability on the heated surface resulted in delaying the formation of hot spots and increasing CHF.

In spite of many studies has been conducted to enhance CHF and to understand its mechanism, a high heat flux removal from a large heated surface is another concern. Especially in the application of IVR during an emergency event in a nuclear power plant.

Therefore, pool boiling experiment considering a large heated surface is performed and reported in this chapter.

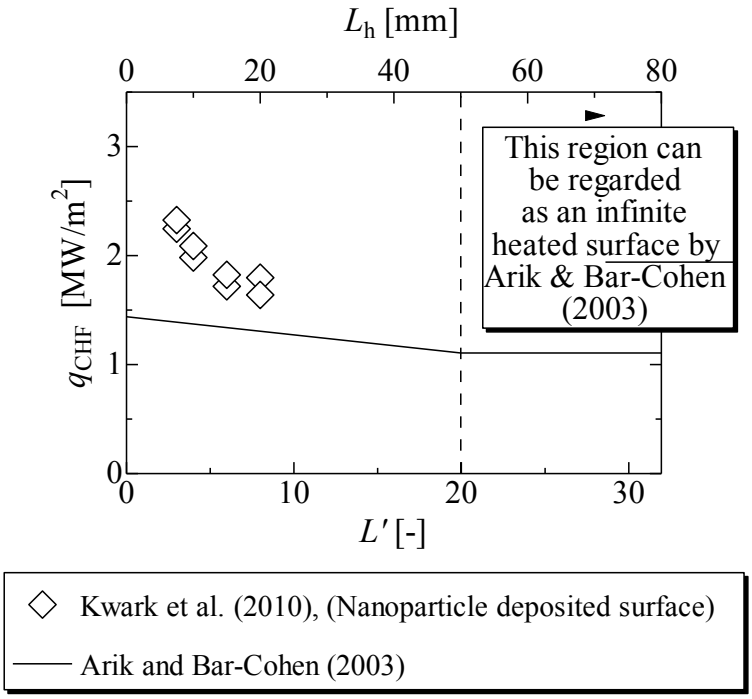

Figure 2-6 Relationship between the CHF and the size of the heated surface by Kwark et al. (2010) and Arik-Bar Cohen (2003).

Figure 2-6 show the relationship between the CHF and the size of the heated size in mm L_h and the dimensionless heater length L' for experimental results from Kwark et al. (2010) and Arik-Bar Cohen (2003). According to Arik and Bar-Cohen the CHF performance tends to decrease when the heater size is increasing. Similar finding by Kwark et al. show that even though the CHF is enhanced by nanoparticle deposited surface but the results shows that the value CHF decreases with the increase of heater surface. It is also acknowledged by Arik and Bar-Cohen (2003) that the CHF is become constant at $L'= 20$ or $L_h= 50$ mm. Beyond this points, the region could be considered an an infinite heated surface.

Therefore, in this study several sizes of the heated surface were considered to examine the characteristic of hydrodynamic length.

With the literature preview provided above, this chapter reports the effect of surface modification by nanoparticle deposited surface and honeycomb porous plate on CHF enhancement. The titania nanoparticles, TiO_2 (Aero-sil Corporation, Aeroxide TiO_2 P 25) has been used in the present study. TiO_2 is selected due to a few reasons. One of the reason because it has the property of hydrophilic which is crucial in the present study. Nanoparticle deposition forms a porous layer on the surface during the boiling. Capillary force is expected to spread the water on the heated surface. Additionally, the nanoparticle deposition improves surface wettability, and as a result, water is spread instantaneously on the heated surface. At high heat flux, when coalesced bubbles detach the heated surface, instantaneous liquid spreading on the nanoparticle deposited surface may contribute to a significant CHF enhancement. Besides metal oxide nanoparticles, the nanometer-sized (<100 nm) particles can be metallic, non-metallic, carbide, ceramics, carbonic and a mixture of different nanoparticles called hybrid nanoparticles (Sharma, Tiwari, & Dixit, 2016). However, the property of nanoparticle needs to be considered in order to expect CHF enhancement in pool boiling. The nanoparticle deposited surface could be either hydrophilic or hydrophobic nano-characteristic surfaces depending on the properties of the nanoparticles. For example, titania and silica are hydrophilic materials and graphene is hydrophobic material. In pool boiling experiment, the ability to spread liquid on the heated are extremely crucial to delay burnout to occur. Therefore, good wettability contributed by hydrophilic nanoparticle is preferable.

Additionally, several sizes of the heated surface were considered to examine the characteristic of hydrodynamic length. Pool boiling experiment has been conducted with three different sizes of heat transfer surface namely, 10 mm, 30 mm and 50 mm in diameter. The combination effect of honeycomb porous plate and nanoparticle deposited surface for each heater size surfaces are reported in this chapter.

2.2 Objectives

The objectives of experiments conducted in this chapter are listed as following:

(1) To investigate the effect of heater size on CHF in pool boiling under saturated and atmospheric.

(2) To examine the effect of surface modification by nanoparticle deposited surface, honeycomb porous plate attachment, and its combination on CHF.

2.3 Experimental apparatus and procedures

2.3.1 Experimental apparatus

A schematic diagram of the pool boiling test facility is shown in Figure 2-8. The main vessel is made of Pyrex glass and has an inner diameter of 87 mm and a height of 500 mm. The pool container was filled with distilled water to a height of approximately 60 mm above the heated surface. The heat flux was supplied to the boiling surface through a copper cylinder using electric cartridge heaters, which was inserted into the copper cylinder and was controlled by an AC voltage regulator. The heat loss from the sides and bottom of the copper cylinder was reduced using a ceramic fiber insulation material.

The top horizontal surface of a copper cylinder with diameters of 10 mm, 30 mm, and 50 mm is smooth and is used as the heat transfer surface in the experiments. An image of the freshly heated surface for a diameter of 30 mm is shown in Figure 2-7. Two sheathed thermocouples with an outer diameter of 0.5 mm were inserted horizontally to the centerline of the copper cylinder. The thermocouples (TC1 and TC2 shown in Fig. 1) in the copper cylinder were set apart axially by 6.0 mm. The closest thermocouple was located 5.4 mm below the boiling surface. These thermocouples were calibrated using a platinum resistance thermometer. The wall temperature and the wall heat flux were calculated by applying Fourier's Law, where the thermal conductivity of the copper was evaluated at the arithmetic averaged temperature of TC1 and TC2.

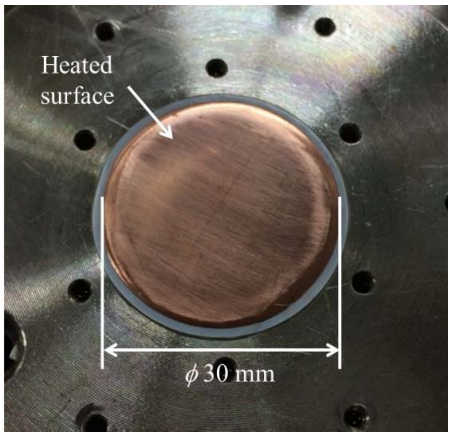

Figure 2-7 Image of a freshly heated surface for a diameter of 30 mm.

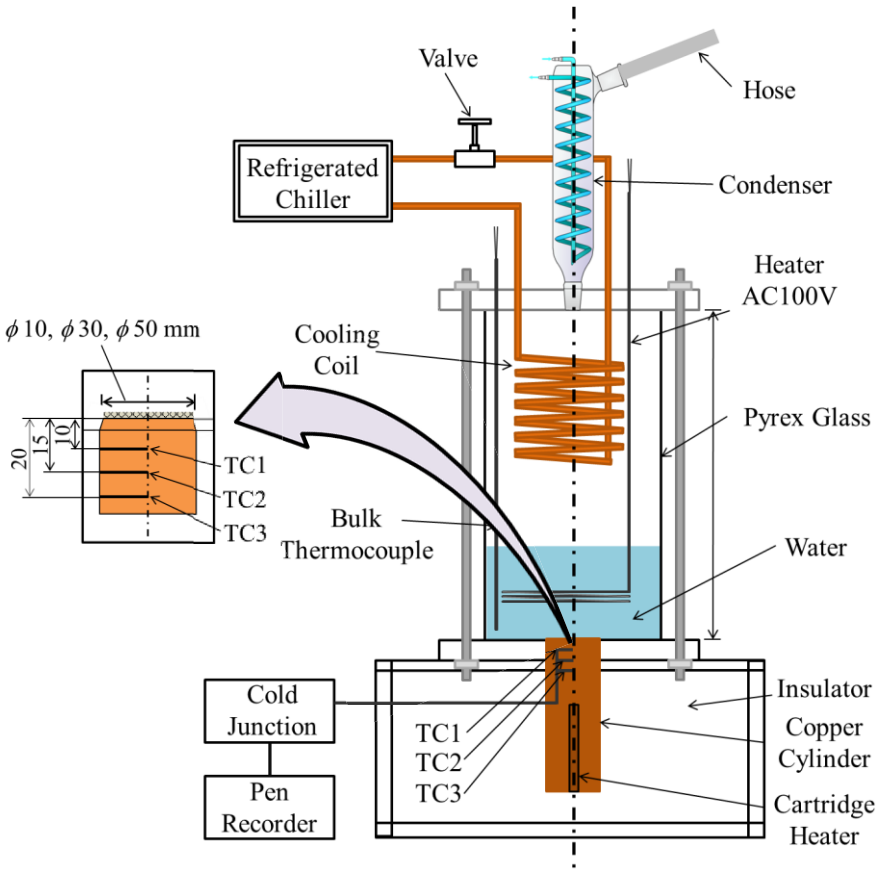

Figure 2-8 Schematic diagram of the experimental apparatus.

2.3.2 Honeycomb porous plate

The commercially available honeycomb porous plate used in the present study and a micrograph of its structure are shown in Figure 2-9. The honeycomb porous plate is commonly used as a filter for purifying exhaust gasses from combustion engines. Its constitutive ingredients are $CaOAl_2O_3$ (30–50 wt%), fused SiO_2 (40–60 wt%), and TiO_2 (5–20 wt%). The parameters of the honeycomb porous plate are listed in Table 2-1. The average, median, and maximum pore radii and the porosity obtained from the mercury penetration porosimetry are also given in Table 2-1. The pore radius distribution of the honeycomb

porous plates was measured by mercury penetration porosimetry and was found to peak at approximately 0.17 μm, as shown in Figure 2-10.

Table 2-1 Parameters for HPP

Parameter	**Value**
Vapor escape channel width (cell width) d_v	1.4 mm
Wall thickness δ_s	0.4 mm
Aperture rate	0.55
Height δ_h	1 mm
Permeability coefficient K	6.9×10^{-14} m^2
Effective pore radius r_{eff}	1.8 μm
Average pore radii	0.037 μm
Medium pore radii	0.13 μm
Maximum pore radii	0.17 μm
Porosity ε	24.8%

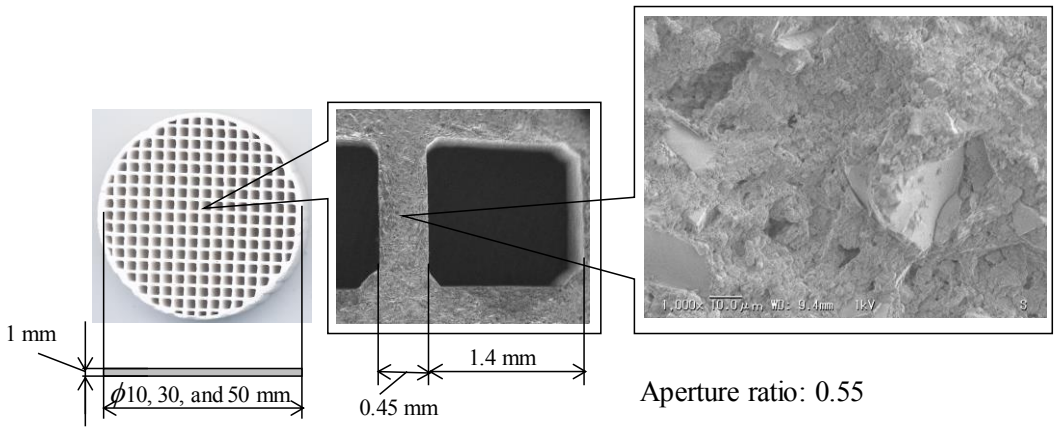

Figure 2-9 Dimensions of the honeycomb porous plate with micrograph structure.

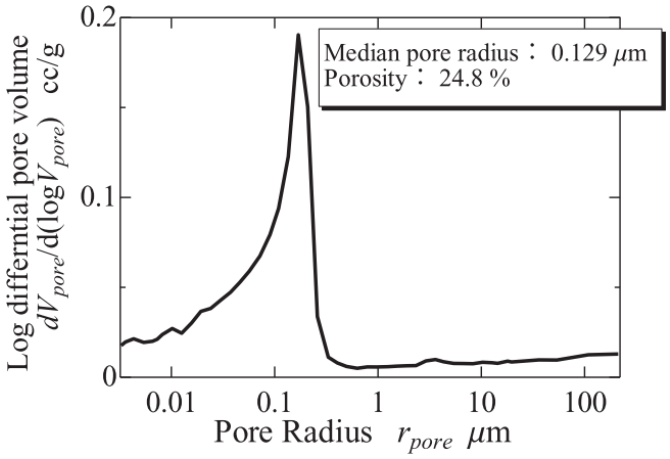

Figure 2-10 Pore radius distribution of the test porous material.

The porous plate was fixed on the top of the boiling surface by a stainless steel wire with a diameter of 0.3 mm without thermally conductive grease as shown in Figure 2-11.

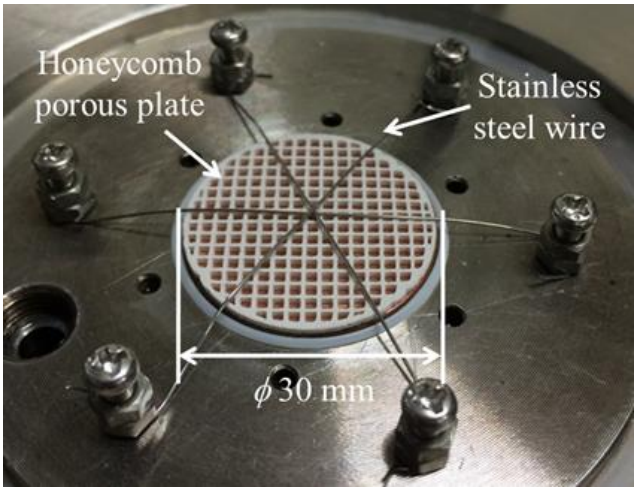

Figure 2-11 Image of surface modification by honeycomb porous plate attachment on ϕ30 mm heated surface.

2.3.3 Preparation of the nanoparticle deposited heat transfer surface

The preparation of the nanoparticle deposited surface is similar to that described in previous studies. The TiO_2 nanoparticles (Aero-sil Corporation, Aeroxide TiO_2 P 25) were selected as the test nanoparticles and were dispersed in distilled water, i.e. nanofluid. The mean particle diameter of the particle supplied by the company was approximately 21 nm. The heated surface was polished using waterproof 2000-grit sand paper and then cleaned using acetone. For preparation, 800 ml of distilled water was kept boiling in a test vessel at 500 kW/m^2 for at least 30 min. A volume of 200 ml of nanofluid which was stirred for at least four hours using an ultrasonic bath, was then added to the boiling distilled water in the test vessel. Therefore, the final nanoparticle concentration was 0.0040 wt% (volume concentration: 0.001 vol%). The time from the addition of nanofluid was set to 20 minutes to form the nanoparticle deposited surface. The reason for these conditions was that the CHF was not changed greatly under a higher concentration and a longer deposition time compared

to the present condition. Heating was then turned off, and the liquid containing nanoparticles were removed from the test vessel to prevent nanoparticles from continuously depositing on the heated surface. Figure 2-12 shows the image of nanoparticle deposited layer formed on the heated surface. Finally, the vessel was cleaned and refilled with distilled water.

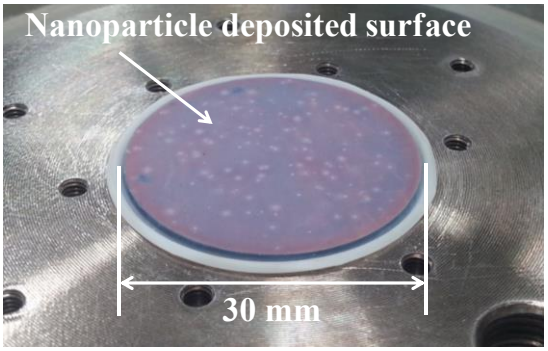

Figure 2-12 Image of nanoparticle deposited surface on a ϕ30 mm heater surface.

Figure 2-13 shows the surface roughness of the nanoparticle deposited surface which is measured using a laser focus displacement (LCD) meter, (LT-8110, Keyence Co.). The surface roughness of the nanoparticle deposited surface is on the order of ten microns, as shown in the figure. In order to know the thickness of nanoparticle deposited surface, with the same heater surface, uncoated and coated surface is prepared. Using LCD meter, the thickness of nanoparticle deposited surface is from 3 μm to 15 μm.

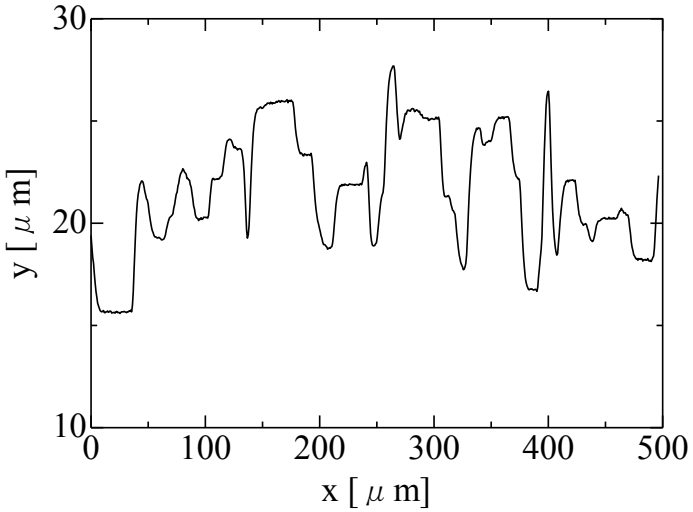

Figure 2-13 Surface roughness of the nanoparticle deposited surface.

Figure 2-14 depicts SEM images with 3500 times magnification of plain surface (#2000 sandpaper) and nanoparticle deposited surface. As can be viewed in Figure 2-14, nanoparticle deposition clearly changed the heated surface microscopically and improved the surface wettability.

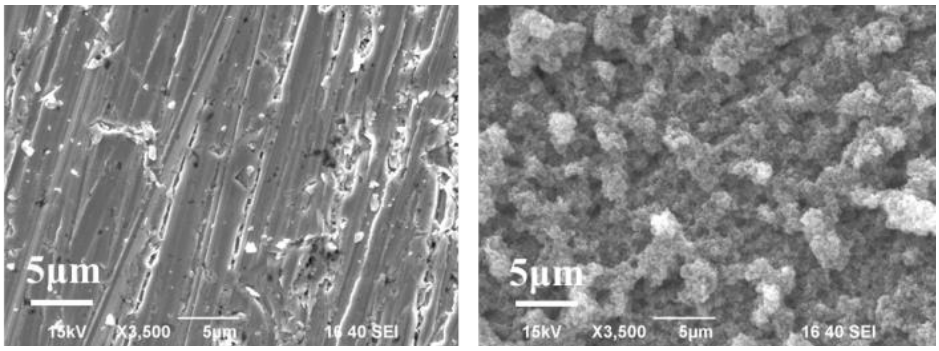

Figure 2-14 SEM images of the heated surface before (left) and after (right) the nanoparticle deposition.

2.3.4 Experimental procedure

Experiments were carried out using distilled water as a working fluid under saturated conditions at atmospheric pressure. A sheathed heater was installed above the heated surface in the liquid bath to maintain the liquid temperature at the saturation temperature. At each run, the heated surface was polished using waterproof 2000-grit sandpaper and then cleaned using acetone to minimize the effect of oxidation of heat transfer surface. The heat flux was increased in increments of approximately 0.1 MW/m^2 until burnout occurred. All measurements were performed at the steady state. The steady state was regarded as being reached when the temperatures did not change more than 0.25 K for at least 10 minutes. When burnout occurred, the heating was immediately stopped to prevent the heater and the thermocouples from being damaged. The last quasi-steady state heat flux was then measured before the transition to film boiling and was taken as the CHF.

2.3.5 Uncertainty analysis

The individual standard uncertainties are combined to obtain the estimated standard deviation of the results, which is calculated using the law of propagation of uncertainty (Taylor & Kuyatt, 1994). The uncertainties of the heat flux q, the superheat ΔT_{sat}, and the heat transfer coefficient h, respectively, are evaluated in the following equations:

$$\Delta q = \sqrt{\left(\frac{\partial q}{\partial \lambda}\Delta\lambda\right)^2 + \left(\frac{\partial q}{\partial \delta}\Delta\delta_1\right)^2 + \left(\frac{\partial q}{\partial T_1}\Delta T_1\right)^2 + \left(\frac{\partial q}{\partial T_2}\Delta T_2\right)^2} \tag{2-4}$$

$$\Delta(\Delta T_{sat}) = \sqrt{\left(\frac{\partial(\Delta T_{sat})}{\partial q}\Delta q\right)^2 + \left(\frac{\partial(\Delta T_{sat})}{\partial T_1}\Delta T_1\right)^2 + \left(\frac{\partial(\Delta T_{sat})}{\partial \delta_2}\Delta\delta_2\right)^2 + \left(\frac{\partial(\Delta T_{sat})}{\partial \lambda}\Delta\lambda\right)^2} \tag{2-5}$$

$$\Delta h = \sqrt{\left(\frac{\partial h}{\partial(\Delta T_{sat})}\Delta(\Delta T_{sat})\right)^2 + \left(\frac{\partial h}{\partial q}\Delta q\right)^2} \tag{2-6}$$

where T_1 and T_2 are the temperatures at TC1 and TC2, respectively, λ is the thermal conductivity of copper evaluated at the arithmetic mean of T_1 and T_2, δ_1 is the distance between TC1 and TC2, and δ_2 is the distance between TC1 and the boiling surface. Table 1 shows an example of the relative uncertainties calculated using Eqs. (2-1) through (2-3). As shown in Table 2-2, the relative uncertainties depend on the experimental conditions and tend to become smaller with increasing heat flux.

Table 2-2 Relative uncertainties of the measured quantities.

q [MW/m^2]	ΔT_{sat} [K]	h [kW/(m^2・K)]	$\Delta q/q$ [%]	$\Delta(\Delta T_{sat})/\Delta T_{sat}$ [%]	$\Delta h/h$ [%]
1.2	16	77	2.7	2.7	3.8
1.5	18	83	2.3	2.3	3.2
1.8	20	91	1.9	2.0	2.8
2.0	21	95	1.8	1.8	2.5

2.4 Results and discussion

2.4.1 Heater size effects on CHF by plain surface

The effect of the heater size on CHF of the plain surface was experimentally investigated under saturated and atmospheric pressure conditions. Three different sizes of heat transfer surface 10 mm, 30 mm and 50 mm in diameter were used. Heater size for ϕ50 mm can be regarded as infinite heater surface because the dimensionless heater lengths of the heater size, $L' = 19.97$ is nearly 20 can be regarded as infinite heater surface. Figure

2-15 show the relationship between the CHF and the size of the plain heated surface in mm L_h and the dimensionless heater length L'. Experimental result show that the decrease trend is similar to Arik and Bar-Cohen (2003).

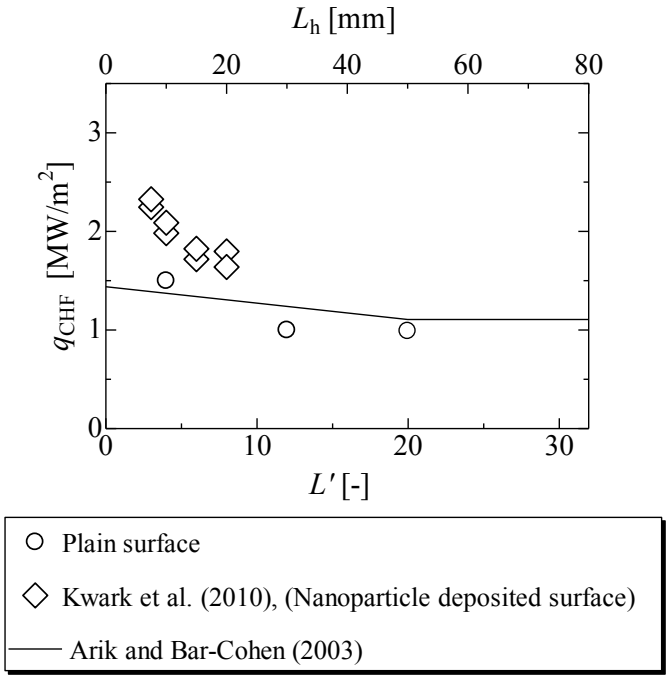

Figure 2-15 Relationship between the CHF and the size heater of the plain surface.

2.4.2 Combination effect of honeycomb porous plate attachment and nanoparticle deposited surface on CHF

Surface modification by nanoparticle deposited surface is introduced to improve the wettability of the heater surface. A combination of honeycomb porous plate and nanoparticle deposition is performed. Figure 2-16 (a) to Figure 2-16 (c) show the boiling curves for the cases with and without surface modifications, i.e., a nanoparticle deposited surface (△), a honeycomb porous plate installed on a plain surface (□), a honeycomb porous plate installed on a nanoparticle deposited surface (▼), and a plain surface (○) for surfaces having

diameters of 10, 30, and 50 mm, respectively. The arrows in Figure 2-16 correspond to the CHF condition. As shown in the figure, the CHFs of the nanoparticle deposited surfaces are higher than those of plain surfaces. The CHF enhancement for the case of the nano-coated surface is attributed to the surface wettability, surface roughness, and the capillary wicking effect due to nanoparticle deposition on the heated surface. As shown in the figure, the CHF for the case of a honeycomb porous plate, as indicated by the □ and ▼ symbols, is enhanced compared to that for the cases of plain and nano-coated surfaces (○, △). The CHF enhancements in the case of a honeycomb porous plate are due to the automatic liquid supply to the heated surface due to capillary action and the reduction of the vapor escape flow resistance due to the separation of liquid and vapor flow by the honeycomb porous structure. Moreover, it is interesting that the CHF in the case of a honeycomb porous plate installed on a nanoparticle deposited surface is higher than that for the case of a honeycomb porous plate alone on a plain surface for diameters of 10, 30, and 50 mm. The mechanisms of liquid supply to the heated surface due to a honeycomb porous plate, which are believed to be responsible for this phenomenon, are explained in the following.

Figure 2-17 shows a schematic diagram of the liquid supply mechanism in a honeycomb porous plate. In Figure 2-17, (1) and (2) depict the liquid flow caused by the capillary force and the inflow of liquid through the vapor escape channels from the top surface by gravity, respectively. The liquid is passing through the vapor escape channels from the top surface due to gravity, as indicated by (2) in Figure 2-17. Then, spreads quickly at the bottom of the vapor escape channel due to the nanoparticle deposited surface. This mechanism prevents dryout from growing on the heated surface because of good wettability and the capillary wicking effect. Consequently, the case of a honeycomb porous plate placed

on a nanoparticle deposited surface has the best performance on CHF enhancement.

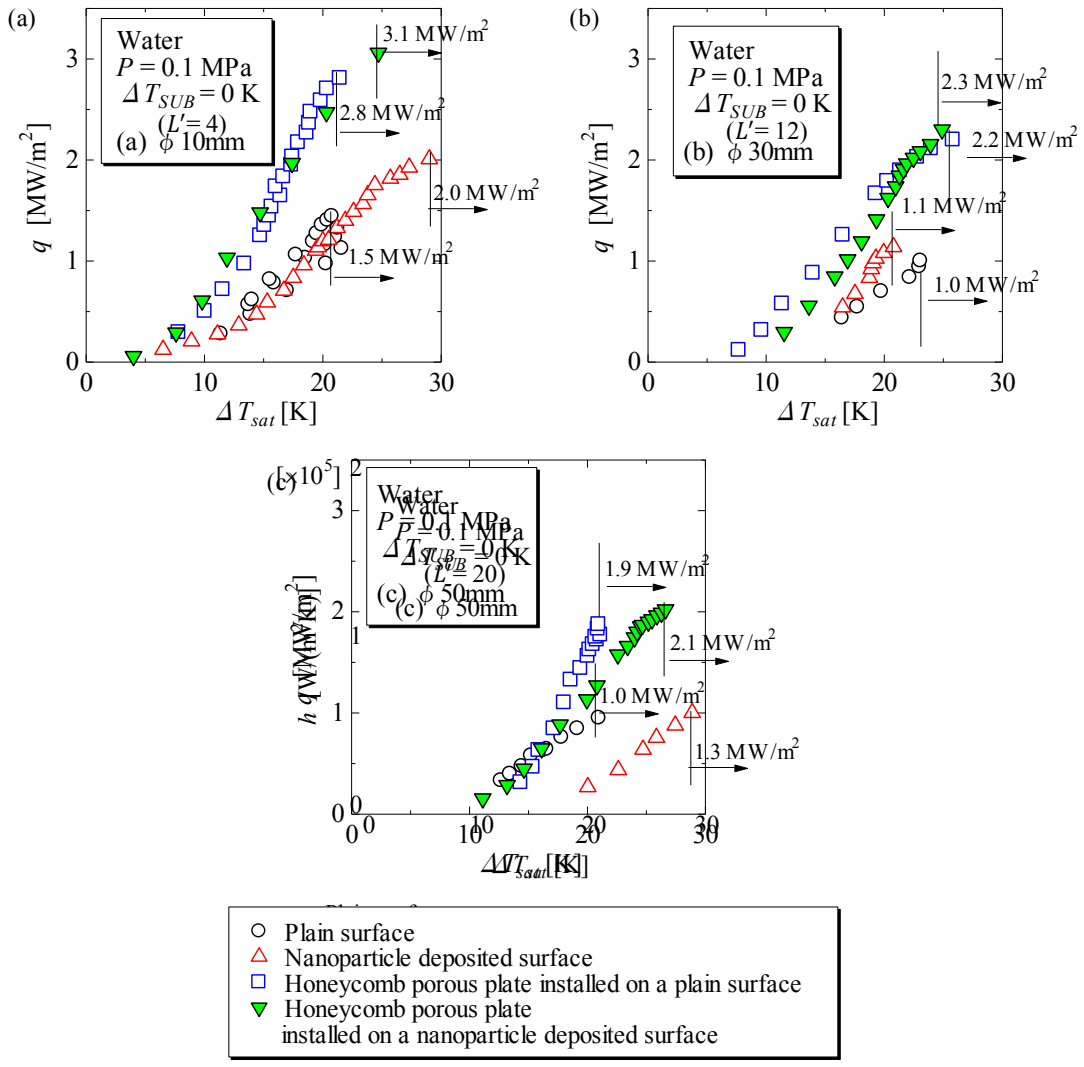

Figure 2-16 Boiling curves for different surface modifications 10, 30, and 50 mm in diameter.

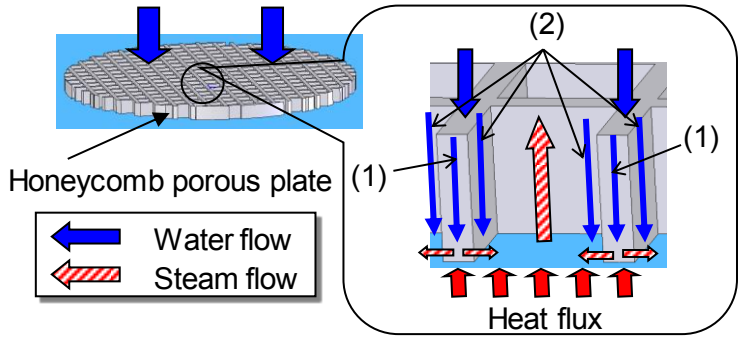

Figure 2-17 Schematic diagram of the liquid supply mechanisms to the heated surface

Fig. 4 Schematic diagram of the liquid supply mechanisms to tl
generated by a honeycomb porous plate.
heated surface generated by a honeycomb porous plate

Figure 2-18(a) to (c) indicates the heat transfer coefficient for the cases shown in Figure 2-16. As shown in Figure 2-18, the boiling heat transfer coefficients of plain surfaces and nanoparticle deposited surfaces are similar in the nucleate boiling regime except for the case of 50 mm in diameter. This tendency was also observed in a previous study (You et al., 2003). Moreover, irrespective of nanoparticle deposition occurred on the heated surface, the boiling heat transfer coefficients in the case with a honeycomb porous plate (□ and ▼) were clearly higher than those without a honeycomb porous plate (△, ○). As shown in Figure 2-17, this enhancement was caused by the honeycomb porous plate.

As stated in the introduction, nanofluids have received lots of attention because of the drastic CHF enhancement they provided. As such, some studies have proposed enhancing the IVR capability for severe accident management strategies using nanofluid. In order to establish the cooling system for IVR, the CHF must be enhanced even for a sufficiently large heated surface. Therefore, the effect of heater size on CHF enhancement is crucial for IVR.

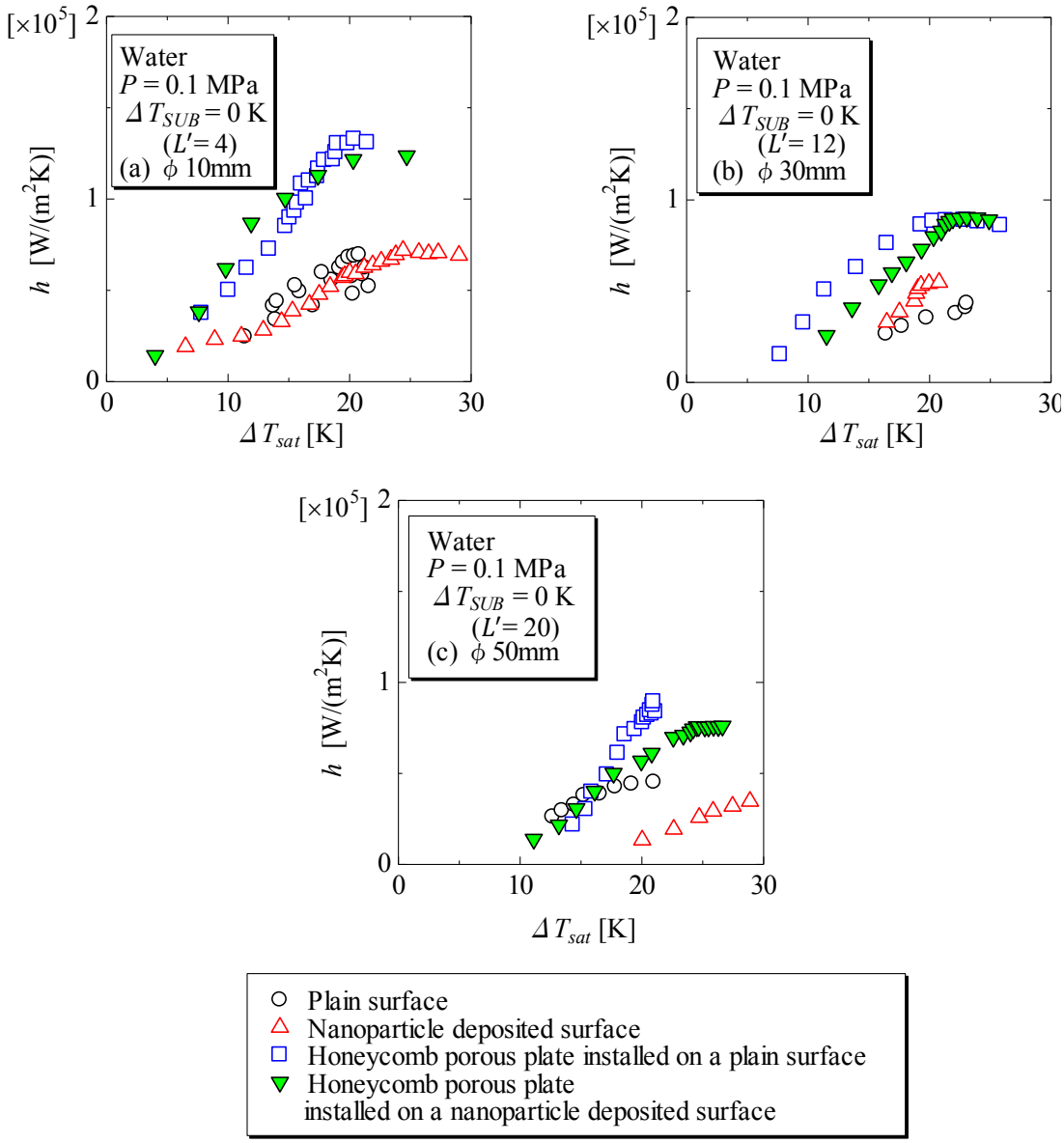

Figure 2-18 Heat transfer coefficients for different surface modifications 10, 30, 50 mm in diameter.

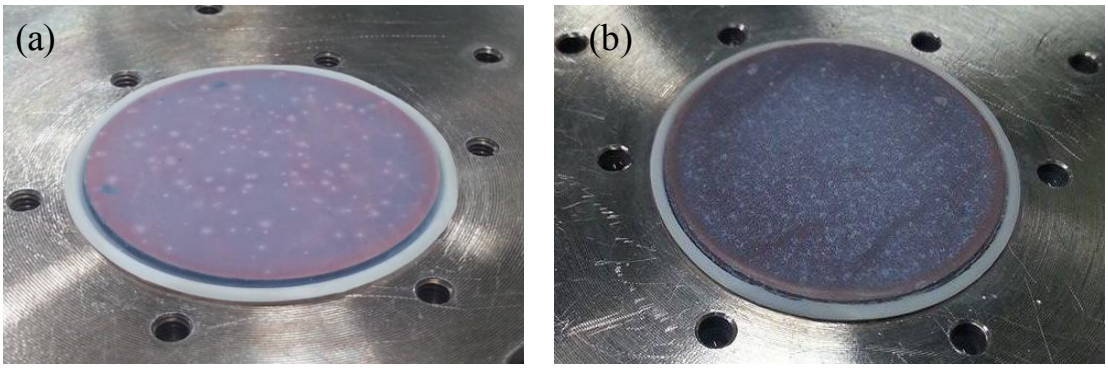

Figure 2-19 Images of the heated surface with nanoparticle deposited surface in the case of 30 mm in diameter (a) before and (b) after the CHF experiment in water boiling.

In the case of nanoparticle deposited surface in water boiling, it is noticed that the white layer is faded away after the CHF experiment as seen in Figure 2-19. This is due to vigorous boiling that detaches the nanoparticle deposition from the heated surface. From this observation, we may imply that the surface wettability is not yet optimized during the experiment because the nanoparticle deposited surface is faded away. Even though the modified surface enhances the surface wettability but the robustness of the nanoparticle deposited surface is weak. It can be easily taken away by hand. However, the experimental has been conducted properly with the same procedures, and the repeatability of the results was confirmed.

Figure 2-20 depicts the relationship between the CHF and the heater size with or without surface modifications. The values of the CHF reported by Kwark et al. (2010) are included in the figure for comparison. The CHF obtained in the present study for a diameter of 10 mm is in good agreement with the data obtained by Kwark et al. (2010). In addition, for the case of a nanoparticle deposited surface of 30 mm in diameter, the CHF extrapolated using data obtained by Kwark et al. (2010) which is shown by the broken line in the figure, is in good

agreement with the CHF for a diameter of 30 mm obtained in the present study. As shown in the figure, the CHF tends to decrease with increasing heater size for all cases. In particular, the CHF for a nanoparticle deposited surface of 30 and 50 mm in diameter was not enhanced greatly compared to a plain surface. Therefore, it is possible that a nanoparticle deposited surface alone cannot enhance the CHF when applied to a large heated surface. This is because the liquid may be pumped two-dimensionally toward the center of the heated surface due to capillary suction and wettability for smaller surfaces. On the other hand, when using a honeycomb porous plate, the CHF was enhanced compared with a plain surface (○) even for a diameter of 50 mm. Furthermore, as stated above, the CHF is enhanced in the case of a honeycomb porous plate placed on a nanoparticle deposited surface. Therefore, the strategy of combining a nanofluid and a honeycomb porous plate is suitable for high heat flux removal from a large heated surface.

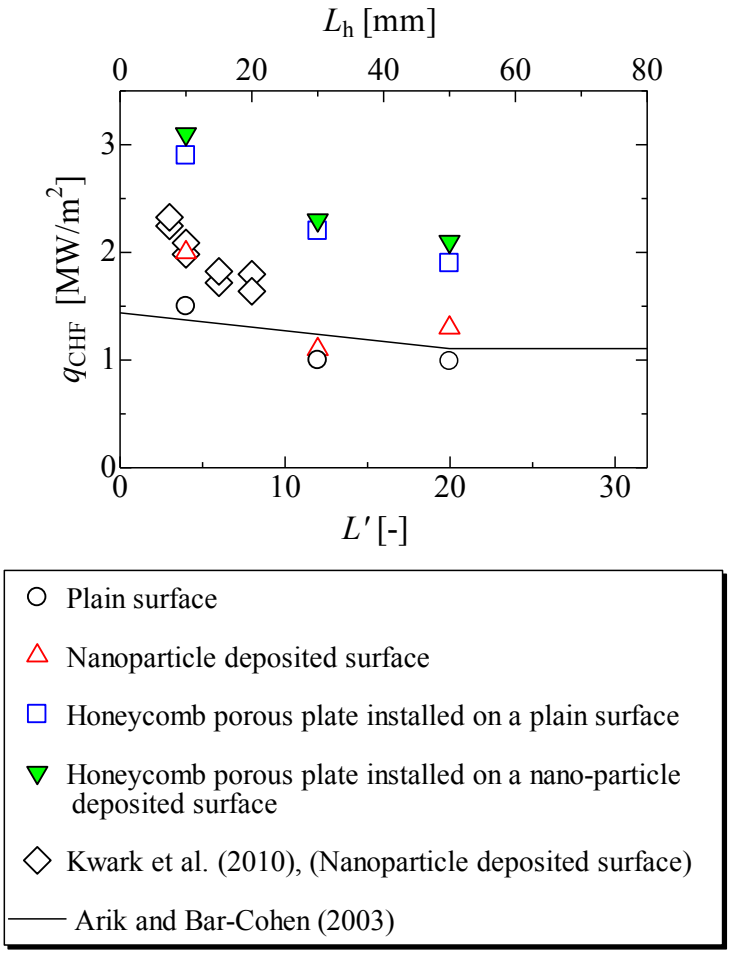

Figure 2-20 Relationship between the CHF and the size of heated surfaces with various surface modifications.

2.5 Conclusion

In this chapter, the CHF in a saturated pool boiling of water was investigated experimentally using a honeycomb porous plate and nanoparticle deposited surface. After preparation of the nanoparticle deposited heat transfer surface, a liquid containing nanoparticles was removed from the test vessel in order to prevent nanoparticles from continuously depositing on the heated surface. The vessel was then cleaned and refilled with

distilled water. The following conclusion was obtained.

(1) Nanoparticle deposition formed during vapor bubbles evaporate on the heater surface. This changes the surface roughness resulting in increasing the wettability. However, the heat transfer coefficient is degraded by the deposition surface.

(2) While honeycomb porous plate attachment shows an enhancement for both CHF and boiling heat transfer at each heater size.

(3) For each surface modification, CHF is verified to decrease with the increase of heater size. These results have been predicted earlier by rewetting resistance getting bigger with the increase of heater surface.

(4) The best performing surface modification is confirmed to be a honeycomb porous plate installed on a nanoparticle deposited surface. Under the best performing surface modifications, the CHF for 10 mm, 30 mm, and 50 mm in diameter surfaces is enhanced up to 3.1, 2.3, and 2.2 MW/m^2, respectively.

Chapter 3 CHF enhancement on the surface attached a honeycomb porous plate using nanofluid

3.1 Introduction

This chapter reports the CHF enhancement on the honeycomb porous plate attachment using nanofluid. The previous chapter demonstrated the pool boiling experiment in water with a modified surface by nanoparticle deposition surface which is prepared earlier. However, in this chapter, nanofluid is used as a working fluid. Therefore the improvement of surface wettability by nanoparticle deposition is occurring during pool boiling with nanofluid. There are two sizes of heated surface reported in this chapter, ϕ30 mm and ϕ50 mm. Pool boiling experiment with ϕ30 mm used to examine the different concentration of nanofluids with and without attachment of honeycomb porous plate. While, with a larger ϕ 50 mm heated surface, further enhancement of CHF is investigated using a square-shaped metal structure. Differences of CHF enhancement in several surface modifications by honeycomb porous plate attachment and square-shaped metal structures in nanofluids are used to examine the mechanism of CHF.

3.2 Objectives

The objectives of the experiments conducted in this chapter are listed as following:

(1) To study the effect of water-based concentration on CHF in ϕ30 mm heater size with a plain surface.
(2) To determine the CHF enhancement with surface modification by honeycomb porous plate attachment in a water-based nanofluid.
(3) To analyze the endurance performance of surface modification by honeycomb porous plate attachment in a water-based nanofluid.
(4) To investigate the single effect of several dimensions of the square-shaped metal structure attachment on a ϕ50 mm heater.
(5) To determine the CHF output by modifying heater surface with the square-shaped metal structure, nanoparticle deposited surface and honeycomb porous plate attachment in water and water-based nanofluid boiling.

3.3 Experimental apparatus and procedures

3.3.1 Experimental apparatus

The pool boiling facility is the same as used in the previous chapter. Working fluid in this experiment are distilled water and nanofluid. In the case of distilled water, the pool container was filled to a height above the heated surface of approximately 60 mm. Meanwhile, experiment with nanofluid as working fluid is detailed in the later section. In this experiment, the design of the copper block is revised to bear a high CHF estimated to

be about 4 MW/m^2. Figure 3-1 show the actual image of copper blocks and its technical drawing. A new automatic quenching system and overheating prevention device are installed. As soon as the boiling transition occurs, both devices are triggered to supply liquid water into pool boiling vessel and to stop the power heating respectively.

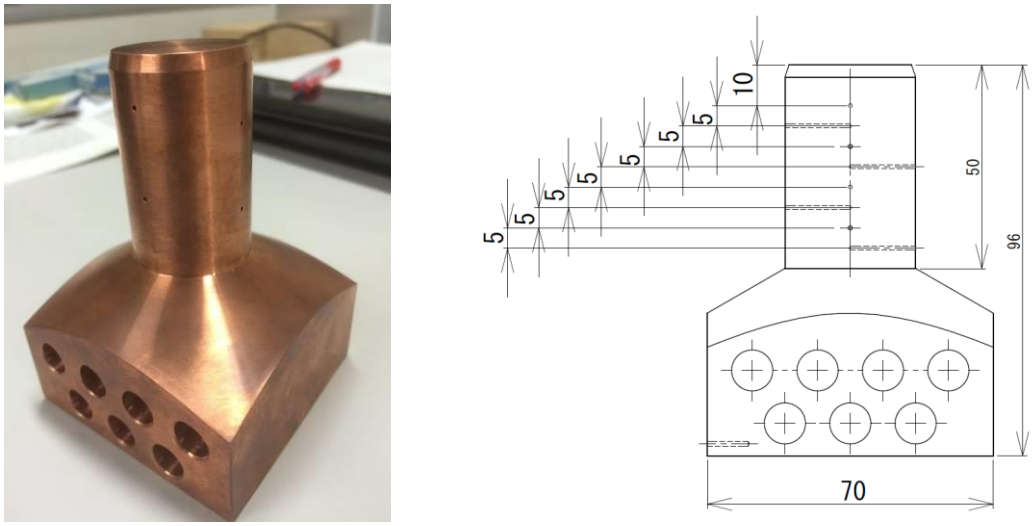

Figure 3-1 New design of copper block for ϕ 30 mm.

3.3.2 Preparation of nanofluid

Water-based TiO_2 nanofluids were prepared by dispersing dry powders into distilled water with two hours of ultrasonic vibration. No additives such as surfactants or dispersants were used to stabilize the nanoparticle suspensions. The concentrations of nanofluid were 0 vol.% (0 g/L), 0.001vol.% (0.04 g/L), and 0.1 vol.% (4.0 g/L). Figure 3-2 shows images of water-based TiO_2 nanofluid with (a) 0.001 vol.% (0.004 g/L) and (b) 0.1 vol.% (4.0 g/L) in pool boiling vessel.

(a) (b)

Figure 3-2 Images of water-based TiO_2 nanofluid with (a) 0.001 vol.% (0.004 g/L) and (b) 0.1 vol.% (4.0 g/L) in pool boiling vessel.

3.3.3 Square-shaped metal structure

The square-shaped metal structure (later is known as SMS) is made of 0.3 mm sheet stainless steel. Several different dimension of SMS is prepared to investigate the effect of heights and cells width size. In the case to examine the effect of heights, the width of each cell is fixed to 11.36 mm and the heights were varying from 1 mm, 10 mm, 25 mm and 60 mm. On the other hand, three different cells width sizes, 5.6 mm, 11.3 mm and 22.5 mm with the same height of 25 mm were prepared to look at the effect of cells width size on

CHF. Images of SMS are shown in Figure 3-3 and Figure 3-4, respectively. The best performance of SMS is selected to use in the nanofluid boiling experiment.

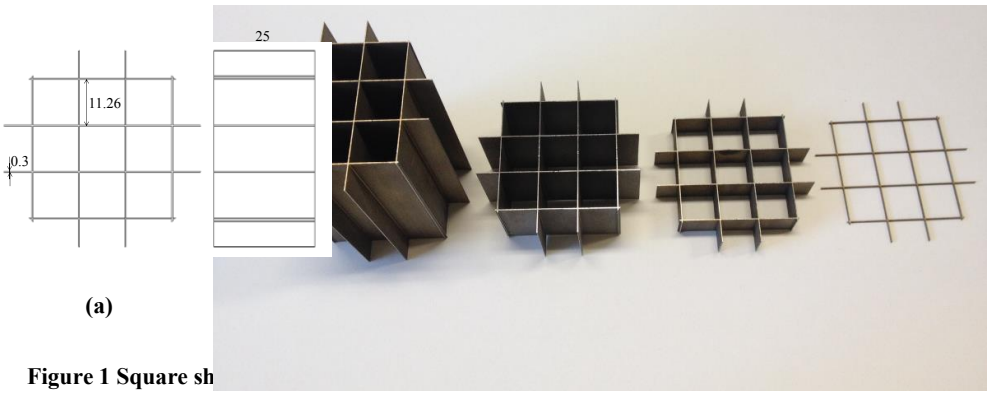

Figure 1 Square sh

Figure 3-3 Square-shaped metal structure with (a) dimension of cell width and thickness (b) different heights from left to right, 60 mm, 25 mm, 10 mm and 1 mm.

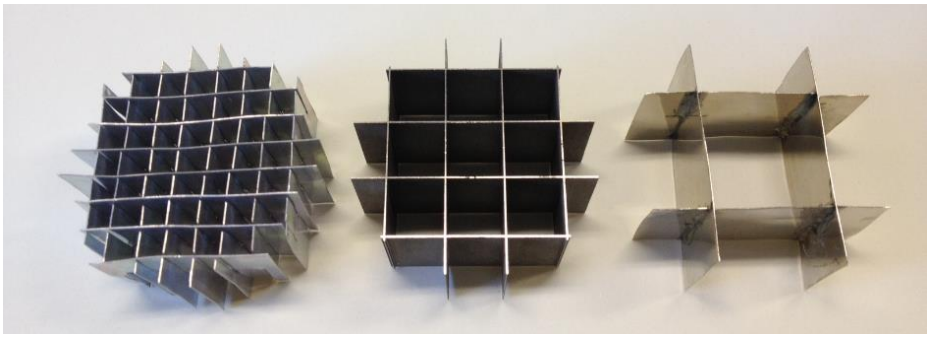

Figure 1 Square-shaped metal structure with different cell size from left to right, 5.6 mm, 11.3 mm

Figure 3-4 Square-shaped metal structure with different cell size from left to right, 5.6 mm, 11.3 mm and 22.5 mm with the same height.

3.3.4 Experimental procedures

Experiments were carried out using distilled water or nanofluid as a working fluid under saturated conditions at atmospheric pressure. Surface modifications in the present study are shown in Figure 3-5, namely (a) unmodified surface; plain surface (PS) and (b) nanoparticle deposited surface (NDS), (c) honeycomb porous plate attachment and (d) attachment of

square-shaped metal structure on honeycomb porous plate. A sheathed heater was installed above the heated surface in the pool boiling vessel in order to maintain the liquid temperature at the saturation temperature. For each run, the heat flux was increased in increments of approximately 0.1 MW/m^2 until the CHF condition is reached. The boiling transition is defined as TC1 rapidly increasing to more than 300 °C. All of the measurements were performed in the steady state, which was regarded as being reached when the temperatures did not change more than 0.25 K for at least 10 minutes. When the CHF condition is reached, the heating was immediately stopped to prevent damage to the heater or thermocouples. The final heat flux in the quasi-steady state was then measured before the transition to film boiling and was taken as the CHF. All of the measurements were taken only for increasing heat flux, and the effects of hysteresis were not considered.

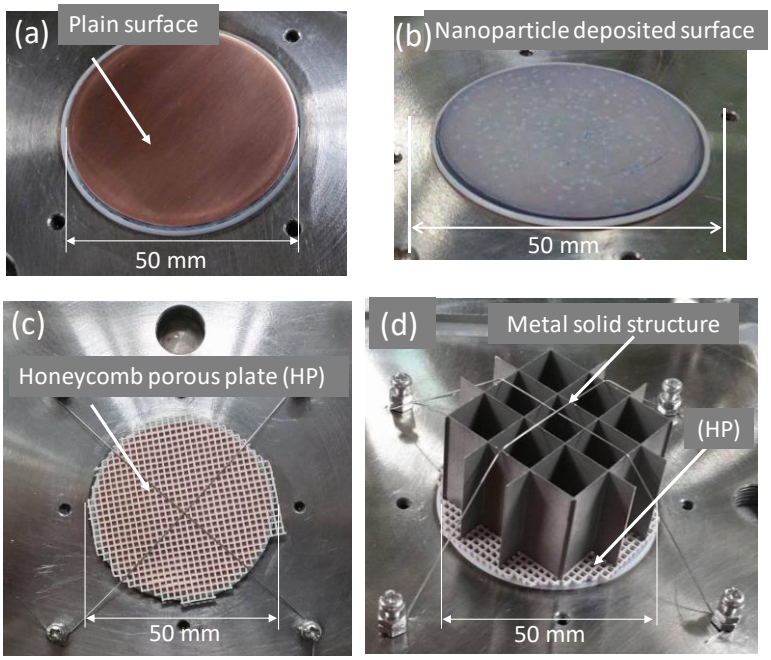

Figure 3-5 Images of surface modifications in the present study (a) plain surface (PS), (b) nanoparticle deposited surface (NDS), (c) honeycomb porous plate attachment (HPP) and (d) square-shaped metal structure on honeycomb porous plate (HPP+SMS).

3.4 Results and discussion

3.4.1 CHF enhancement by honeycomb porous plate in saturated pool boiling of nanofluid

A honeycomb porous plate and water-based nanofluid may be combined to obtain the further CHF enhancement because the CHF of each component has been proven to provide a significant improvement. On the other hand, the cooling capability due to the combination of a honeycomb porous plate and a nanofluid may deteriorate as a result of micropores of the honeycomb porous plate becoming clogged with nanoparticles, resulting

in no water being supplied to the heated surface. Therefore, a durability test for cooling capability by a honeycomb porous plate in pool boiling of a nanofluid was performed.

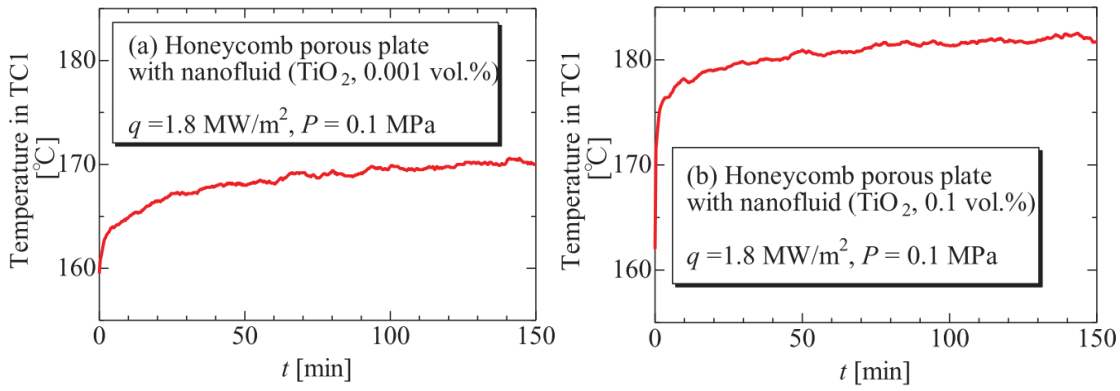

Figure 3-6 Time variation of TC1 just after the addition of nanofluid to pure water (final nanofluid concentration: (a) 0.001 vol.%, (b) 0.1 vol.%).

Figure 3-6 shows the time changes of temperature in TC1 resulting from the addition of nanofluid to pure water in the presence of an attached honeycomb porous plate. The experiment was conducted as follows. First, 900 ml of distilled water was boiled in the presence of an attached honeycomb porous plate. After a steady state condition had been achieved, 100 ml of condensed nanofluid at room temperature was added to boiling pure water so that the final concentration was 0.001 vol.% or 0.1 vol.%. Heat flux is set to approximately 1.8 MW/m^2, which is less than the CHF for the case of an attached honeycomb porous plate in pure water. Interestingly, the CHF did not occur under either experimental condition for more than 2 hours. The temperature in TC1 increased suddenly just after the addition of nanofluid because nanoparticles were deposited on the heated surface. The thickness of nanoparticle deposition related to thermal resistance depends on the nanofluid concentration, which is why the temperature increment in thicker nanofluid

(0.1 vol.%) is higher than that in thinner nanofluid (0.001 vol.%). The temperature in TC1 then saturates at approximately 100 min in both cases. The amounts of nanoparticles deposited on and detached from the heated surface are considered to be approximately the same. Subsequently, CHF experiments were performed because CHF conditions were not reached in these circumstances. Nanoparticle deposition during boiling process occurred at different rate depends on the heat flux. When the steady state condition is achieved, the deposition can be assuming to be optimized and stabilized. At high heat flux near to the occurrence of CHF, steady state condition is achieved with a temperature fluctuation bigger than condition at low heat flux.

Figure 3-7 shows the relationship between the CHF and concentration of nanofluid. As shown in this figure, for the both cases of a nanofluid with a plain surface, the CHF increases up to 1.7 MW/m^2 (pure water: 1.0 MW/m^2), and the CHF is not affected by the nanofluid concentration. On the other hand, the CHF is increased up to more than 2 MW/m^2 by attaching a honeycomb porous plate to the heated surface in pure water as reported in a previous study by Mori & Okuyama (2009).

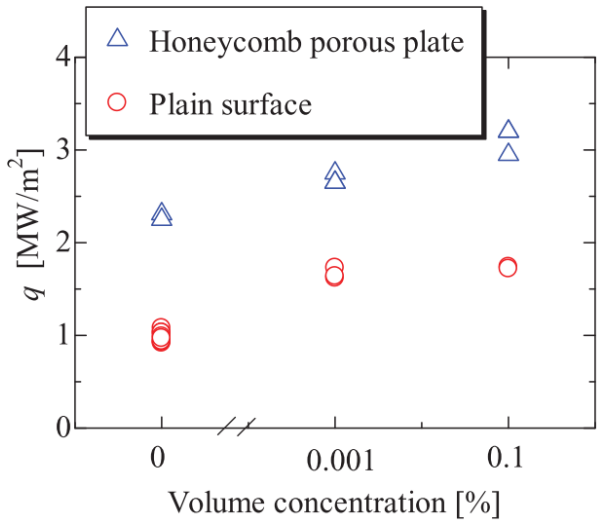

Figure 3-7 Relationship between q_{CHF} and the concentration of the nanofluid.

The CHF with a honeycomb porous plate increases as the nanofluid concentration increases, and, surprisingly, the CHF reaches approximately 3.2 MW/m^2 at maximum for 0.1 vol.% nanofluid. The CHF was increased significantly, by nearly three times compared to the case of pure water on a plain surface. Various surface modifications of the heated surface by porous coating have been proven to increase the CHF in saturated pool boiling. As pointed out in the introduction, the CHF is affected by the heater size. For IVR applications, the cooling method should apply to a large heated surface.

Figure 3-8 shows the boiling curves for different experimental conditions: pure water (○), nanofluid (0.001 vol.%) (△), nanofluid (0.1 vol.%) (□), a honeycomb porous plate with pure water (●), a honeycomb porous plate with nanofluid (0.001 vol.%) (▲), and a honeycomb porous plate with nanofluid (0.1 vol.%) (■). The arrows in the figure correspond to the CHF conditions. The superheats in the case with an attached honeycomb

porous plate are the highest for the case of (■), followed by the cases of (▲) and (●), in this order. For a honeycomb porous plate in pure water, the superheats are roughly the same from low heat flux to CHF. Among the experimental conditions, for the case of honeycomb porous plate with nanofluid (0.1 vol.%), the superheat is the highest (60 K) at the CHF condition. However, this is irrelevant in the case of IVR because a wall temperature of 160°C is sufficiently low compared with the operating temperature. Note that each experimental point could achieve a steady state during the 10-hour boiling experiment for the case of a honeycomb porous plate with nanofluid (0.1 vol.%). This fact is consistent with the results of the durability test shown in Figure 3-6.

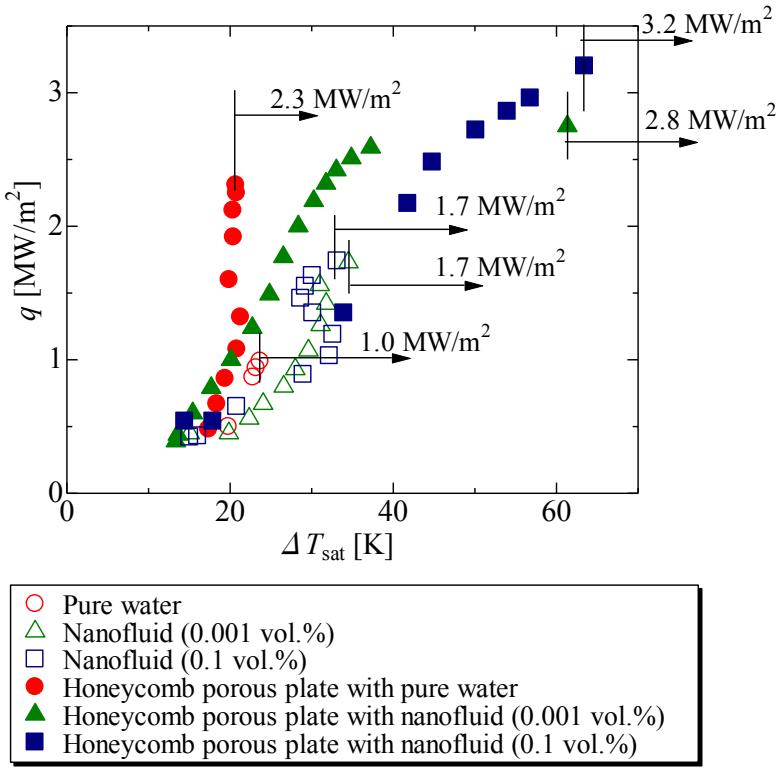

Figure 3-8 Effects of a honeycomb porous plate and a nanofluid on boiling curves.

There was an unusual ascending pattern in Figure 3-8 for nanofluid boiling (△) and (□) from a typical boiling curve as illustrated in Figure 1-1. In the beginning, the heat flux is increased with increasing of superheat temperature. At this region, it is believed that the nanoparticle is deposited onto the heated surface, reached a certain thickness and considered to be steady. However, with an increment of heat flux in the middle, there is a turning point where superheat temperature decreases with the increase of heat flux. At this turning back point, it is believed that some of the nanoparticle deposited on heated surface detach from the surface caused more activation nucleation site available. As a result, wall superheat is decreased. Cie (2002) called the behavior as an inverted boiling crisis. Zuhairi et. al (2013) also observed these strange trends in their boiling curves.

It is argued that if the rheological behavior of nanofluid changed in comparison to the suspending liquid media alone, the transport properties such as thermal conductivity and viscosity change too. This changes will affect the heat transfer performance in a pool boiling. The rheological behavior of nanofluid could be determined by measuring shear viscosity (μ). The shear viscosity (μ) is defined as the ratio of shear stress (τ) to shear rate ($\dot{\gamma}$). This is called Newton's law of viscosity and shown in the below equation.

$$\tau = \mu \frac{du}{dy} = \mu\dot{\gamma}. \tag{3-1}$$

If the shear viscosity (μ) remaining constant while the ratio between shear stress and shear rate is in linear relation, the liquid behavior is called Newtonian behavior. On the other hand, when the shear viscosity (μ) is not constant the nanofluid behavior is called non-Newtonian. In the present study, the viscosity measurement of water-based nanofluid was

not performed. However, there were some literature reports the rheological behavior of titania nanoparticle dispersed in a water base. The study was carried out by Turgut et al. (2009) and Penkavova et al. (2011).

Turgut et al. (2009) investigated the thermal conductivity and viscosity of titania (TiO_2) water-based nanofluid with concentration varies from 0.2 vol.% to 3 vol.%. The mean diameter of the nanoparticle was 21 nm which is the same as used in the present study.

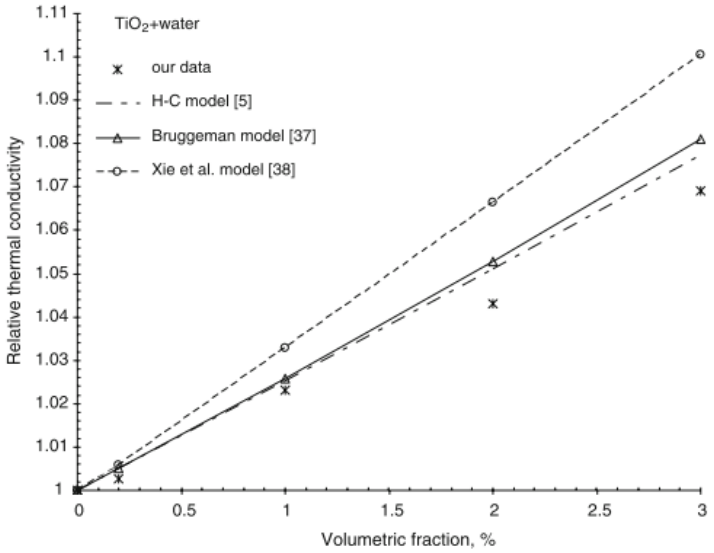

Figure 3-9 The relative thermal conductivity of TiO_2 water-based nanofluid with other models as a function of volumetric fraction (Turgut et al., 2009).

Figure 3-9 shows the relative thermal conductivity obtained in their study in comparison to the other model as a function of water-based nanofluid concentration (vol.%). From the figure, low concentration of water-based nanofluid used in the present study, 0.001 vol.% and 0.1 vol.% have a subtle amount increment of thermal conductivity. Hence, it could be ruled out that the CHF enhancement observed in the present study does not exhibit with the thermal property of the nanoparticle.

Figure 3-10 shows the effective viscosities of various concentration water-based nanofluid measured at temperatures between 13°C and 55°C. They found that the viscosity values for 0.2 vol.% follow quite well the viscosity of pure water. However, for a higher concentration of titania nanoparticles, approximately more than two times of the viscosity value were obtained for 3 vol.% at 13°C, and it behaves as a non-Newtonian fluid. It can be implied that for 0.1 vol.% and 0.001 vol.% of water-based nanofluid used in the present study, the viscosities values will lay down between the water and nanofluid with 0.2 vol.% concentration. In the other study by Penkavova et al. (2011), they used titania water-based with various low concentration ranging from 0.07 to 0.7 vol.%. The study found that all samples exhibit the rheological behavior of the Newtonian. These two studies confirmed that the properties of low concentration of TiO_2 water-based nanofluid are similar to water and behave as a Newtonian fluid.

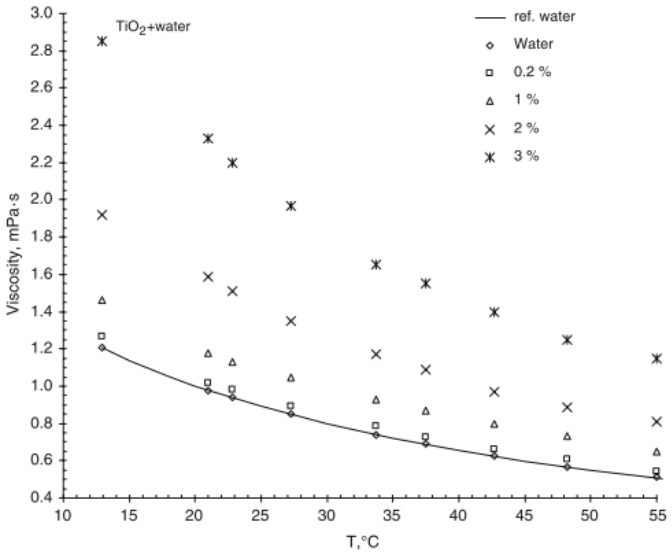

Figure 3-10 Effective viscosities of water-based nanofluid of TiO_2 from 0.2 vol.% to 3 vol.% as a function of temperature (Turgut et al., 2009).

A review made by Sharma et al. (2016) concluded that most nanofluid with a low and high concentration of nanoparticle would exhibit Newtonian and non-Newtonian behavior respectively. Nanofluid can be either Newtonian or non-Newtonian behavior depending not only on nanoparticle concentration but also various factors such as nanoparticle shapes, sizes, surfactants and magnetic fields. In other review literature by Wang et al. (2013) suggested that the Brownian motion and nanoparticle aggregation are the main reason to determine the rheological properties of nanofluids.

Detailed scanning electron microscope (SEM) observations were carried out to clarify the behavior at the clearance between the honeycomb porous plate and the heated surface. Figure 3-11 shows SEM images below the surface of the honeycomb porous plate attached to the heated surface (a) before and (b) after the CHF experiments for 0.1 vol.% nanofluid. As shown in the figures, nanoparticles were deposited beneath the honeycomb porous plate after the experiment. Moreover, microchannels of several tens of microns in width were formed just below the honeycomb porous plate. These microchannels will be confirmed directly by the boiling experiments through the transparent ITO thin heater as a subject of future research.

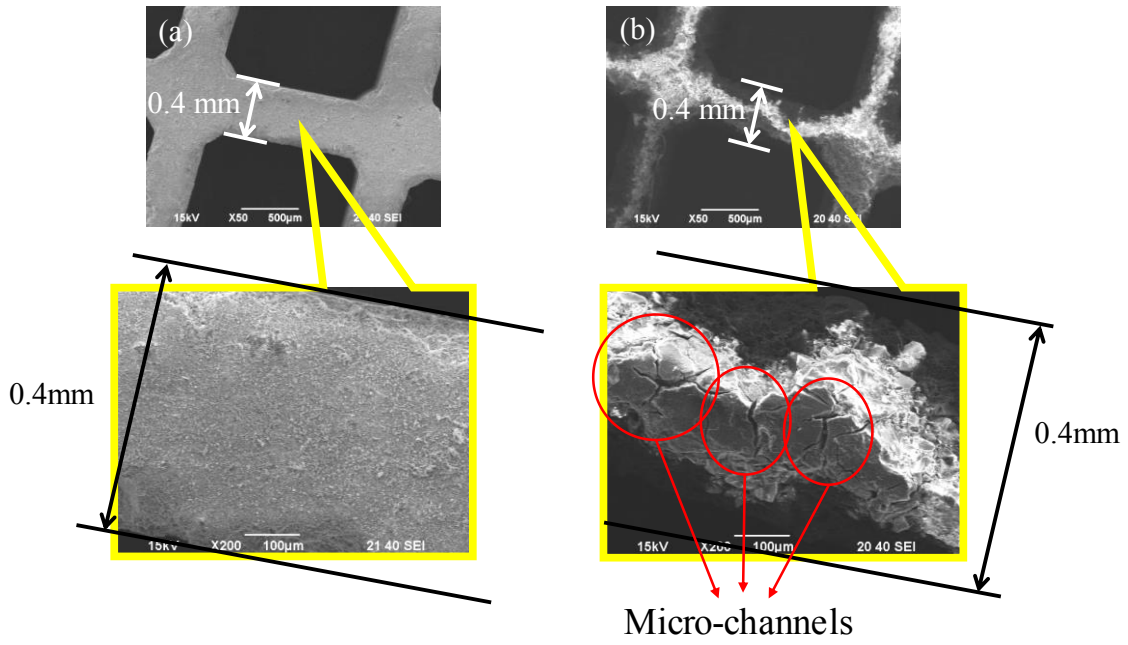

Figure 3-11 SEM images of the bottom surface of a honeycomb porous plate (a) before the boiling experiment and (b) after the boiling experiment (nanofluid: 0.1 vol.%).

Microchannels formed near the heated surface may decrease the flow resistance in the porous layer due to nanoparticle deposition, resulting in increased CHF enhancement. Based on the above discussion, the CHF enhancement mechanism caused by the combination of a honeycomb porous plate and a nanofluid is considered as follows.

Figure 3-12 shows a schematic diagram of the steam and water flows for the combination of a honeycomb porous plate and a nanofluid. During the vigorous pool boiling, a white layer is formed on the heated surface. The surface wettability and capillary wicking performance are improved due to the nanoparticle deposited surface. Therefore, dryout is retarded due to nanoparticle deposition once a liquid is supplied by gravity to the heated surface through vapor escape channels from the top surface. In addition to this effect, the liquid is supplied to the heated surface due to capillary action by the honeycomb porous

plate, as shown in previous studies by Mori and Okuyama (2009), resulting in significant CHF enhancement. As a consequence of the attachment of a honeycomb porous plate to a heated surface in a nanofluid, CHF enhancement in saturated pool boiling occurs due to the effects of wettability, capillary wicking, the inflow of liquid through vapor escape channels, and vapor escaping macro and microchannels.

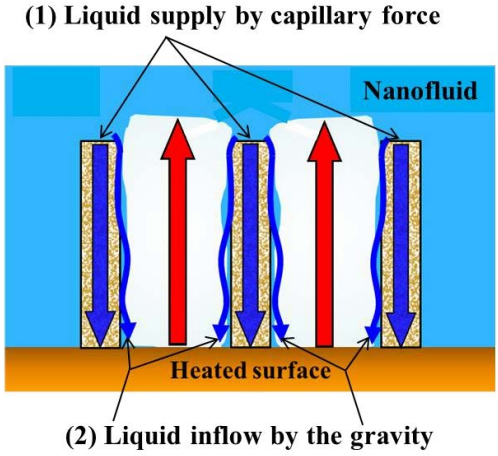

Figure 3-12 Schematic diagram of steam and water flow in a honeycomb porous plate attached to a heated surface.

There are two mechanisms for the water transported to the heater surface in Figure 3-12, (1) through capillary action by the porous plate and (2) vapor escape channels from the bulk liquid due to gravity. If the liquid from both mechanisms reached heated surface and completely evaporated, the volumetric flow rate of water, $\dot{V}_l$ can be converted into heat flux, q_{CHF} expression as below:

$$q_{\mathrm{CHF}} = \dot{V}_l \frac{\rho_l h_{fg}}{A_s} \tag{3-2}$$

where ρ_l is the density of water, h_{fg} is the latent heat vaporization and A_s is the heated surface area. From Eq. (3-2), the volumetric flow rate of water, $\dot{V}_l$ to the heated surface could be estimated at CHF. For example, if the CHF is 4.5 MW/m^2 for the case of honeycomb porous plate attachment on 30 mm diameter heated surface (Mori & Okuyama, 2009), the Q_l is about 1.4714×10^3 m^3/s. This amount is the total for both water supply mechanisms.

In the capillary limit theory by Mori & Okuyama (2009), the CHF occurs when the maximum capillary pressure, $\Delta p_{\mathrm{c,max}}$ is equal to the summation of pressure losses along the liquid vapor path as shown in the following:

$$\Delta p_{\mathrm{c,max}} = \Delta p_l + \Delta p_v + \Delta p_a \tag{3-3}$$

where Δp_l and Δp_v are the pressure drops caused by the liquid flow in the porous part and the vapor flow via channels, respectively, and Δp_a is the acceleration pressure drop due to phase change from liquid to vapor. The maximum capillary pressure can be calculated by

$$\Delta p_{\mathrm{c,max}} = \frac{2\sigma}{r_{\mathrm{eff}}} \tag{3-4}$$

where r_{eff} and σ are effective pore radius ($r_{\mathrm{eff}} = 1.8$ μm) and surface tension, respectively. To know the amount of water to the heated surface via porous part, the calculation can be simplified considering the maximum capillary pressure, $\Delta p_{\mathrm{c,max}}$ is equal to the pressure drops by the liquid flow, Δp_l given by Darcy's law as expressed in the below:

$$\Delta p_l = \frac{\mu_l Q_{\max} \delta_h}{K A_{\mathrm{w}} \rho_l h_{fg}} \tag{3-5}$$

where μ_l is the viscosity of the liquid, $Q_{\max}$ is the maximum heat transfer rate, δ_h is the height of the honeycomb porous plates, K is the permeability ($K = 2.4\times10^{-14}$ m^2), ρ_l is the density of a liquid, A_{w} is the contacted area of the honeycomb porous plate with the heated surface, and h_{fg} is the latent heat of vaporization for water. Therefore, the CHF can be derived from Eq. (3-4) and Eq. (3-5) as

$$q_{\mathrm{CHF}} = \frac{Q_{\max}}{A_s} = \frac{2\sigma K A_w}{r_{\mathrm{eff}}\mu_l\delta_h}\frac{\rho_l h_{fg}}{A_s} \tag{3-6}$$

The first term on the right of Eq. (3-6) is comparable to $\dot{V}_l$ in Eq. (3-2) as shown in Eq. (3-7).

$$\dot{V}_l = \frac{2\sigma K A_w}{r_{\mathrm{eff}}\mu_l\delta_h} \tag{3-7}$$

Therefore Eq. (3-7) could estimate the value for a volumetric flow rate of water through the porous plate at CHF. From the calculation, the volumetric flow rate of water by Darcy's law gives value of 1.4660×10^3 m^3/s. This value shows that at CHF condition, the liquid supply to the heated surface is almost dominant, 99% through the porous plate rather through the vapor escape channels from the bulk. This result seems to be plausible because, at high heat flux, the vapor is escaped from channels and makes difficult for water to get through to the heated surface via cells.

3.4.2 Further CHF enhancement using square-shaped metal structure

3.4.2.1 Effect of square-shaped metal structure (SMS)

SMSs of various as mentioned in the previous section were used to investigate its effect on CHF performance. Figure 3-13 shows the experimental result of CHF for different height of SMS using same cells width (11.3 mm).

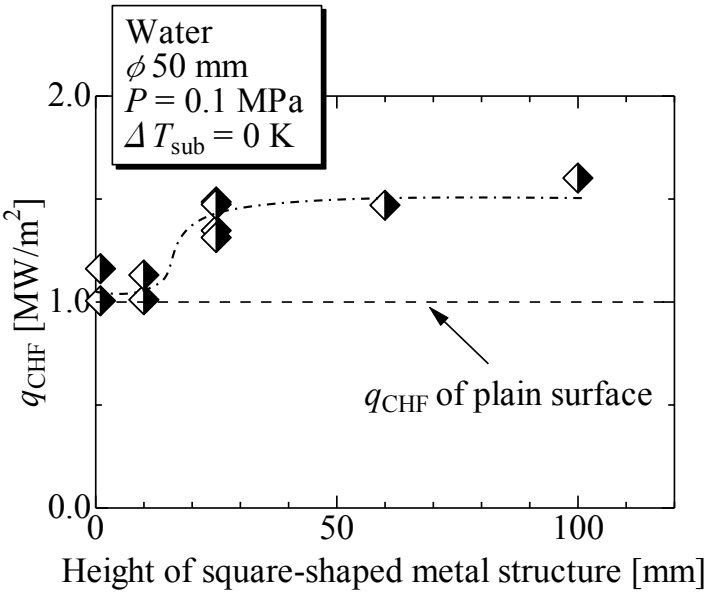

Figure 3-13 Comparison of CHF for different heights of the square-shaped metal structure.

Figure 3-13 show that there is no significant CHF enhancement for SMS with 1 mm and 10 mm heights. However, CHF is enhanced to approximately 1.5 MW/m^2 from 1.0 MW/m^2 (plain surface) for SMS with height 25 mm and above. Figure 3-14 shows the boiling curves and heat transfer coefficient graphs. Regarding the heights of SMS, there are no obvious differences in terms of heat transfer coefficient.

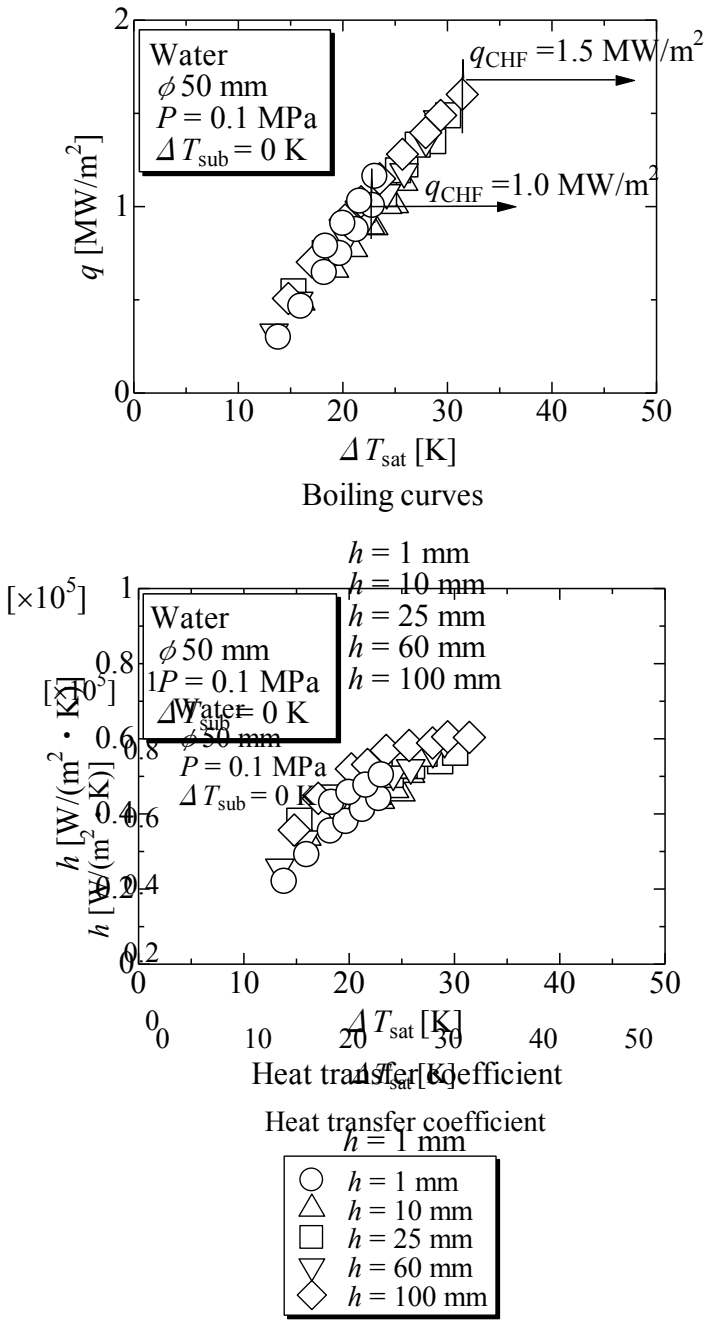

Figure 3-14 Boiling curves and heat transfer coefficient graph for different heights of the square-shaped metal structure.

Critical heat flux experiments were performed in order to investigate the effect of the cell width of the SMS. Square-shaped metal structures of the same height and having

cells of various widths (5.6 mm, 7.8 mm, 11.3 mm, 15.9 mm, 22.5 mm, and 25 mm) were installed on the heater surface. The experimental results are shown in Figure 3-15. The figure shows the CHF values normalized to the CHF obtained by Zuber's model versus the cell width given in terms of wavelength; L' obtained using Eq. (1-8). The curve for one vapor jet, $N_j = 1$, obtained using Eq. (1-11), the theoretical validity of which was confirmed by Lienhard et al., is also shown in Figure 3-15. The figure indicates that CHF is optimized by a cell width of 11.3 mm ($L/\lambda_D = 0.40$). For small cell widths ($<$ 11.3 mm), the tendency of the CHF could not be predicted by Eq. (1-11) because the inviscid model of water no longer applies. This result is consistent with Lienhard et al., (1973) because a cell width of 11.3 mm is approximately half the most dangerous wavelength, λ_d, for water at atmospheric pressure (27 mm) and exhibits the highest CHF among the various cell widths.

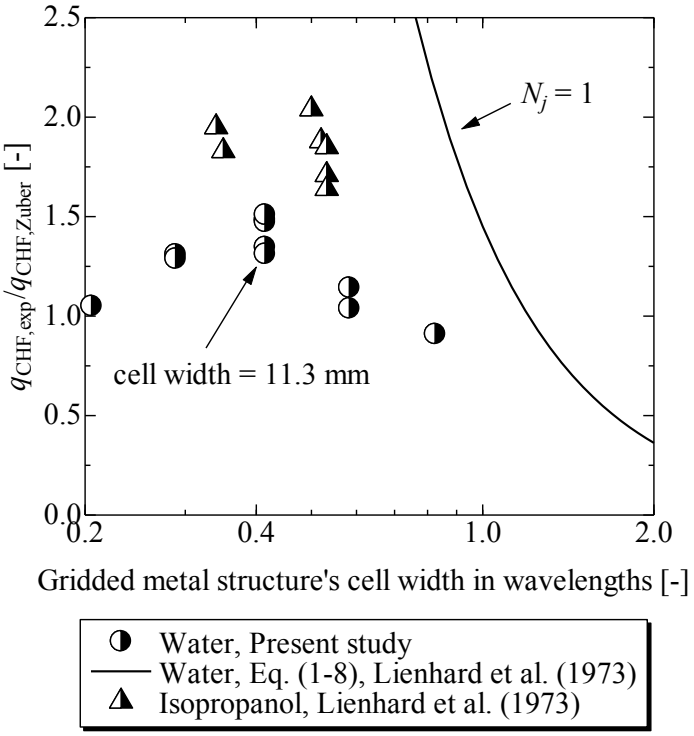

Figure 3-15 CHF enhancement for square-shaped metal structure with various cell width in wavelengths and the curve for $N_j = 1$ in Eq. (1-8).

From the experimental results (Figure 3-13 and Figure 3-15), a significant enhancement of CHF obtained using 25 mm (1.5 MW/m^2) compared to 1 mm and 10 mm in height (1.0 MW/m^2) with the same cells width, 11.3 mm. While the CHF enhancement with 25 mm in height is similar to 60 mm and 100 mm in height. From the boiling configuration, the coalesced bubble formation in the case of SMS with 25 mm, 60 mm and 100 mm were similar. Bubbles left the cell individually with different period and coalesced and detached from the top of the SMS. The SMS with 25 mm in height could represent 60 mm and 100 mm in height SMS. The reason as mentioned above explains, why the SMS with 25 mm in height and 11.3 mm in cell width was chosen to further investigate the combination effect

of surface modification by honeycomb porous plate and nanofluid on CHF. From a technical point of view, with the height of 50 mm, the heated surface and the coalesced bubble on top of the SMS can be captured in one frame by the high-speed camera. This could not be done using SMS height higher than 50 mm due to our high-speed camera limitation.

Figure 3-16 shows the growth process of a coalesced bubble on top of the plain heated surface under the steady state condition at 1.05 MW/m^2. At 0 ms, the previously coalesced bubble detached from the heated surface, and new vapor bubbles simultaneously formed on the heated surface. A large number of vapor bubbles formed rapidly, and a new coalesced bubble can be observed in the image at 20 ms. The coalesced bubble grows and quickly detaches from the heated surface at 120 ms.

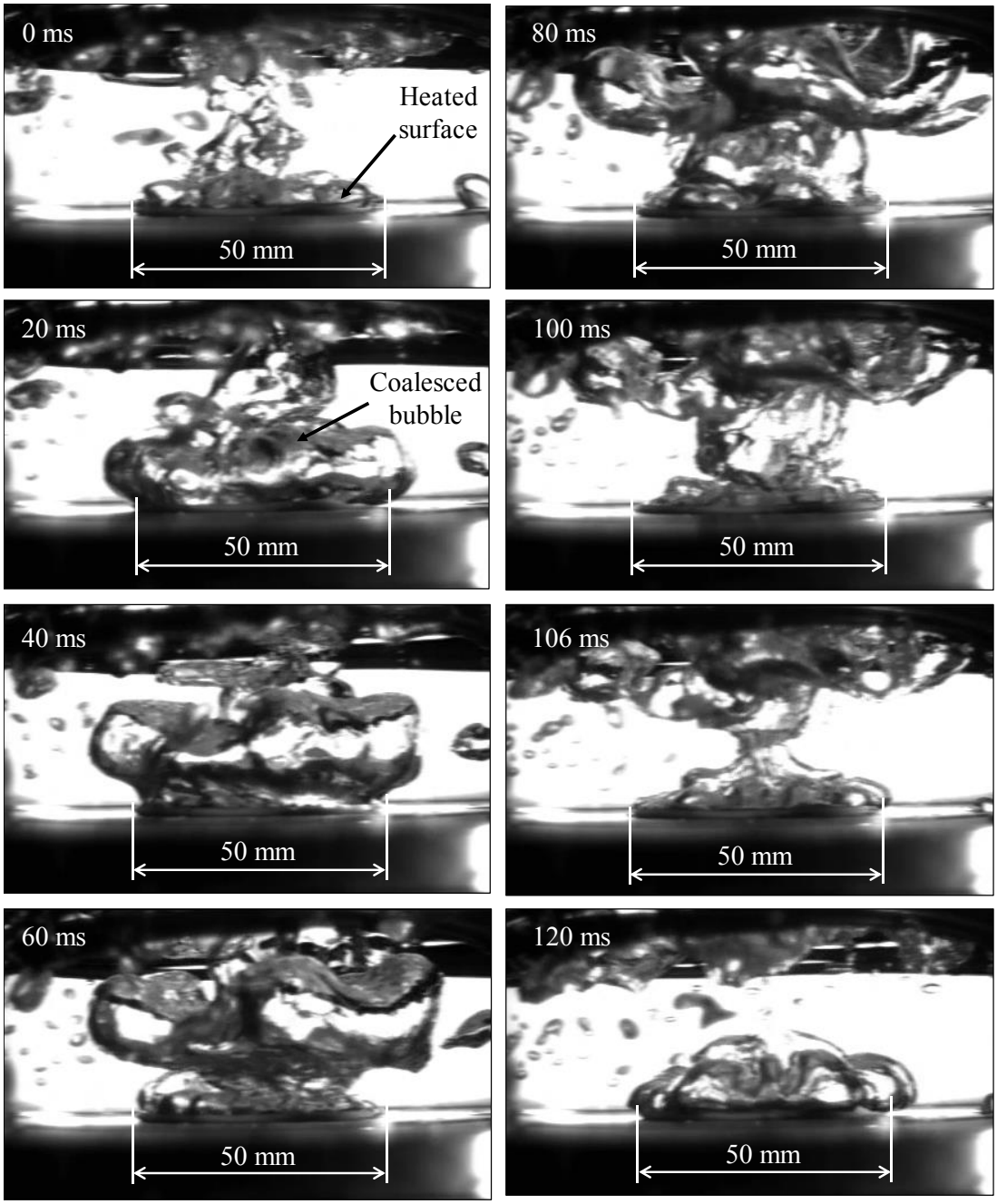

Figure 3-16 Change of boiling configuration of the plain surface (△) at 1.05 MW/m^2.

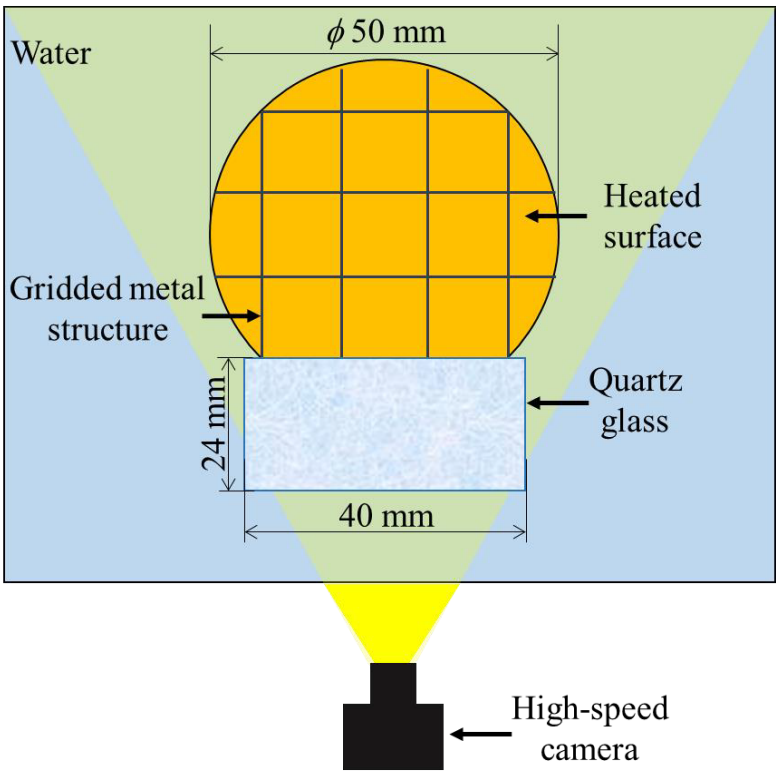

Figure 3-17 Top views of the heated surface for the visualization of the boiling behavior with a square-shaped metal structure (SMS).

Figure 3-17 shows a top view of the heated surface for the visualization of the boiling behavior with the square-shaped metal structure in distilled water. The SMS with a cell width of 11.3 mm and a height of 25 mm was chosen for this purpose because of the CHF enhancement provided by this structure. One part of the square-shaped metal structure's wall was removed and replaced by a block of quartz glass (L40 mm × W24 mm × H34 mm), so that the vapor and liquid could be contained within the same space as the other cells of the structure while the boiling behavior could be observed through the transparent glass. Stainless steel wire of ϕ 0.5 mm was used to fix the square-shaped metal structure and the quartz glass to the heated surface. Video recording was performed using a high-speed

camera at 500 fps under a steady state condition at 1.05 MW/m^2 for comparison with the images of Figure 3-16.

Figure 3-18 shows the boiling configuration for HPP+SMS with distilled water. As shown in Figure 3-18, one vapor jet clearly appears in each SMS cell, for a total of nine vapor jets. Each vapor jet created a liquid path that surrounds the jet within the cell, allowing liquid to reach the heated surface. As a result, the amount of water is increased significantly because nine vapor jets exist at the top of the heated surface. This improvement led to a higher CHF for the SMS (1.5 MW/m^2) compared to PS (1.05 MW/m^2). This experimental result is aligned with the proposal by Lienhard et al., (1973) which suggested that an increasing number of vapor jets could lead to CHF enhancement. However, it should be noted that Lienhard et al. did not discuss the behavior of coalesced bubble on top of the metal structure. According to the high-speed camera observation, as shown in Figure 3-16 and Figure 3-18, the size of coalesced bubbles above SMS was smaller than that of PS. Additionally, the hovering periods (94$\pm$9 ms) of the coalesced bubbles above the SMS is shorter than that (120$\pm$19 ms) of the PS. The hovering period shortened due to SMS indicates more liquid can be supplied to the heated surface because of the increase in bubble detachment frequency, resulting in CHF enhancement.

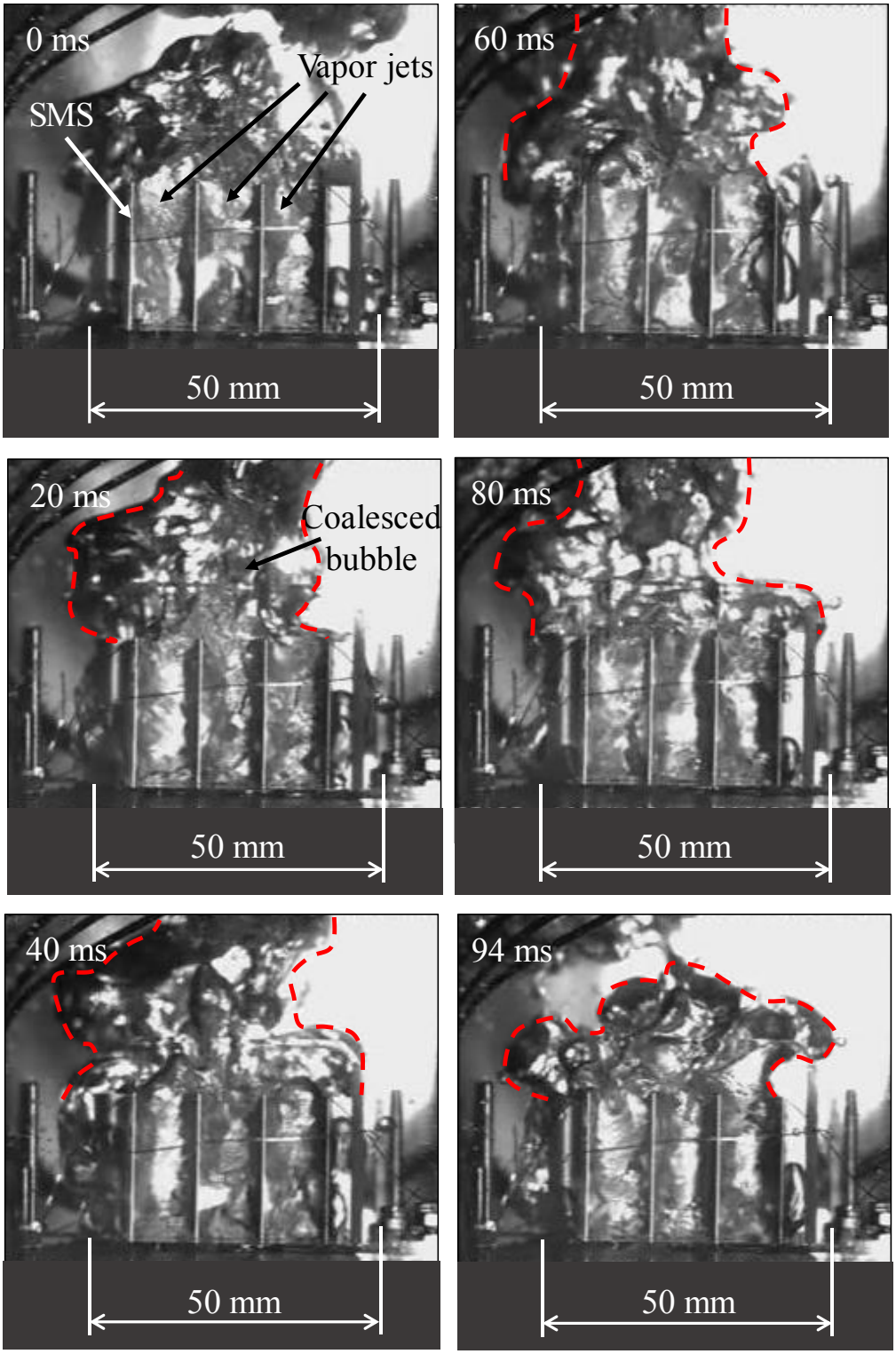

Figure 3-18 Change in the boiling configuration for the square-shaped metal structure in distilled water at 1.05 MW/m^2.

3.4.2.2 Combination effects of a honeycomb porous plate, a square-shaped metal structure, and nanofluid on CHF enhancement

Figure 3-19 shows the boiling curves for the plain surface, the honeycomb porous plate, and the square-shaped metal structure in combination with the honeycomb porous plate for distilled water and high-concentration nanofluid (0.1 vol.%) as working fluids. The values over the arrows in Figure 3-19 are the CHF values excluding the case of nanofluid boiling with HPP+SMS because the steady state condition was not achieved due to insufficient coolability in the condenser (denoted by * in Figure 3-19 and Figure 3-21).

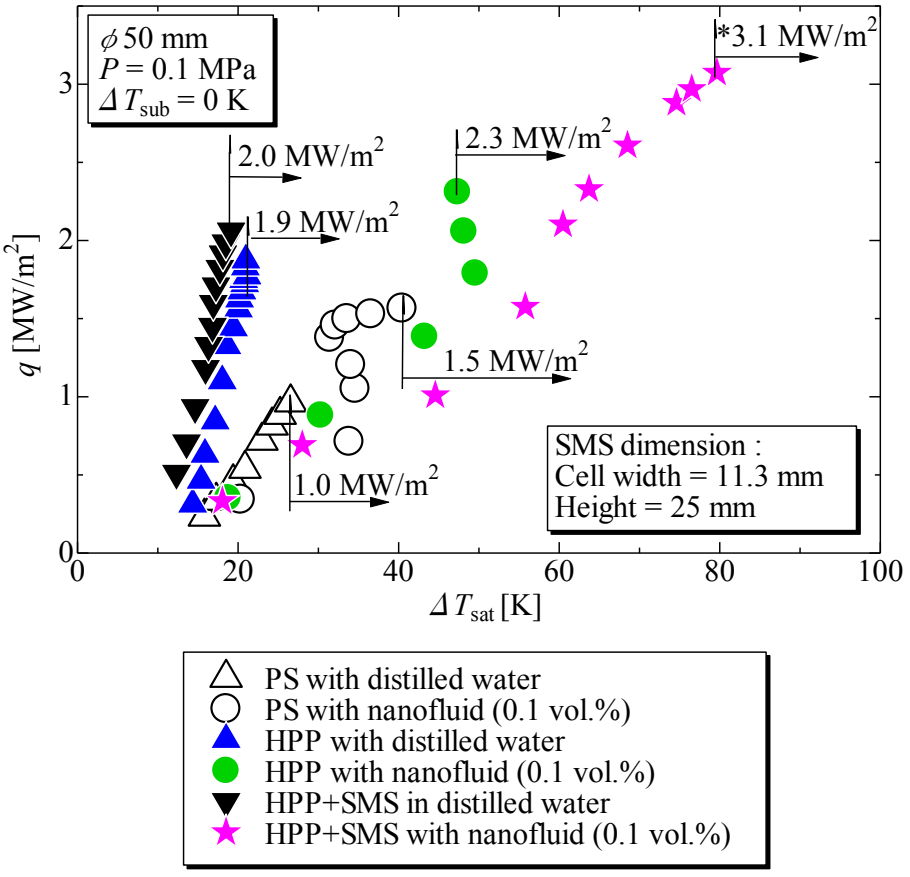

Figure 3-19 Boiling curves for various surface modifications and working fluids.

As shown in this figure the CHF is enhanced for all surface modifications, as compared to the PS in water boiling (△). The CHF for PS in nanofluid (○) enhanced up to 1.5 MW/m^2. Surface modification with HPP in distilled water (▲) (1.9 MW/m^2) were greater than that for the PS in water boiling (△) (1.0 MW/m^2). The case of HPP+SMS (▼) shows improvement in both heat transfer coefficient and CHF as compared to PS (△). The attachment of an SMS to the heated surface caused the coalesced bubble to detach faster. Hence liquid supply to the heated surface was sustained, resulting in CHF enhancement. Separately, a more active nucleation site underneath the porous part attached to the heater surface was effectively activated. Therefore, an increase in the heat transfer coefficient can be observed for HPP+SMS. The attachment of the HPP (▲) and HPP+SMS (▼) in distilled water provided similar CHF values and a comparable heat transfer coefficient. These results show that the present of SMS on top of HPP did not have a significant impact compared to SMS attachment on the plain surface which show about 50% CHF enhancement to the plain surface. There is a potential that the liquid is more accessible to the heated surface with SMS. However, the HPP performance outweighs the SMS effect in this condition.

The case of HPP in nanofluid (●) enhanced the CHF to 2.3 MW/m^2 as compared to HPP in distilled water (▲). This is due to the formation of a nanoparticle-deposited layer during the boiling process, which changed the roughness and increased the wettability of the heated surface. Hence, these changes enable rewetting of the dryout region and delays burnout. However, the deposited layer causes thermal resistance and deteriorates the heat transfer coefficient. This becomes clear by observing the boiling curves for HPP in nanofluid (●) and HPP in distilled water (▲) at a heat flux of 1.5 MW/m^2. At the same heat flux, the values for HPP in nanofluid (●) were shifted to the right with a higher superheat wall, as

compared to HPP in distilled water (▲).

The heat flux in the case of HPP+SMS with nanofluid (★) is removed significantly up to 3.1 MW/m^2, even though the same combination (HPP+SMS) in distilled water (▼) showed no significant CHF enhancement as compared to HPP in distilled water (▲). The reason for this is the improvement in liquid supply provided by the presence of the square-shaped metal structure. Then, liquid reaches the heated surface through strong capillary action by the porous plate and spread quickly on the nanoparticle deposited surface. Each time the heat flux is increased, boiling becomes more vigorous, and microlayer evaporation leaves more nanoparticles on the heated surface at higher heat flux (Kwark, Moreno, et al., 2010). The process repeats, resulting in the possibility of thicker nanoparticle deposition. This is a plausible explanation for the high superheat wall observed in Figure 3-19 for HPP+SMS in nanofluid (★). As shown in Fig. 12, the results obtained at 2.0 MW/m^2 indicate that the heat transfer coefficient for HPP+SMS in nanofluid (★) deteriorated more than that for HPP in nanofluid (●).

Figure 3-20 illustrates the schematic diagram of vapor and liquid flow near the heated surface with magnification of honeycomb porous plate on the right for HPP+SMS with nanofluid. As indicated in the figure, the mechanism of the high heat removal up to three times are as follows:

(i) Automatic liquid supply to the heated surface through the porous plate due to capillary force by the honeycomb porous plate.

(ii) Reduction of flow resistance between generated vapor and liquid (moving downward (iii)) in the vapor escape channels.

(iii) The inflow of liquid through the vapor escape channels (iii) directly to the

heated surface.

(iv) Liquid spreads quickly on the nanoparticle-deposited surface due to the improvement of surface wettability and capillary wicking.

(v) The increase in the coalesced bubble's detachment frequency resulted in the ease of liquid supply to the heated surface by the SMS's cells.

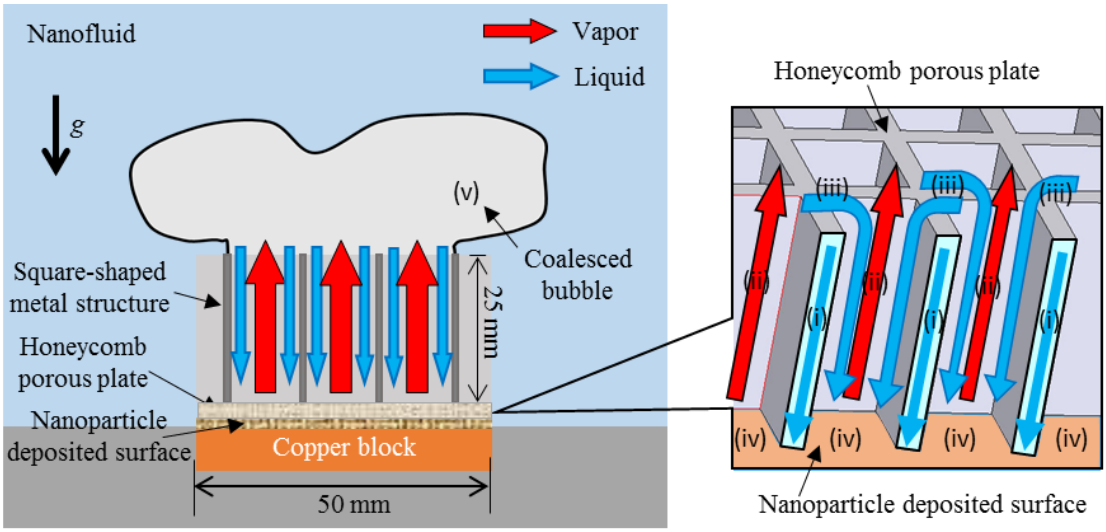

Figure 3-20 Schematic diagram of the liquid supply mechanism for HPP+SMS with nanofluid.

Figure 3-21 illustrates the relationship between CHF enhancement ratio and heater sizes express in dimensionless length given by Eq. (1-8). L' can be considered to represent infinite heater surface if the value is greater than 20. Experimental results from Chapter 2 and previous section are also added in the figure for comparison. Our experiment with 50 mm diameter has dimensionless heater length, L' value of 20. Attachment of honeycomb porous plate in nanofluid boiling (0.1 vol.%) on heater surface of 30 mm in diameter heater surface (L' = 12) has shown CHF enhancement about 3.2 times against PS in water boiling.

Yet, with larger heater surface ϕ 50 mm, HPP in water-based nanofluid could not enhance CHF as much as 3 times. The gap of this result could be explained by liquid supply to the heated surface from above at high heat flux, particularly, from sides of HPP. SMS attachment resulted in increasing the detachment frequency of the coalesced bubble and sustains liquid supply to the heated surface. Combination of metal solid structure and honeycomb porous plate in nanofluid boiling could enhance the CHF significantly, three times of plain surface CHF, even on a large heater surface.

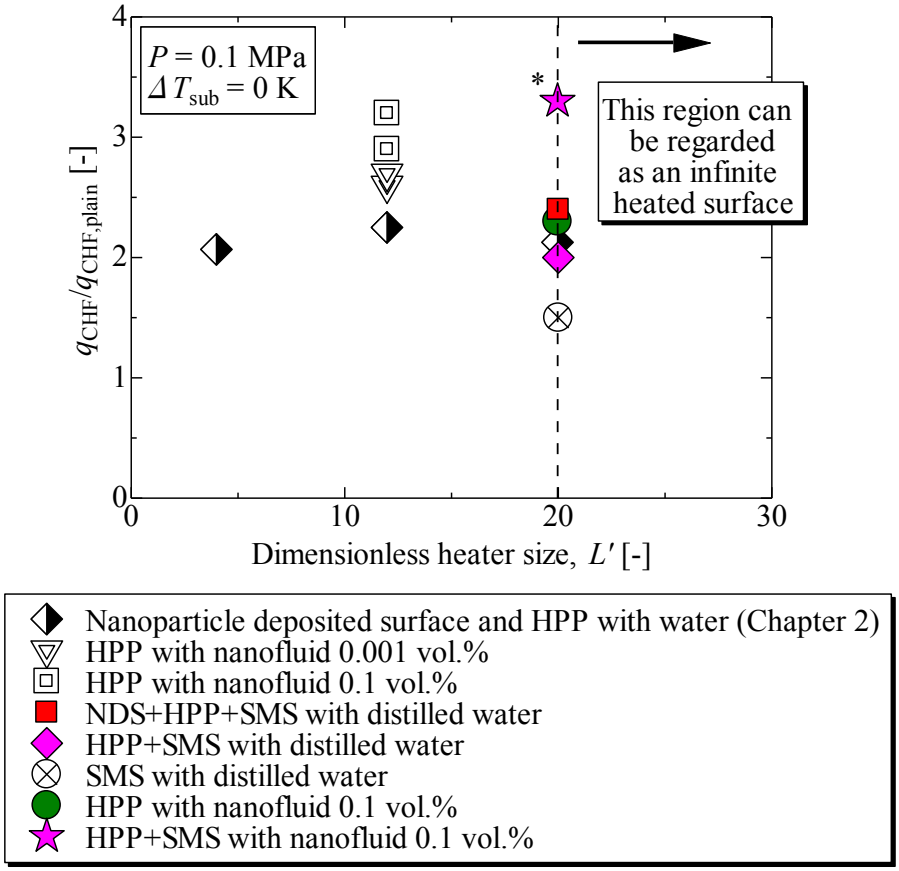

Figure 3-21 CHF enhancement ratio as a function of dimensionless heater size, L'.

3.5 Conclusion

The CHF enhancement in saturated pool boiling of nanofluid by the attachment of a honeycomb-structured porous plate to a ϕ 30 mm heated surface was investigated experimentally. The following conclusions were obtained:

1. A durability test to determine the cooling capability of a honeycomb porous plate in saturated pool boiling of a nanofluid was performed. There was a concern that micropores in the honeycomb porous plate may have become clogged with nanoparticles, resulting in a decrease in the CHF. As a result, for a heat flux of 1.8 MW/m^2, no CHF could be observed for more than two hours under the experimental conditions, such as a heat flux of 1.8 MW/m^2 and a high nanoparticle concentration of 0.1 vol.% (4 g/L).
2. The CHF increased as the nanoparticle concentration increased. The CHF is enhanced significantly up to 3.2 MW/m^2 at maximum for 0.1 vol.% nanofluid. To the best of the author's knowledge, the highest value of CHF (3.2MW/m^2) was obtained for a large heated surface having a diameter of more than 30 mm.
3. The heat transfer coefficient with a honeycomb porous plate decreased in accordance with the increase in the nanoparticle concentration.4. Detailed SEM observation beneath the surface of a honeycomb porous plate in contact with the heated surface revealed microchannels of several tens of microns in width just below the honeycomb porous plate. These microchannels may act as vapor escape channels for CHF enhancement.

Surface modification by honeycomb porous plate, square-shaped metal structure, and nanofluid have been investigated experimentally using water and nanofluid under saturated and atmospheric conditions with a large heater surface (ϕ 50 mm). The following conclusions were obtained:

(1) Attachment of a square-shaped metal structure on a plain surface in water boiling shortens the hovering period of coalesced bubble compared to the plain surface at the same heat flux (1.0 MW/m^2). Therefore, more water supply is sustained during the detachment of the coalesced bubble.

(2) The combination of a square-shaped metal structure and honeycomb porous plate attachment on a plain surface increases CHF to 2.0 MW/m^2. Additionally, heat transfer coefficient is improved due to more active nucleation site density underneath porous part that is attached to the heater surface is activated effectively.

(1) Nanoparticle deposition during the boiling process significantly improves wettability and capillarity on the heated surface. Hence the dry out region is delayed, and further CHF enhancement is observed.

(2) The combination of a honeycomb porous plate and square-shaped metal structure in a high concentration of water-based nanofluid could remove high heat flux up to 3 MW/m^2.

Chapter 4 Effect of the surface orientation on the CHF enhancement at honeycomb porous attachment

4.1 Introduction

In this chapter, pool boiling experiments were performed with an inclination of heater surface unlike studies reported in the previous chapter, with upward-facing horizontal flat heater surface. Pool boiling experiment is conducted to examine the effect of surface modification by honeycomb porous plate and nanoparticle deposited surface on CHF. Experiments on the pool boiling of water at saturated and atmospheric conditions were conducted for heater orientations ranging from upward-facing to fully facing downward.

Priorane (2005) performed an experimental study on nucleate boiling and critical heat flux of the dielectric fluids FC-72 and HFE-7100 with a smooth copper surface. They found that the surface orientation strongly influences the heat transfer coefficient and the CHF. From experimental results, the CHF decreases slightly as the orientation angle increases from 0° to 90°. However, the CHF decreases rapidly as the orientation angle approaches to downward-facing 180°. The CHF correlation obtained is given as following.

$$q_{\mathrm{CHF}} = C_{f,w,sat} f(\theta) \left\{ \rho_v^{1/2} h_{fg} \left[[\sigma(\rho_l - \rho_v) g] \right]^{1/4} \right\}, \tag{4-1}$$

$$f(\theta) = 1 - 0.001117\theta + 7.79401\times10^{-6}\theta^2 - 1.37678\times10^{-7}\theta^3, \quad (4\text{-}2)$$

where the coefficient of $C_{f,w,\,sat}$ depending on heater orientation and $f(\theta)$ represents the effect of the heater orientation for the case of FC-72.

Liao et al. (2008) report the surface orientation effect on CHF using three differences of heat transfer surface, normal surface, hydrophilic surface and a superhydrophilic surface having a contact angle of 55°, 30°, and 0° respectively. They provide a prediction CHF correlation from the experimental results which considering surface orientation and contact angle.

$$q_{\mathrm{CHF}} = q_{\mathrm{CHF,Zuber}}\left[-0.73 + \frac{1.73}{1 + 10^{-0.021\times(185.4-\theta)}}\right] \times\left[1 + \frac{55-\beta}{100}\cdot(0.56 - 0.0013\theta)\right], \quad (4\text{-}3)$$

Sakashita et al. (2009) reported CHF and near-wall boiling behaviors in saturated on vertical (90°) and inclined surfaces. They investigate the trigger mechanism of the CHF using a conductance probe. From the signal by the conductance probe, they found the surface orientation affects the period of vapor masses to pass the heated surface. The duration of vapor mass passage increased as inclination angle approaches to downward-facing and this is the main reason that triggers CHF.

Guo & El-Genk (1992) performed an experiment with a copper disk having a diameter of 50 mm in a pool boiling of saturated water. The heater surface orientations are from vertical to fully face downward-facing. Coalesced bubble are trapped below the heated surface in the case of fully downward facing and CHF drop drastically. For an inclined

heated surface, the bubble is removed by buoyancy and creates a movement to leave the heated surface. The CHF correlation by Guo & El-Genk (1992) is shown as follow.

$$q_{\mathrm{CHF}} = [0.034 + 0.0037(180 - \theta)^{0.656}]h_{fg}\sqrt[4]{\rho_v^2 g\sigma(\rho_l - \rho_v)}. \quad (4\text{-}4)$$

Finally, the empirical correlation by Chang and You (1996) using FC-72 as a working fluid is given by

$$\frac{q_{\mathrm{CHF}}}{q_{\mathrm{CHF},0^\circ}} = 1.0 - 0.00120 \cdot \theta \cdot \tan\,(0.414 \cdot \theta) - 0.122 \cdot \sin\,(0.318 \cdot \theta). \quad (4\text{-}5)$$

CHF values with above-mentioned literature are summarizing in Figure 4-1.

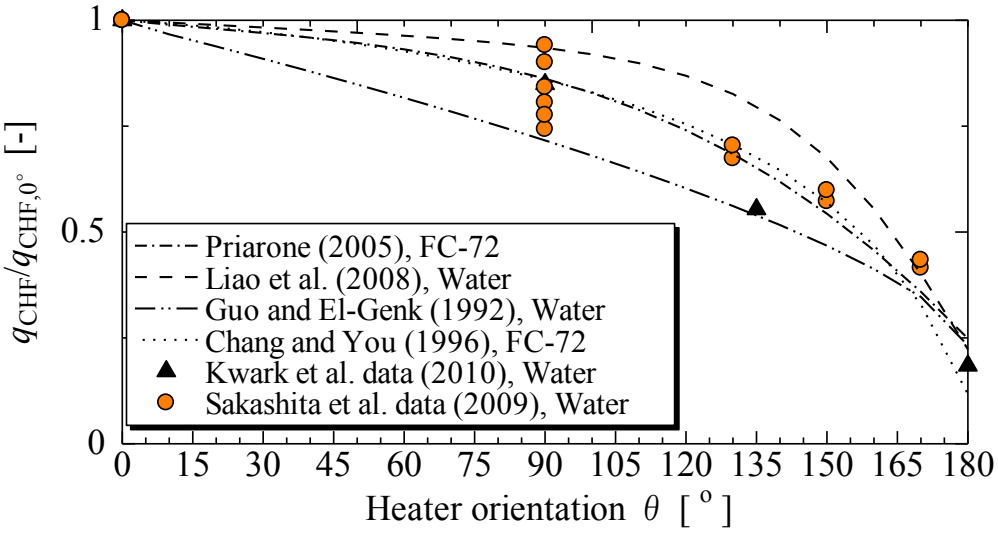

Figure 4-1 CHF values normalized to upward-facing (0°) from literature.

As shown in Figure 4-1, the measured CHF decreases as the angle of inclination of the surface heater increases. In general, the main reason for this decline is due to the difficulty for the coalesced bubbles to detach from the heater surface. Bubbles generated on the incline heated surface tends to be stagnant and cover the surface, especially in the case

of fully downward-facing. Hence, the CHF decreases substantially as the orientation approaches downward-facing.

This chapter reports the effect of heater surface orientation on CHF enhancement at honeycomb porous plate attachment. Heater orientations considered in this chapter are upward-facing 0°, vertical 90°, downward-facing 135°, 150°, 170° and fully facing downward 180°. The experiment has been conducted using a plain surface or nanoparticle deposited surface with honeycomb porous plate attachment for each heater surface orientation from upward-facing (0°) to downward-facing (180°). The boiling behavior of a coalesced bubble near the heated surface is recorded using a high-speed video camera during steady state condition to examine the hovering period. A wettability test is conducted on a nanoparticle deposited surface to study the spreading behavior of a droplet. The results from the boiling configuration and rewetting investigation are used to explain the CHF enhancement.

4.2 Objectives

The objectives of the experiments conducted in this chapter are listed as following:

1. To study the relationship between heater orientation from horizontal upward-facing (0°), vertical (90°) to downward-facing (135°, 150°, 170° and 180°) under saturated and atmospheric conditions. Heater surface modifications are plain surface, honeycomb porous plate attachment, nanoparticle deposited surface, and a combination of honeycomb porous plate and nanoparticle deposited surface.

2. To observe the hovering period of coalesced bubble behavior at low and high heat flux before CHF for upward-facing and inclination of 170° heater surface.
3. To investigate the heater surface wetting performance with a droplet spreading on a modified surface by nanoparticle deposited surface.

4.3 Experimental apparatus and procedures

4.3.1 Experimental apparatus

A schematic of the experimental apparatus is shown in Figure 4-2(a). The pool-boiling vessel is made of borosilicate glass and has an inner diameter of 87 mm and a height of 500 mm. An auxiliary heater is fixed in the vessel to boil the bulk liquid and keep it at the saturation temperature. An external condenser is installed on top of the vessel to condense the vapor to a liquid. One thermocouple (T.C.2) is placed in the vessel near the heated surface to ensure the bulk liquid is at the saturation temperature.

Figure 4-2(b) shows the test heater used in the present study. A square ceramic heater is embedded in a cavity of polycarbonate substrate using silicon sealant (KE-3418). The 12 mm × 12 mm surface of a ceramic heater (ULTRAMIC® WALN-6, from Watlow®, 12 mm × 12 mm × 2.5 mm, 11.52Ω) is used as the boiling heat transfer surface. Experiments are performed on heated surfaces with orientations of 0°, representing an upward-facing surface; 90°, representing a vertical surface; and 135°, 170°, and 180°, representing downward-facing surfaces. The heat loss from the sides and bottom of the ceramic heater is negligible because of the low thermal conductivity of the silicon sealant. Power is supplied to the ceramic heater by an alternating current (AC) voltage regulator. A thermocouple (T.C.1)

with an outer diameter of 0.1 mm is installed underneath the ceramic heater and connected to an overheating prevention device. A diagram of the electric heating circuit used in the present study is shown in Figure 4-2(c). Lastly, the boiling surface temperature is calculated from T.C.1 using the heat equation.

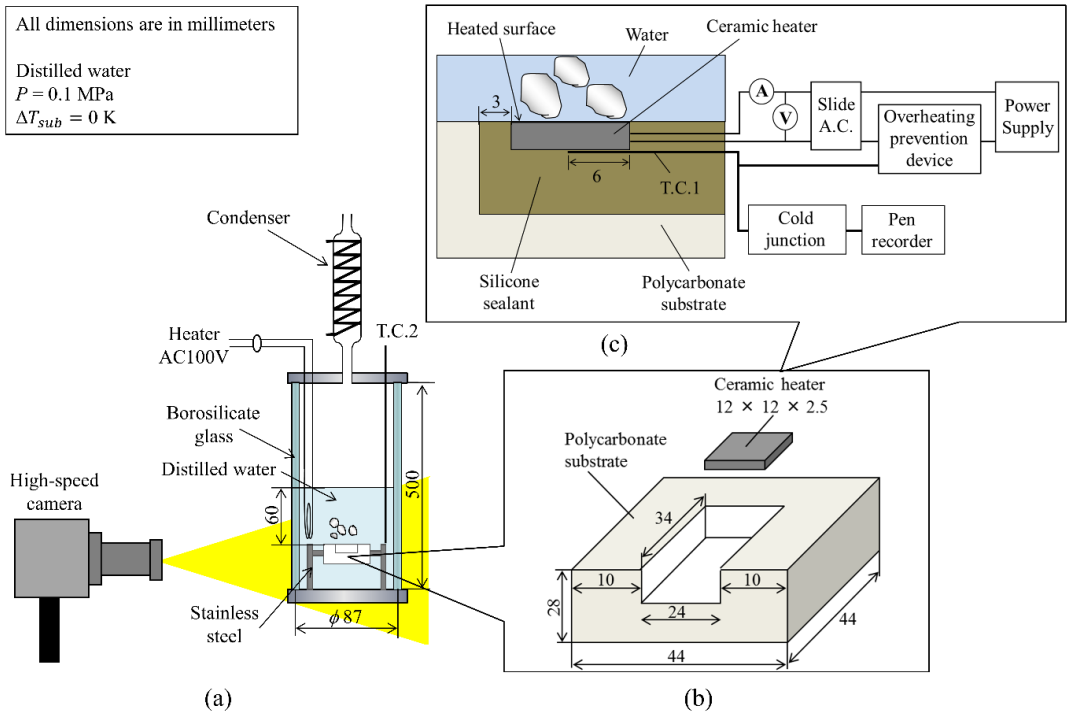

Figure 4-2 Schematics of (a) experimental apparatus, (b) test heater assembly and (c) electrical circuit.

4.3.2 Preparation of nanoparticle deposition on heated surface

TiO_2 nanoparticles (Nippon Aerosil Co., Ltd. AEROXIDE TiO_2 P 25) were selected as test nanoparticles and were dispersed in distilled water. The mean particle diameter reported in the product specifications was 21 nm. The heated surface of the ceramic heater was polished using waterproof 2000-grit sandpaper. For preparation, 400 ml of distilled

water was boiled for 30 min using a heater installed in the test vessel to remove any dissolved gas. Then, the ceramic heater was heated with a constant heat flux of 0.5 MW/m^2 until a steady state was reached. Next, 100 ml of nanofluid (C = 0.50 at %), which had been stirred earlier for one hour using an ultrasonic bath, was added to the boiling distilled water in the test vessel. Therefore, the final nanofluid concentration was 0.1 wt% (0.026 vol%). To form the nanoparticle deposited surface (NDS), 10 min after the addition of the nanofluid to the test vessel (Okawa et al., 2012), the heating was turned off, and the nanofluid was removed from the test vessel to prevent further nanoparticle deposition on the heated surface. The vessel was then cleaned and refilled with distilled water. During this process, a white layer formed on top of the ceramic heater as a result of the nanoparticles deposited during vigorous boiling (Figure 4-4(c)).

4.3.3 Honeycomb porous plate

Honeycomb porous plate is cut into a square of 12 mm × 12 mm in dimension to be fixed onto the heated surface.

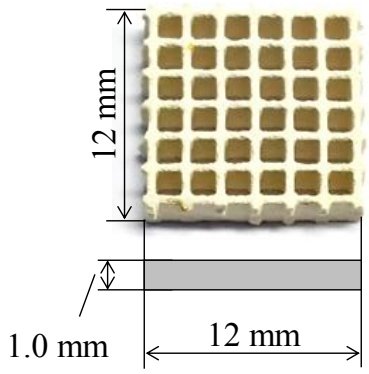

Figure 4-3 Dimensions of honeycomb porous plate for heater orientation experiment.

4.3.4 Experimental procedure

Experiments were conducted using distilled water as the working fluid under saturated and atmospheric conditions. The pool boiling container was filled with distilled water to a height of approximately 60 mm above the heated surface. The working fluid was rigorously boiled for 30 min to remove dissolved air. A sheathed heater was used to maintain saturated boiling conditions. At each step, the heat flux was increased gradually by approximately 0.1 MW/m^2 until the heating surface showed a rapid rise in temperature. All measurements were taken in a quasi-steady state. The system was considered to be in a quasi-steady state when the temperature fluctuation did not exceed 0.25 K for at least 5 min. The heating was automatically stopped by the overheating prevention device when the reading of T.C.1 rapidly increased above 200 °C to prevent damage to the heater and the thermocouples beneath the ceramic heater. The heat flux was determined from data measured by a voltmeter, an ammeter and the area of the heated surface (12 mm × 12 mm). The last measured data point before the boiling transition was defined as the CHF. As the heat flux increased under steady state conditions, the boiling behavior on the top of the heater surface was recorded several times by a high-speed camera at 4000 fps for intervals of 5 s for each steady state condition. The four surfaces considered in this study are an unmodified plain surface (PS), HPP attachment (HPP), an NDS, and an NDS with an HPP attachment (NDS+HPP). Images of these four surfaces are shown in Figure 4-4(a)–(d), respectively.

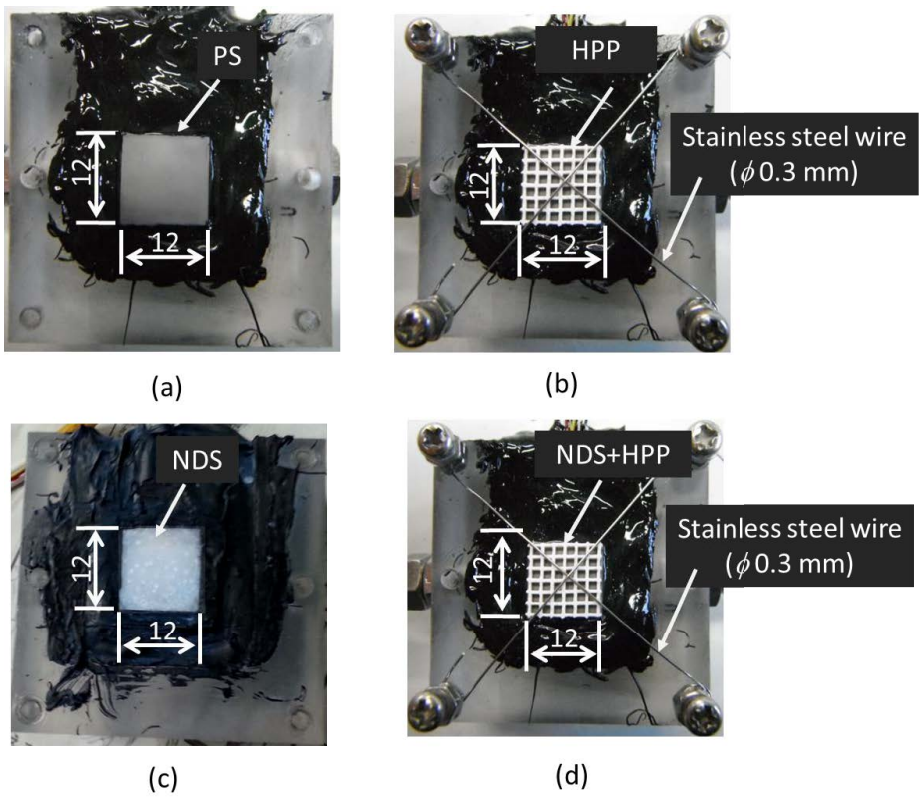

Figure 4-4 Heated surface modifications: (a) PS, (b) HPP, (c) NDS, and (d) NDS+HPP.

4.3.5 Uncertainty analysis

Individual standard uncertainties were combined to estimate the standard deviation of the results, which was calculated using the law of the propagation of uncertainty (Taylor & Kuyatt, 1994). The heat loss from a ceramic heater through the side opposite the heat transfer surface and the silicon sealant and polycarbonate on the other sides were estimated to be less than 0.2%. The uncertainty in the heat flux q due to errors in the voltage, current, and heated surface area was found to be less than 5%. Additionally, the uncertainties in the

nanofluid measurements and the angles of inclination of the heaters were approximately ±5 mg and ±0.5°, respectively.

4.4 Results and discussion

In the present study, the effect of the orientation of a heater with surface modifications on the CHF was experimentally investigated under saturated and atmospheric pressure conditions. All experiments for each type of heater surface modification were performed at least three times to ensure repeatability.

4.4.1 CHF of plain surface

Pool boiling CHF experiment is conducted with a PS, and the CHF obtained at each angle of inclination was normalized by the CHF at $\theta = 0°$. The measured CHFs are compared with correlations by Chang & You (1996), Guo and El-Genk (1992), Liao et al. (2008) and Priarone (2005) and experimental data from previous studies by other researchers such as Kwark et al. (2010), Sakashita et al. (2009) and Ono & Sakashita (2007) as shown previous in Figure 4-1. The four correlations considered above are applicable from upward-facing $0°$ to downward-facing $180°$.

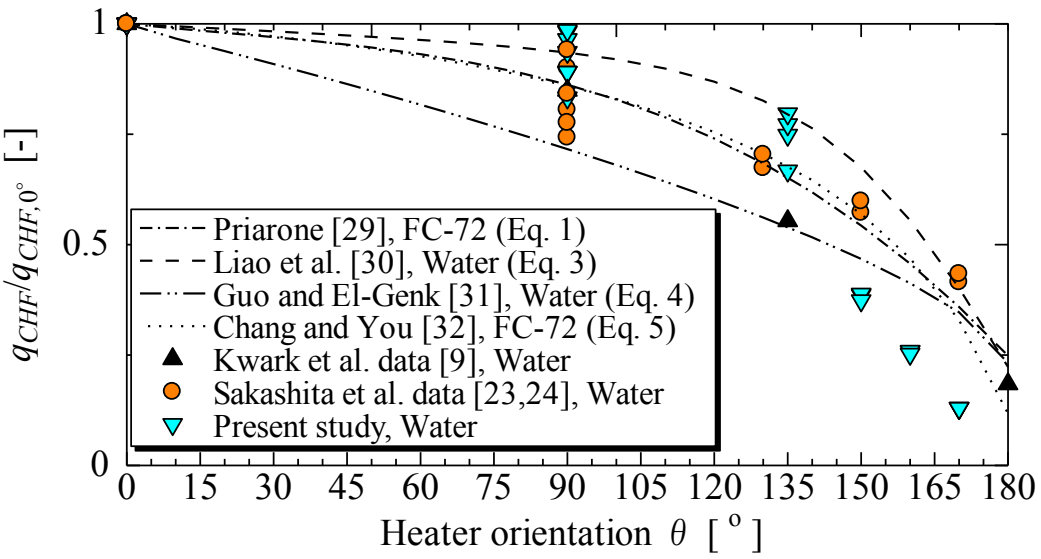

Figure 4-5 Comparison of current experimental data with previously developed correlations and earlier experimental data by other researchers.

As shown in Figure 4-5 the measured CHF in the present study decreases as the angle of inclination of the surface heater increases which is similar to predicted by others. In general, it is hard for the coalesced bubbles to detach from the inclined heater surface because bubbles below heated surfaces tended to be stagnant. Hence, the CHF decreases substantially as the orientation approaches downward-facing. All in all, decreasing trend shown in our results are comparable with other literature.

4.4.2 CHF enhancement by honeycomb porous plate attachment and nanoparticle deposition surface and its combination

Figure 4-6(a) shows the CHFs for heater surfaces with different modifications and angles of inclination ranging from 0° to 180°. Regardless of the type of present heater surface modification, the CHF decreased as the orientation approached downward-facing. The CHF at an angle of inclination of 0° for the HPP (approximately 1.3 MW/m^2) does not agree with

the results of previous chapters, which reported CHFs of 2.2 MW/m^2, twice that for the plain heated surface (1.0 MW/m^2). This differences may be because the heated surface material and heating conditions were different; namely, the ceramic heater is used rather than copper, and the current experiment is conducted under uniform heat flux conditions rather than isothermal conditions. The experimental results are shown in Figure 4-6(a) indicate that the NDS+HPP shows a significant CHF enhancement compared with the other three surfaces, regardless of the heater orientation angle. Surprisingly, the CHF of NDS+HPP at 180° is greater than upward-facing 0° of PS. It should be noted that data could not be obtained for the PS at 180°. Because the vapor generated on the heater surface continually grew and accumulated below the heated surface, steady state conditions could not be achieved once heating began.

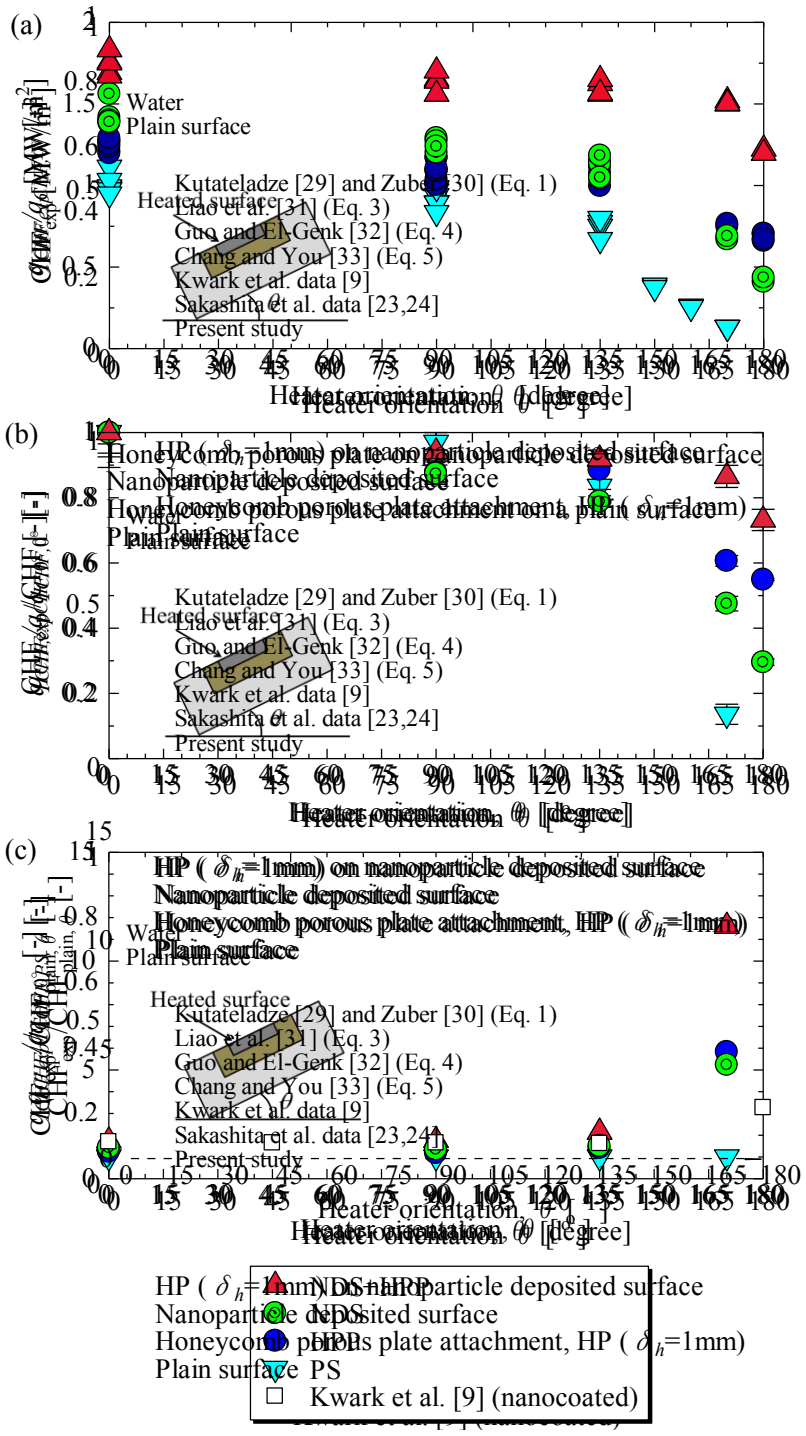

Figure 4-6 Effects of heater orientation and heater surface modifications on CHF.

Figure 4-6(b) shows the dependence of the CHF on the inclination angle, with all values normalized by that at 0°. It can be seen that as the angle increases, the CHF is more strongly dependent on the type of surface modification. The NDS+HPP is most effective at suppressing the decrease in CHF with increasing angle, followed by the HPP and the NDS. Figure 4-6(c) shows the CHF relative to the value for the PS for different heater orientation angles. Data from Kwark et al. (2010) are also shown in this figure. For the NDS+HPP, the CHF enhancement becomes greater with increasing orientation angle, particularly at 170° with 11.6 times compared to PS. To the best of the authors' knowledge, the largest enhancement this study is the first of its kind.

Assuming uniform energy generation per unit volume within the heater and adiabatic conditions at heater surface on the opposite side of the boiling surface, the temperature of the boiling heat transfer surface can be estimated from the temperature measured by T.C.1 underneath the ceramic heater using the heat equation. After that, the superheat ΔT_{sat} and heat transfer coefficient h can be determined. The results for 0° and 170° are shown in Figure 4-7(a) and Figure 4-7(b), respectively.

At 0°, the boiling curve for the HPP shifts to the left of that for the PS, which means the heat transfer coefficient for the HPP is higher than that for the PS. At $\Delta T_{sat} = 10$ K, the HPP has the highest heat transfer coefficient, followed by the PS, the NDS+HPP, and the NDS. For NDS, this is a result of the increase in the thermal resistance caused by the nanoparticle deposition layer on the heated surface.

At 170°, all surfaces showed a decrease in heat transfer coefficient in comparison with that at 0°. A similar observation was reported by Zhong et al. (2015); in their study, the

heat transfer coefficient decreased at a given wall superheat as the orientation changed from vertical (90°) to downward-facing (175°).

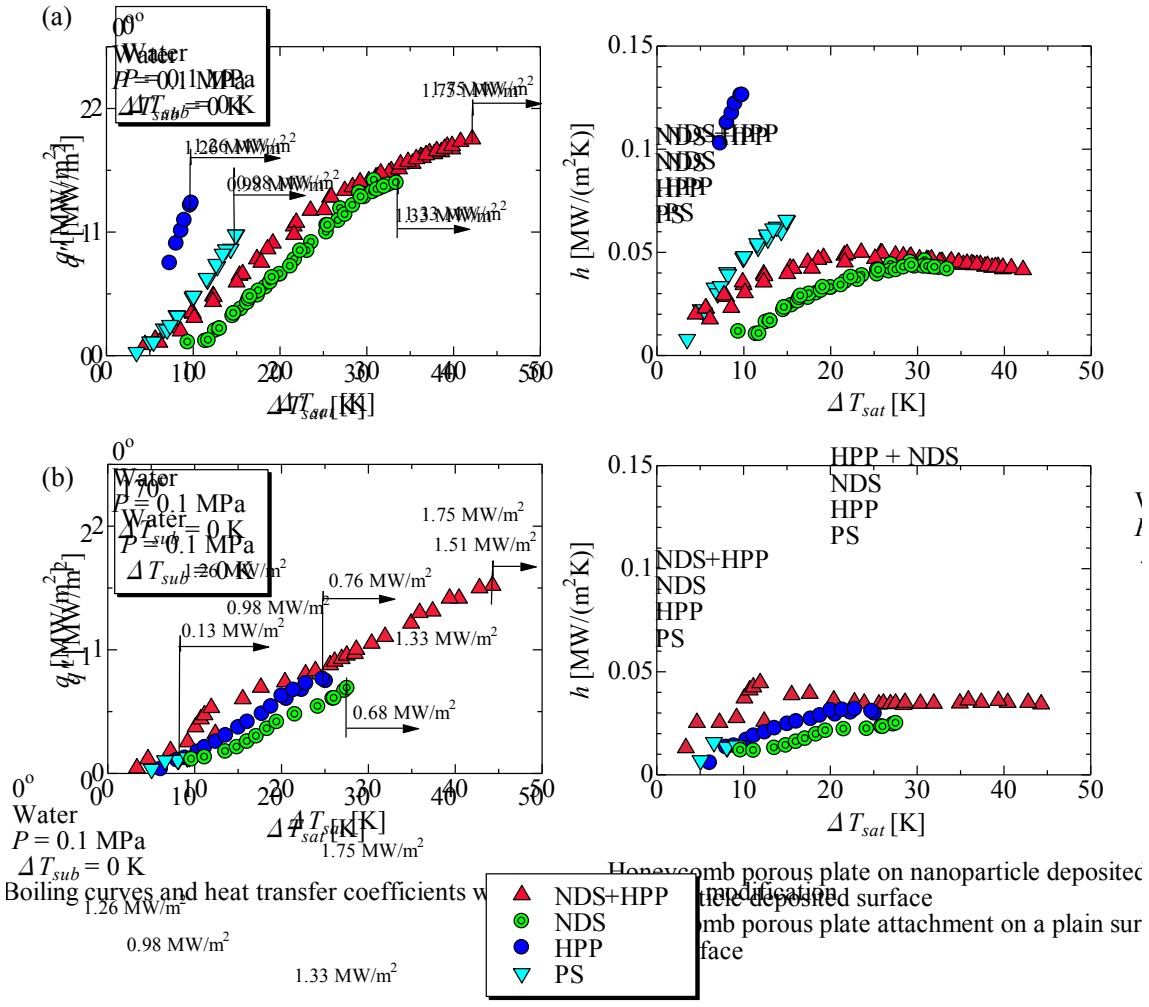

Figure 4-7 Boiling curves and heat transfer coefficients for surfaces with different modifications at (a) 0° and (b) 170°.

4.4.2.1 Hovering period of coalesced bubbles

A high-speed camera is used to capture the boiling behavior at 4000 fps from low to high heat flux under steady state conditions. The hovering period is determined by

periodically counting the number of coalesced bubbles departing from the heated surface at intervals of 5 s for angles of inclination of 0° and 170°, respectively.

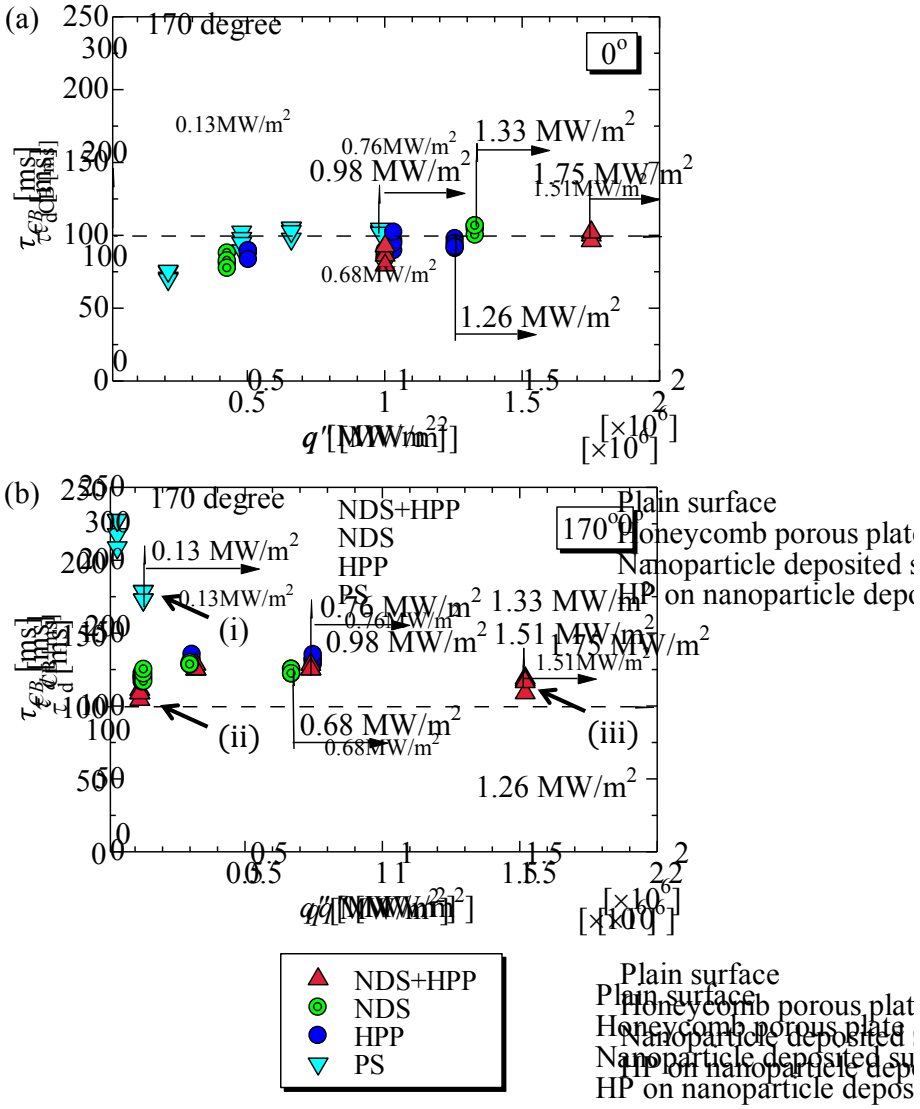

Figure 4-8 Comparison of the coalesced bubble hovering period for surfaces with different modifications at (a) 0° and (b) 170°.

Figure 4-8 compares the hovering period τ_{CB} of coalesced bubbles for heated surfaces with different modifications at 0° and 170°. The CHFs for each type of surface modification are also indicated by the arrows in the figure. As shown in Figure 4-6(c), the

enhancement of the CHF by surface modification was much greater for an orientation of 170° than for an upward-facing heated orientation (0°). Therefore, this section focuses on the effect of the orientation on boiling behavior, specifically the hovering period of coalesced bubbles, for orientations between 0° and 170°.

At 0°, as the heat flux increased, τ_{CB} increased gradually and approached approximately 100 ms regardless of the type of surface modifications. These results clearly indicate that the surface modifications considered in this study (HPP attachment and NDS) have no significant effect on τ_{CB}. However, at 170°, the hovering period of coalesced bubbles for the PS (τ_{CB} = 170 ms) is nearly 1.4 times that for the modified surfaces (τ_{CB} = 120 ms) at q = 0.13 MW/m^2.

At low heat flux (0.13 MW/m^2), comparison of boiling behavior at steady state condition between PS and NDS+HPP, corresponding to the points labeled (i) and (ii), respectively, in Figure 4-8(b) are shown in Figure 4-9. The images revealed that even under the same heat flux, coalesced bubble forming on the PS is larger and takes a longer time to detach from the heated surface than those forming on the NDS+HPP. Regarding (i), due to buoyancy, the coalesced bubble is tending to be stagnant below the heated surface and entirely covering the heated surface, which resulted in hindering the liquid supply. Therefore, the CHF is greatly decreased. On the other hand, regarding (ii), in the early stages, isolated vapor bubbles are observed to escape through HPP cells. It can be noticed the coalesced bubble is not entirely covering the heated surface as in (i) and smoothly detached from the heated surface.

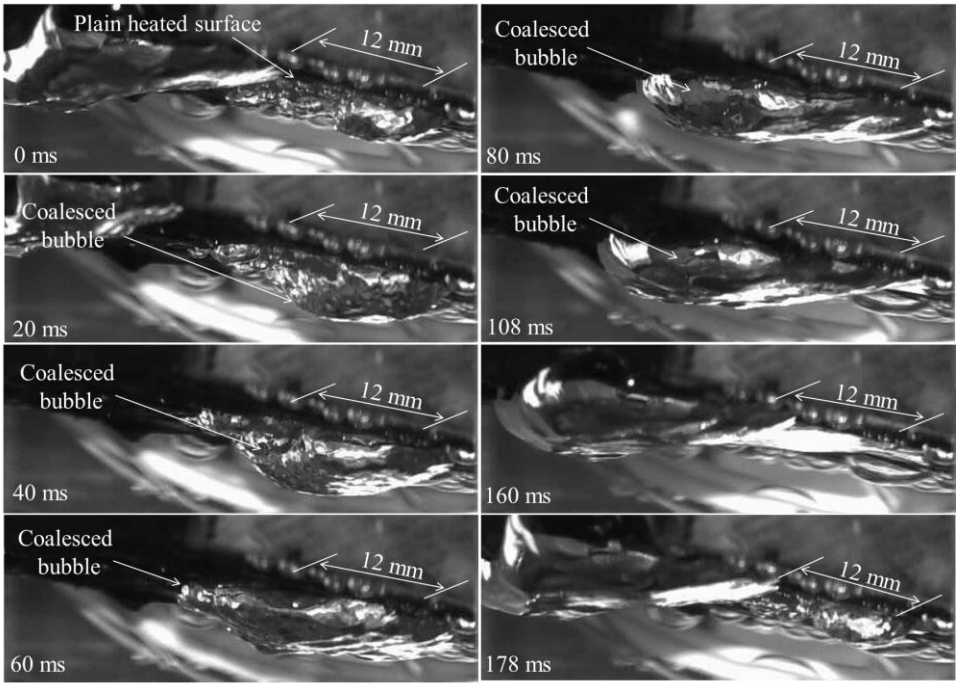

(a) PS

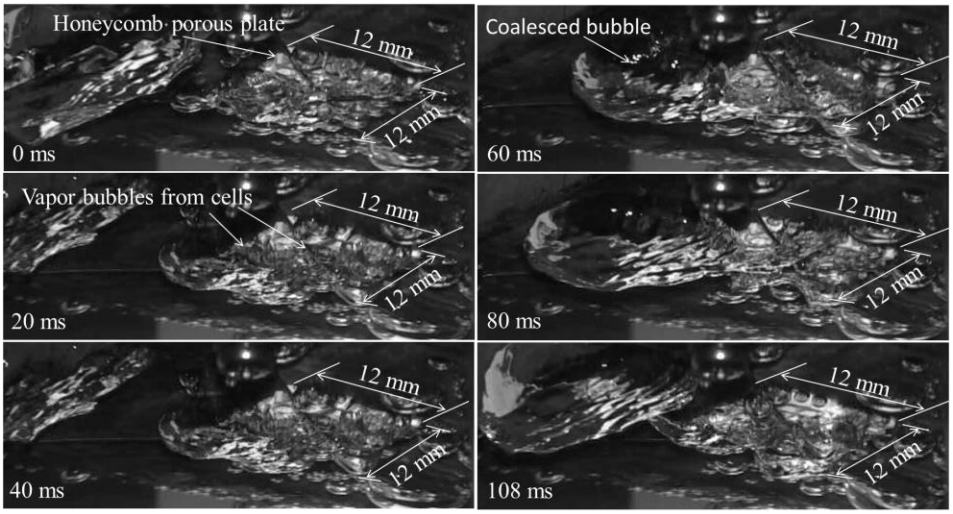

Figure 4-9 Boiling configuration for (a) PS ((i) in Fig. 7(b)) and (b) NDS+HPP ((ii) in Fig. 7(b)) at 170° and q = 0.13 MW/m^2.

Figure 4-10 shows the boiling configuration at q_{CHF} =1.51 MW/m^2 on NDS+HPP at 170° corresponding to the point labeled (iii) in Figure 4-8(b). At high heat flux, the

moment coalesced bubble detaches the heated surface at 0 ms, isolated vapor bubbles are observed growing below the heated surface. Then, the heated surface is entirely covered by coalesced bubble and detaches at about 132 ms.

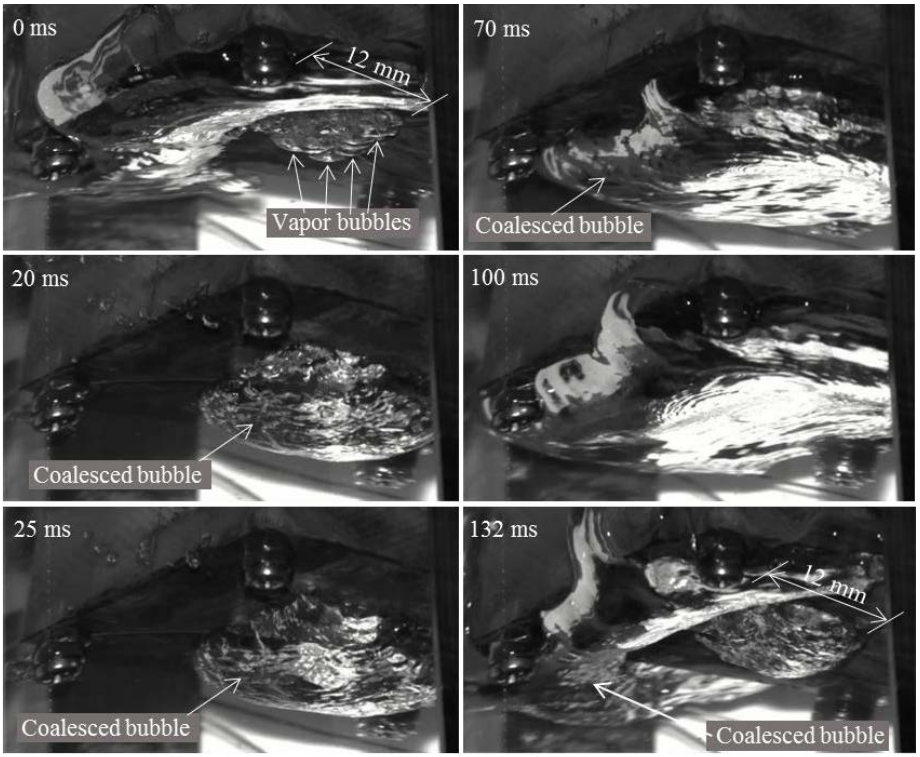

Figure 4-10 Boiling configuration for NDS+HPP ((iii) in Fig. 7(b)) at 170° and q_{CHF} = 1.51 MW/m^2.

Figure 4-11 shows the detailed growth of vapor bubbles below the heated surface just before and after the detachment of coalesced bubble from heated surface of Figure 4-10. At -4 ms the coalesced bubble starts leaving and moving along the heated surface. Simultaneously, isolated vapor bubbles emerge below the heated surface. During this time, it is possible that liquid is supplied to the gap of isolated bubbles to the heated surface through HPP. These bubbles keep growing until coalesced bubble is formed at about 4 ms.

From this observation, it implies the liquid is supplied to the heated surface at the instant of coalesced bubble detaching the heated surface. The liquid is spread instantaneously on the heated surface by NDS with the aid of capillary action. The amount of water supplied during this process is accountable for CHF enhancement for NDS+HPP.

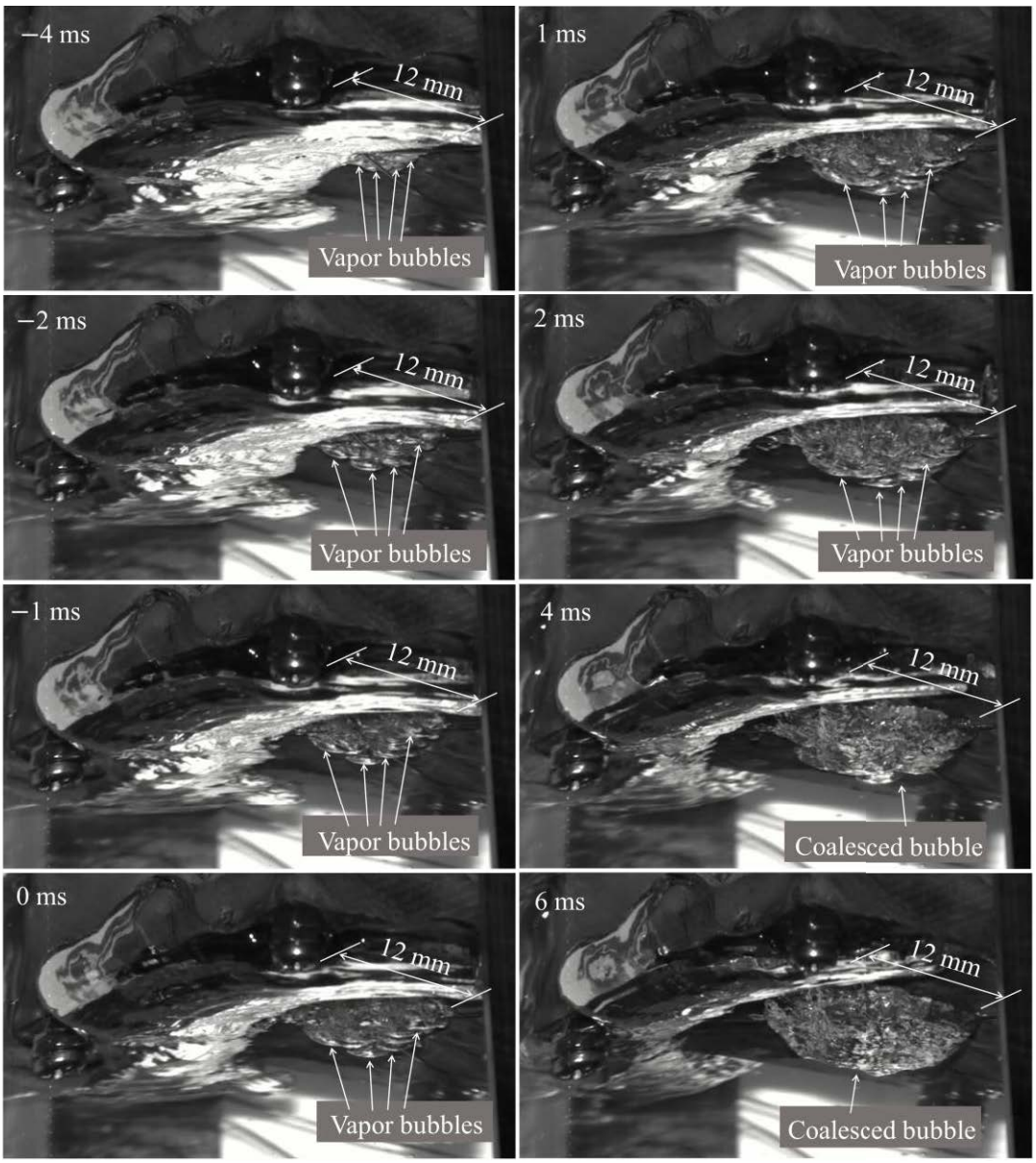

Figure 4-11 Vapor bubbles growth before and after coalesced bubble leaves the heated surface at q_{CHF} = 1.51 MW/m^2 for NDS+HPP.

Haramura and Katto (1983) proposed a macrolayer dryout model which considering the existence of a thin liquid macrolayer underneath coalesced bubble. CHF occurs when the liquid macrolayer is completely evaporated during the coalesced bubble hovering period.

With the same assumption, if the water inside the porous material is dried out during the hovering period of coalesced bubble, the CHF should occur. To clarify it for the case of NDS+HPP in both heater orientation 0° and 170°, either the CHF occurs due to the dryout phenomenon, the following discussion is made.

In order to estimate the time for drying liquid inside HPP under the q_{CHF} condition, considering the conservation of energy, the following equations can be obtained:

$$q_{CHF}\tau_{dryout}A = \rho_l V_p h_{fg}, \tag{4-6}$$

$$V_p = \varepsilon A_w \delta_h. \tag{4-7}$$

where V_p is the estimated maximum volume of water in HPP. From these equations, Eq. (8) and Eq. (9) yielding the following estimation of the dryout time of liquid inside a porous material:

$$\tau_{dryout} = \frac{\varepsilon A_w \delta_h \rho_l h_{fg}}{q_{CHF}A}. \tag{4-8}$$

Substituting the appropriate values into Eq. (10) yields τ_{dryout} to be 136 ms and 158 ms at 0° and 170°, respectively. At both angles of inclination, τ_{dryout} was larger than the experimentally obtained hovering period of approximately 100 ms. This means that the CHF mechanism is not related to the dryout phenomenon inside a porous material for any heater orientation. In Figure 4-11, at about 4 ms, coalesced bubble is formed and may hinder liquid supply to rewet the heated surface.

4.4.2.2 Surface wettability of nanoparticle deposited surface

From experimental results in Figure 4-6(a), regardless of any heater orientation, it is observed that CHF enhancement of NDS+HPP is more than HPP. The differences between these two surface modifications are with or without nanoparticle deposition surface, and it indicates CHF enhancement for NDS+HPP is caused by not only HPP but also NDS.

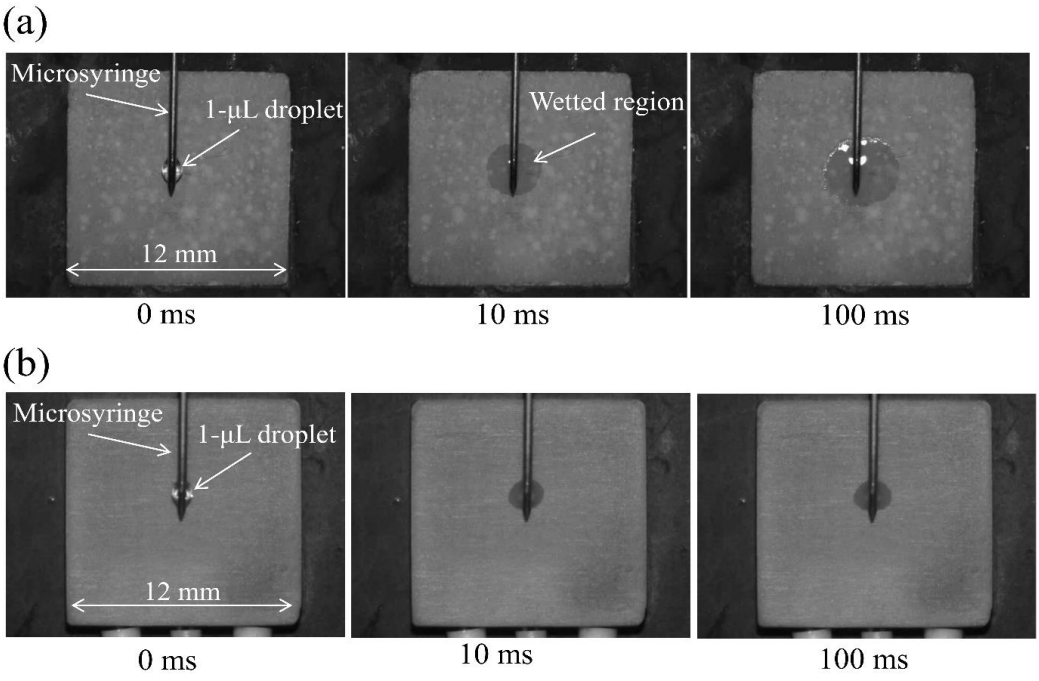

Figure 4-12 Images of droplets spreading on (a) NDS and (b) PS at 0, 10, and 100 ms.

CHF enhancement by HPP is mainly due to liquid supply to the heated surface as a result of (1) capillary suction and (2) inflow of liquid through vapor escape channel directly from bulk (Mori & Okuyama, 2009). In the case of NDS+HPP, the liquid is instantaneously spread out on heated surface by nanoparticle deposition layer through vapor escape channel (mechanism (2)) once liquid contacted with the heated surface. For this reason, CHF of NDS+HPP is enhanced rather than HPP. Therefore, to clarify the effect of nanoparticle

deposition on the dynamic wettability of the heated surface, a simple droplet spreading experiment has been performed.

The PS and NDS were used as test surfaces. A 1-μl droplet of distilled water was gently placed on the test surfaces using a microsyringe, and the wetting phenomenon was recorded by a high-speed camera at 4000 fps. The test was repeated four times for each surface. Figure 4-12 shows images of droplet spreading on the NDS and PS for 0, 10, 100 ms after droplet placement. At selected times, the wetted area was determined using motion analysis software, and the wetted radius was calculated.

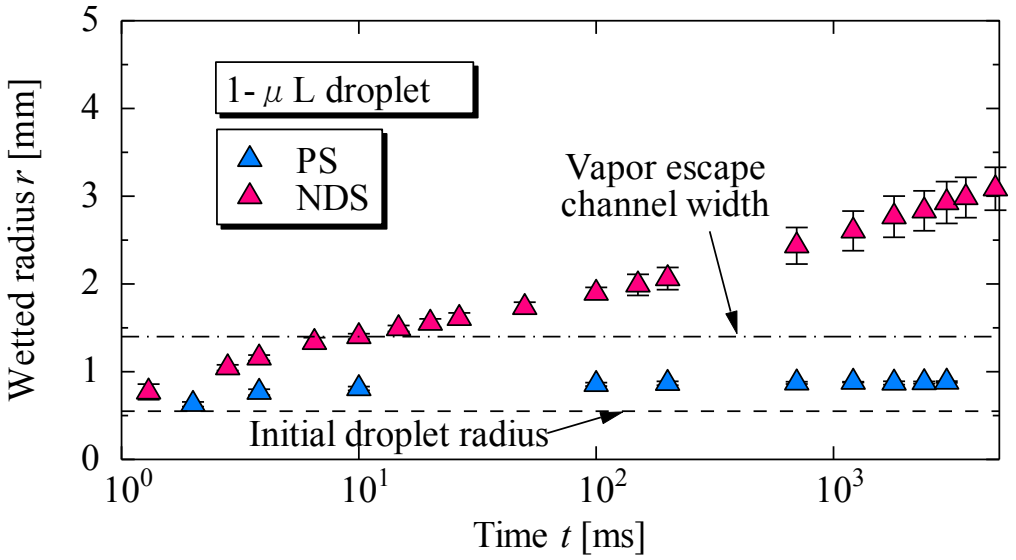

Figure 4-13 Wetted radius as a function of time for PS and NDS.

Figure 4-13 compares the droplet spreading on the PS and NDS in terms of the wetted radius against time. The initial radius of the droplet (0.55 mm) and the vapor escape channel width (1.4 mm) are also plotted in the figure for reference. Figure 4-13 clearly shows that the wetted radius increased steadily on the NDS but remained nearly constant on the PS. These results indicate that the surface modification of nanoparticle deposition changes

the wettability profile of the surface. In this case, the 1-μl droplet of water was able to spread out on the heated NDS below the vapor escape channel (width 1.4 mm) in 10 ms. The increased surface roughness caused by nanoparticle deposition also contributes to the enhanced surface wettability (H. D. Kim, Kim, & Kim, 2007). The enhancement of the wettability enables immediate rewetting, thus counteracting the dryout phenomenon. Therefore, the increased wettability of the heated surface helps to delay the CHF by rewetting dry spots. The continued supply of liquid by the capillary action of the HPP and the instantaneous liquid spreading on NDSs may explain the significant enhancement observed in the NDS+HPP.

4.4.2.3 CHF enhancement mechanism of honeycomb porous plate on nanoparticle deposited surface

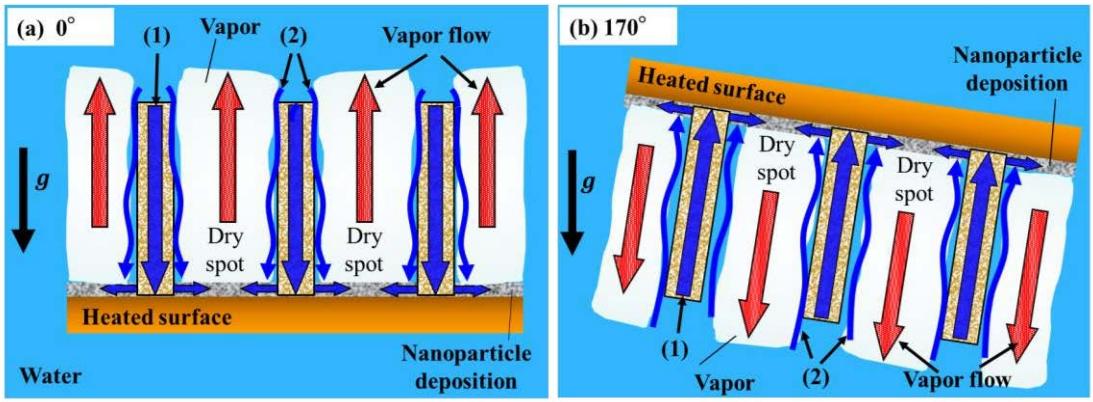

Figure 4-14 Schematic diagram of water and vapor flow near the heated surface at (a) 0° and (b) 170°.

Figure 4-14 shows the mechanisms for supplying liquid to the heated surface for the NDS+HPP at 0° and 170°. Liquid supply mechanism (1) corresponds to liquid driven by

capillary action flowing from the bulk liquid to the heated surface of the porous material. Conversely, liquid supply mechanism (2) corresponds to liquid driven by gravity flowing toward the heated surface through the vapor escape channel.

These two mechanisms ensure liquid is supplied to the heated surface. However, as the angle of inclination increases from 90° to 180°, the generated vapor tends to accumulate below the heated surface; hence, the amount of water available to rewet the heater surface is reduced because of the increase in τ_{CB} (Figure 4-8(b)). Nanoparticle deposition facilitates the more rapid spreading of the liquid (liquid supply mechanism (3) in Figure 4-14) on the heated surface by mechanism (1) and (2) from bulk liquid to HPP, hence delaying the occurrence of the dryout occurrence.

Therefore, the largest CHF achieved in the present study can be obtained for all heater orientations with the NDS+HPP. Regardless of the heater orientation, the contribution of the HPP to CHF enhancement can be anticipated because the capillary action is not affected by gravity. This capability may explain the minimal decline in the CHF obtained with the NDS+HPP. The difference between the CHFs at different heater orientations (0° and 170°) may cause by the liquid supplied by gravity to the heated surface through vapor escape channels.

4.5 Conclusion

In this chapter, the effect of heater orientation on the CHF was experimentally investigated for four different surfaces (PS, HPP, NDS, and NDS+HPP) under saturated and atmospheric pressure conditions. The following conclusions were obtained.

(1) In general, the CHF decreased as the orientation of the heater surface changed from upward- to downward-facing. However, the amount of CHF reduction depends on the surface modification, and the NDS+HPP was the most effective at suppressing this decline. The CHF enhancement was more significant at higher heater inclination angles approaching 180° and was approximately 12 times that for the PS at 170°.

(2) The combined effects of the HPP attachment and nanoparticle deposition are key to improving CHF performance. The HPP plays a major role in supplying water to the heated surface by capillary action, whereas the NDS is responsible for instantaneously spreading the liquid over the heated surface because of its good wettability and capillarity. A high heat flux removal in IVR could be realized by modifying the surface through HPP attachment and nanoparticle deposition.

Chapter 5 Conclusion

5.1 Conclusion of this study

Experiment in this study has been carried out to enhance the CHF in pool boiling under saturated and atmospheric conditions. This effort is relevant with the global demand that requires a new cooling technology for a high heat flux removal. For example, in IVR method in the nuclear industries. Combination effects of surface modification by honeycomb porous plate, nanofluid, square-shaped metal structure, and the combination of this element have been investigated.

In Chapter 1, the background of this study, mainly the knowledge of proposed CHF mechanism from a few prominent scholars is reviewed. An investigation by other researchers to enhance CHF and its mechanism in the literature is introduced and discussed. Especially, CHF enhancement method using nanofluid and the recently proposed technique using honeycomb porous plate. The problem statement that driven this study and the research objectives are outlined.

In Chapter 2, pool boiling experiments were conducted with surface modification by nanoparticle deposited surface, honeycomb porous plate and its combination to examine the effect of the heated surface size. The nanoparticle deposited surface is prepared earlier using

a low concentration of water-based nanofluid, 0.001 vol.%. The heater surfaces are ϕ10 mm, ϕ 30 mm and ϕ 50 mm were selected to examine the characteristic hydrodynamic length which represents dimensionless heater lengths of the heater size, L' are 4, 12 and, 20 respectively. The heater with $L' = 20$ can be regarded as infinite heater surface. The following conclusion were obtained.

(1) Nanoparticle deposition formed during vapor bubbles evaporate on the heater surface. This changes the surface roughness resulting in increasing the wettability. However, the heat transfer coefficient is degraded the deposition surface due to an increase of thermal resistance.

(2) While honeycomb porous plate attachment shows an enhancement for both CHF and boiling heat transfer at each heater size.

(3) For each surface modification, CHF is verified to decrease with the increase of heater size. These results have been predicted earlier by rewetting resistance getting bigger with the increase of heater surface.

(4) The best performing surface modification is confirmed to be a honeycomb porous plate installed on a nanoparticle deposited surface. Under the best performing surface modifications, the CHF for 10 mm, 30 mm and 50 mm in diameter surfaces is enhanced up to 3.1, 2.3, and 2.2 MW/m^2, respectively.

In Chapter 3, two techniques are proposed to increase CHF further. Both of the techniques considers the surface modification by honeycomb porous plate and nanofluid as a working fluid. However, with different heated surface size. The first technique focused on ϕ30 mm heated surfaces and the second technique focused on ϕ 50 mm heated surface. In

the first technique, two types of water-based nanofluid concentrations were used to demonstrate a low concentration, 0.001 vol.% (0.004 g/L) and a high concentration, 0.1 vol.% (4.0 g/L). For the first technique, the following conclusions are obtained as follow.

(1) There was a concern that micropores in the honeycomb porous plate may have become clogged with nanoparticles, resulting in a decrease in the CHF. Therefore, a durability test to determine the cooling capability of a honeycomb porous plate in saturated pool boiling of a nanofluid was performed. As a result, for a constant heat flux at 1.8 MW/m^2, no CHF is observed for more than two hours with a high concentration of water-based nanofluid 0.1 vol.% (4 g/L).

(2) The CHF increased as the nanoparticle concentration increased. The CHF is enhanced significantly up to 3.2 MW/m^2 at maximum for 0.1 vol.% nanofluid. To the best of the author's knowledge, the highest value of CHF (3.2MW/m^2) was obtained for a large heated surface having a diameter of more than 30 mm.

(3) The heat transfer coefficient with a honeycomb porous plate decreased by the increase in the nanoparticle concentration.

(4) Detailed SEM observation beneath the surface of a honeycomb porous plate in contact with the heated surface revealed microchannels of several tens of microns in width just below the honeycomb porous plate. These microchannels may act as vapor escape channels for CHF enhancement.

For the second technique, besides heater surface modification by honeycomb porous plate and nanofluid, the square-shaped metal structure is adopted. The experiment was conducted

using water and high concentration of nanofluid (0.1 vol.%) under saturated and atmospheric conditions with a large heater surface (ϕ 50 mm). The following conclusions were obtained:

(1) Attachment of a square-shaped metal structure on a plain surface in water boiling shortens the hovering period of coalesced bubble compared to the plain surface at the same heat flux (1.0 MW/m^2). Therefore, more water supply is sustained during the detachment of the coalesced bubble.

(2) The combination of a square-shaped metal structure and honeycomb porous plate attachment on a plain surface increases CHF to 2.0 MW/m^2. Additionally, heat transfer coefficient is improved due to more active nucleation site density underneath porous part that is attached to the heater surface is activated effectively.

(3) Nanoparticle deposition during the boiling process significantly improves wettability and capillarity on the heated surface. Hence the dry out region is delayed, and further CHF enhancement is observed.

(4) The combination of a honeycomb porous plate and square-shaped metal structure in a high concentration of water-based nanofluid could remove high heat flux up to 3 MW/m^2.

CHF enhancement that is achieved in Chapter 2 and Chapter 3 is compared to previous studies and summarized in Figure 5-1. From the figure, the combination of honeycomb porous plate, nanofluid and square-shaped metal structure could remove a high heat flux on a large heated surface (ϕ 50 mm or $L' = 20$). Therefore, this method could be review as a new cooling technology in the future.

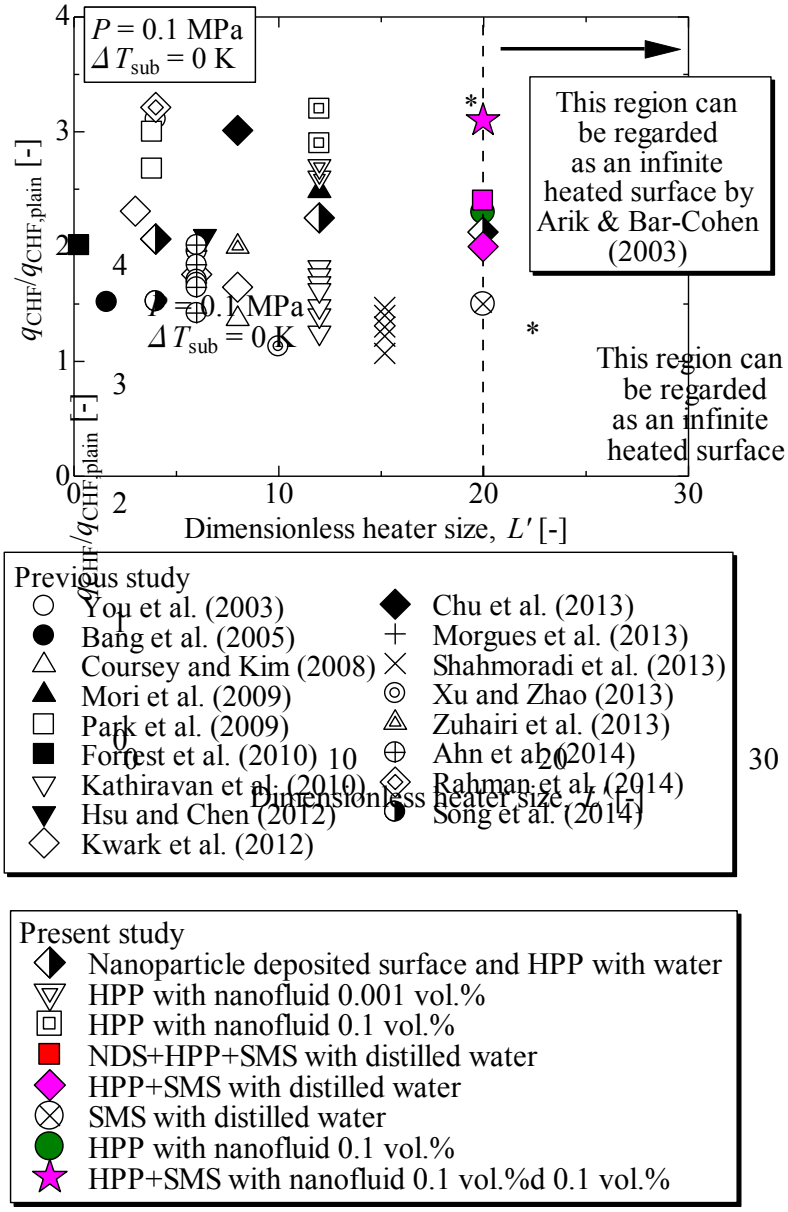

Figure 5-1 Achievement of CHF enhancement in the present study compared to the previous study in literature.

In Chapter 4, the effect of heater orientation on the CHF was experimentally investigated for four different surfaces, namely, plain surface (PS), honeycomb porous plate attachment (HPP), nanoparticle deposited surface (NDS) and a combination of honeycomb

porous plate and nanoparticle deposited surface (NDS+HPP) under saturated and atmospheric pressure conditions. The following conclusions were obtained.

(1) In general, the CHF decreased as the orientation of the heater surface changed from upward- to downward-facing. However, the amount of CHF reduction depends on the surface modification, and the NDS+HPP was the most effective at suppressing this decline. The CHF enhancement was more significant at higher heater inclination angles approaching 180° and was approximately 12 times that for the PS at 170°.

(2) The combined effects of the HPP attachment and nanoparticle deposition are key to improving CHF performance. The HPP plays a major role in supplying water to the heated surface by capillary action, whereas the NDS is responsible for instantaneously spreading the liquid over the heated surface because of its good wettability and capillarity. A high heat flux removal in IVR could be realized by modifying the surface through HPP attachment and nanoparticle deposition.

5.2 Future work

The attachment of honeycomb porous plate on the heated surface, in the beginning, show a great deal of CHF enhancement. The CHF was 2.5 MW/m^2 which about 2.5 times compared to a plain heated surface (1.0 MW/m^2) in a water pool boiling under saturated and atmospheric condition. These results have been reported by Mori and Okuyama (2009; 2010). During a severe accident in nuclear power plant, in-vessel retention (IVR) method is among measurement taken to cool down reactor pressured vessel (RPV) in light water reactors (LWRs). In order to increase the capability of the IVR, it is crucial to increase the

CHF. Therefore, the present study started adopting water-based nanofluid because a big number of studies have shown promising results. As a result, CHF was enhanced to 3.2 MW/m^2 with a combination of honeycomb porous plate attachment in nanofluid boiling (0.1 vol.%). This CHF enhancement is about 3.2 times compared to that a plain surface.

It was shown that the CHF could be enhanced with the combination of honeycomb porous plate and nanofluid. However, thorough studies need to be done to put this method into practicality. Ideally, the experiment conditions in the laboratory scale should reflect the actual IVR conditions. For example, heater surface of RPV is curved, and the orientations are from vertical to downward facing. The cooling by boiling at the outer surface of RPV is changing depends on parameters such as the water level in the cavity, pressures, and mass fluxes. Honeycomb porous plate used in the study is fragile and will face a difficult situation to fix it on a large heater surface. Moreover, if the heated surface is having inclination angle and a curved surface, the attachment of a porous plate will become harder.

The present study managed to perform experiments to examine the effect of heater surface sizes (reported in Chapter 1), honeycomb porous plate attachment in two types of nanofluid concentration and attachment of square-shaped metal structure (reported in Chapter 3), and heater surface orientation (reported in Chapter 4). All experiments have been performed under saturated pool boiling and atmospheric condition.

It is important to understand the enhancement contributed by the honeycomb porous plate and the nanofluid. Boiling experiment using a transparent ITO thin heater to observe the development of dry region near to CHF using infrared (IR) camera is in progress. An investigation to examine the effect of heater inclination on CHF performance together with

surface modification by honeycomb porous plate in IVR flow conditions are also in progress. Saturated condition and various quality conditions are considered in this experiment.

Experiments conducted in this study started from a low heat flux, then with a small increment of heat flux until the occurrence of burnout. However, in IVR method, during the emergency state, working fluid is poured into the reactor vessel and the first contact of the liquid with the reactor vessel surface may produce a film boiling. Therefore, quenching experiment should be conducted to investigate the effect of honeycomb porous plate attachment on a film boiling heat transfer.

In the present study, only one type of water-based nanofluid was considered using nanoparticle of titania (TiO_2). It was confirmed at high heat flux 1.8 MW/m^2; the experiment could endure for more than two hours with honeycomb porous plate attachment in a high concentration of nanofluid boiling (0.1 vol.%). This result indicates that the liquid supply by capillary action remains intact and no clogged of nanoparticles into the porous plate. However, the applicability of another nanofluid with other nanoparticles such as alumina and sea water has not been verified yet and should be carried out.

References

Ahn, H. S., & Kim, M. H. (2013). The boiling phenomenon of alumina nanofluid near critical heat flux. *International Journal of Heat and Mass Transfer*, *62*, 718–728. http://doi.org/10.1016/j.ijheatmasstransfer.2013.03.054

Ahn, H. S., Lee, C., Kim, J., & Kim, M. H. (2012). The effect of capillary wicking action of micro/nano structures on pool boiling critical heat flux. *International Journal of Heat and Mass Transfer*, *55*(1–3), 89–92. http://doi.org/10.1016/j.ijheatmasstransfer.2011.08.044

Aoki, K., Iwaki, C., Sato, H., Mimura, S., & Kanamori, D. (2015). Testing Plan for Critical Heat Flux Measurement During In-Vessel Retention. In *Proceedings of ICONE-23* (pp. 1–5).

Arik, M., & Bar-Cohen, A. (2003). Effusivity-based correlation of surface property effects in pool boiling CHF of dielectric liquids. *International Journal of Heat and Mass Transfer*, *46*(2003), 3755–3764. http://doi.org/10.1016/S0017-9310(03)00215-1

Bang, I. C., & Heung Chang, S. (2005). Boiling heat transfer performance and phenomena of Al2O3–water nano-fluids from a plain surface in a pool. *International Journal of Heat and Mass Transfer*, *48*(12), 2407–2419. http://doi.org/10.1016/j.ijheatmasstransfer.2004.12.047

Buongiorno, J., Hu, L. W., Apostolakis, G., Hannink, R., Lucas, T., & Chupin, A. (2009). A feasibility assessment of the use of nanofluids to enhance the in-vessel retention capability in light-water reactors. *Nuclear Engineering and Design*, *239*, 941–948. http://doi.org/10.1016/j.nucengdes.2008.06.017

Carey, V. P. (2008). *Liquid-Vapor Phase-Change Phenomena: An Introduction to the*

Thermophysics of Vaporization and Condensation Processes in Heat Transfer Equipment, Second Edition (2nd ed.). Taylor & Francis.

Chang, J. Y., & You, S. M. (1996). Heater Orientation Effects on Pool Boiling of Micro-Porous-Enhanced Surfaces in Saturated FC-72. *Journal of Heat Transfer*, *118*(4), 937–943. http://doi.org/10.1115/1.2822592

Chu, K. H., Joung, Y. S., Enright, R., Buie, C. R., & Wang, E. N. (2013). Hierarchically structured surfaces for boiling critical heat flux enhancement. *Applied Physics Letters*, *102*(15). http://doi.org/10.1063/1.4801811

Cie, J. T. (2002). Nucleate pool boiling on porous metallic coatings ski. *Experimental Thermal and Fluid Science*, *25*, 557–564.

Coursey, J. S., & Kim, J. (2008). Nanofluid boiling: The effect of surface wettability. *International Journal of Heat and Fluid Flow*, *29*(6), 1577–1585. http://doi.org/10.1016/j.ijheatfluidflow.2008.07.004

Forrest, E., Williamson, E., Buongiorno, J., Hu, L.-W., Rubner, M., & Cohen, R. (2010). Augmentation of nucleate boiling heat transfer and critical heat flux using nanoparticle thin-film coatings. *International Journal of Heat and Mass Transfer*, *53*(1–3), 58–67. http://doi.org/10.1016/j.ijheatmasstransfer.2009.10.008

Gambill, W. R., & Lienhard, J. H. (1989). An upper bound for the critical boiling heat flux. *Journal of Heat Transfer*, *111*, 815–818. http://doi.org/10.1115/1.3250759

Guo, Z., & El-Genk, M. S. (1992). An experimental study of saturated pool boiling from downward facing and inclined surfaces. *International Journal of Heat and Mass Transfer*, *35*(9), 2109–2117. http://doi.org/10.1016/0017-9310(92)90056-X

Haramura, Y., & Katto, Y. (1983). A new hydrodynamic model of critical heat flux, applicable widely to both pool and forced convection boiling on submerged bodies in saturated liquids. *International Journal of Heat and Mass Transfer*, *26*(3), 389–399. http://doi.org/10.1016/0017-9310(83)90043-1

Howard, A. H., & Mudawar, I. (1999). Orientation effects on pool boiling critical heat flux

(CHF) and modeling of CHF for near-vertical surfaces. *International Journal of Heat and Mass Transfer*, *42*, 1665–1688.

Hsu, C., & Chen, P. (2012). Surface wettability effects on critical heat flux of boiling heat transfer using nanoparticle coatings. *International Journal of Heat and Mass Transfer*, *55*, 3713–3719.

Incropera, F. P., & DeWitt, D. P. (2007). *Fundamentals of Heat and Mass Transfer* (4th ed.). John Willey and Sons.

Jin, Y., Xu, W., Liu, X., & Cheng, X. (2015). In- and ex-vessel coupled analysis of IVR-ERVC phenomenon for large scale PWR. *Annals of Nuclear Energy*, *80*, 322–337. http://doi.org/10.1016/j.anucene.2015.01.041

Kandlikar, S. G. (2001). A Theoretical Model to Predict Pool Boiling CHF Incorporating Effects of Contact Angle and Orientation. *Journal of Heat Transfer*, *123*(6), 1071. http://doi.org/10.1115/1.1409265

Kathiravan, R., Kumar, R., Gupta, A., & Chandra, R. (2010). Preparation and pool boiling characteristics of copper nanofluids over a flat plate heater. *International Journal of Heat and Mass Transfer*, *53*(9–10), 1673–1681. http://doi.org/10.1016/j.ijheatmasstransfer.2010.01.022

Kim, H. D., Kim, J., & Kim, M. H. (2007). Experimental studies on CHF characteristics of nano-fluids at pool boiling. *International Journal of Multiphase Flow*, *33*(7), 691–706. http://doi.org/10.1016/j.ijmultiphaseflow.2007.02.007

Kim, S. J., Bang, I. C., Buongiorno, J., & Hu, L. W. (2007). Surface wettability change during pool boiling of nanofluids and its effect on critical heat flux. *International Journal of Heat and Mass Transfer*, *50*(19–20), 4105–4116. http://doi.org/10.1016/j.ijheatmasstransfer.2007.02.002

Knudson, D. L., Rempe, J. L., Condie, K. G., Suh, K. Y., Cheung, F. B., & Kim, S. B. (2004). Late-phase melt conditions affecting the potential for in-vessel retention in high power reactors. *Nuclear Engineering and Design*, *230*(1–3), 133–150.

http://doi.org/10.1016/j.nucengdes.2003.11.029

Kwark, S. M., Amaya, M., Kumar, R., Moreno, G., & You, S. M. (2010). Effects of pressure, orientation, and heater size on pool boiling of water with nanocoated heaters. *International Journal of Heat and Mass Transfer*, *53*(23–24), 5199–5208. http://doi.org/10.1016/j.ijheatmasstransfer.2010.07.040

Kwark, S. M., Kumar, R., Moreno, G., Yoo, J., & You, S. M. (2010). Pool boiling characteristics of low concentration nanofluids. *International Journal of Heat and Mass Transfer*, *53*(5–6), 972–981. http://doi.org/10.1016/j.ijheatmasstransfer.2009.11.018

Kwark, S. M., Kumar, R., Moreno, G., & You, S. M. (2012). Transient Characteristics of Pool Boiling Heat Transfer in Nanofluids. *Journal of Heat Transfer*, *134*(5), 51015. http://doi.org/10.1115/1.4005706

Kwark, S. M., Moreno, G., Kumar, R., Moon, H., & You, S. M. (2010). Nanocoating characterization in pool boiling heat transfer of pure water. *International Journal of Heat and Mass Transfer*, *53*(21–22), 4579–4587. http://doi.org/10.1016/j.ijheatmasstransfer.2010.06.035

Liao, L., Bao, R., & Liu, Z. (2008). Compositive effects of orientation and contact angle on critical heat flux in pool boiling of water. *Heat and Mass Transfer/Waerme- Und Stoffuebertragung*, *44*(12), 1447–1453. http://doi.org/10.1007/s00231-008-0384-6

Lienhard, J. H., Dhir, V. K., & Riherd, D. M. (1973). Peak Pool Boiling Heat-Flux Measurements on Finite Horizontal Flat Plates. *Journal of Heat Transfer*, *95*, 477–482.

Liter, S. G., & Kaviany, M. (2001). Pool-boiling CHF enhancement by modulated porous-layer coating: theory and experiment. *International Journal of Heat and Mass Transfer*, *44*(22), 4287–4311. http://doi.org/10.1016/S0017-9310(01)00084-9

Mori, S., & Okuyama, K. (2009). Enhancement of the critical heat flux in saturated pool boiling using honeycomb porous media. *International Journal of Multiphase Flow*,

35(10), 946–951. http://doi.org/10.1016/j.ijmultiphaseflow.2009.05.003

Mori, S., Okuyama, K., & Shen, S. (2010). International Heat Transfer Conference 14. In *Effect of Cell Size of a Honeycomb Porous Plate Attached to a Heated Surface on CHF in Saturated Pool Boiling* (pp. 1–11). Washington DC, USA.

Mourgues, A., Hourtané, V., Muller, T., & Caron-Charles, M. (2013). Boiling behaviors and critical heat flux on a horizontal and vertical plate in saturated pool boiling with and without ZnO nanofluid. *International Journal of Heat and Mass Transfer*, *57*, 595–607. http://doi.org/10.1016/j.ijheatmasstransfer.2012.10.073

Mudawar, I., Howard, A. H., & Gersey, C. O. (1997). An analytical model for near-saturated pool boiling critical heat flux on vertical surfaces. *International Journal of Heat and Mass Transfer*, *40*(10), 2327–2339. http://doi.org/10.1016/S0017-9310(96)00298-0

Okawa, T., Takamura, M., & Kamiya, T. (2012). *Boiling time effect on CHF enhancement in pool boiling of nanofluids*. *International Journal of Heat and Mass Transfer* (Vol. 55).

Ono, A., & Sakashita, H. (2004). Liquid-vapor structure near heating surface at high heat flux in subcooled pool boiling. *Transaction of the JSME (B)*, *70*(69), 2951–2957. http://doi.org/10.1016/j.ijheatmasstransfer.2007.01.026

Ono, A., & Sakashita, H. (2007). Liquid–vapor structure near heating surface at high heat flux in subcooled pool boiling. *International Journal of Heat and Mass Transfer*, *50*(17–18), 3481–3489. http://doi.org/http://dx.doi.org/10.1016/j.ijheatmasstransfer.2007.01.026

Park, K., Jung, D., & Eun, S. (2009). Nucleate boiling heat transfer in aqueous solutions with carbon nanotubes up to critical heat fluxes. *International Journal of Multiphase Flow*, *35*(6), 525–532. http://doi.org/10.1016/j.ijmultiphaseflow.2009.02.015

Park, S. D., Lee, S. W., Kang, S., Kim, S. M., & Bang, I. C. (2012). Pool boiling CHF enhancement by graphene-oxide nanofluid under nuclear coolant chemical

environments. *Nuclear Engineering and Design*, *252*, 184–191. http://doi.org/10.1016/j.nucengdes.2012.07.016

Penkavova, V., Tihon, J., & Wein, O. (2011). Stability and rheology of dilute TiO2-water nanofluids. *Nanoscale Research Letters*, *6*(1), 2–7. http://doi.org/10.1186/1556-276X-6-273

Pham, Q. T., Kim, T. I., Lee, S. S., & Chang, S. H. (2012). Enhancement of critical heat flux using nano-fluids for Invessel Retention–External Vessel Cooling. *Applied Thermal Engineering*, *35*, 157–165. http://doi.org/10.1016/j.applthermaleng.2011.10.017

Priarone, A. (2005). Effect of surface orientation on nucleate boiling and critical heat flux of dielectric fluids. *International Journal of Thermal Sciences*, *44*, 822–831. http://doi.org/10.1016/j.ijthermalsci.2005.02.014

Rahman, M. M., Olçeroğlu, E., & McCarthy, M. (2014). Role of wickability on the critical heat flux of structured superhydrophilic surfaces. *Langmuir : The ACS Journal of Surfaces and Colloids*, *30*(37), 11225–34. http://doi.org/10.1021/la5030923

Sakashita, H. (2012). CHF and near-wall boiling behaviors in pool boiling of water on a heating surface coated with nanoparticles. *International Journal of Heat and Mass Transfer*, *55*(23–24), 7312–7320. http://doi.org/10.1016/j.ijheatmasstransfer.2012.07.061

Sakashita, H., Ono, A., & Nyui, J. (2009). Critical Heat Flux and Near-Wall Boiling Behaviors in Saturated and Subcooled Pool Boiling on Vertical and Inclined Surfaces. *Journal of Nuclear Science and Technology*, *46*(11), 1038–1048. http://doi.org/10.1080/18811248.2009.9711614

Shahmoradi, Z., Etesami, N., & Nasr Esfahany, M. (2013). Pool boiling characteristics of nanofluid on flat plate based on heater surface analysis. *International Communications in Heat and Mass Transfer*, *47*, 113–120. http://doi.org/10.1016/j.icheatmasstransfer.2013.06.006

Sharma, A. K., Tiwari, A. K., & Dixit, A. R. (2016). Rheological behaviour of nanofluids: A review. *Renewable and Sustainable Energy Reviews*, *53*, 779–791. http://doi.org/10.1016/j.rser.2015.09.033

Song, S. L., Lee, J. H., & Chang, S. H. (2014). CHF enhancement of SiC nanofluid in pool boiling experiment. *Experimental Thermal and Fluid Science*, *52*, 12–18. http://doi.org/10.1016/j.expthermflusci.2013.08.008

Taylor, B. N., & Kuyatt, C. E. (1994). Guidelines for Evaluating and Expressing the Uncertainty of NIST Measurement Results. *National Institute of Standards and Technology Tech. Note*, (1297), 1–2. Retrieved from http://books.google.com/books?hl=en&lr=&id=xgJeJzsbhoAC&oi=fnd&pg=PA10&dq=Guidelines+for+Evaluating+and+Expressing+the+Uncertainty+of+NIST+Measurement+Results&ots=0nN8XOBf1X&sig=zz3STNxWVQJExIOlisM-GjhKMUg

Theofanous, T. G., Dinh, T. N., Tu, J. P., & Dinh, A. T. (2002). The boiling crisis phenomenon part II: Dryout dynamics and burnout. *Experimental Thermal and Fluid Science*, *26*(6–7), 793–810. http://doi.org/10.1016/S0894-1777(02)00193-0

Theofanous, T. G., Tu, J. P., Dinh, A. T., & Dinh, T. N. (2002). The boiling crisis phenomenon part I: Nucleation and nucleate boiling heat transfer. *Experimental Thermal and Fluid Science*, *26*(6–7), 775–792. http://doi.org/10.1016/S0894-1777(02)00192-9

Turgut, A., Tavman, I., Chirtoc, M., Schuchmann, H. P., Sauter, C., & Tavman, S. (2009). Thermal conductivity and viscosity measurements of water-based TiO2 nanofluids. *International Journal of Thermophysics*, *30*(4), 1213–1226. http://doi.org/10.1007/s10765-009-0594-2

Wang, L., Chen, H., & Witharana, S. (2013). Rheology of Nanofluids : A Review. *Recent Patents on Nanotechnology*, *7*, 232–246. http://doi.org/10.2174/18722105113079990003

Wenzel, R. N. (1986). Surface Roughness and Contact Angle. *Journal of Psychosomatic*

Research, *30*(3), 387. http://doi.org/10.1016/0022-3999(86)90018-8

Xu, Z. G., & Zhao, C. Y. (2013). Thickness effect on pool boiling heat transfer of trapezoid-shaped copper foam fins. *Applied Thermal Engineering*, *60*(1–2), 359–370. http://doi.org/10.1016/j.applthermaleng.2013.07.013

Yang, Y., Ji, X., & Xu, J. (2010). Pool boiling heat transfer on copper foam covers with water as working fluid. *International Journal of Thermal Sciences*, *49*(7), 1227–1237. http://doi.org/10.1016/j.ijthermalsci.2010.01.013

You, S. M., Kim, J. H., & Kim, K. H. (2003). Effect of nanoparticles on critical heat flux of water in pool boiling heat transfer. *Applied Physics Letters*, *83*(16), 3374. http://doi.org/10.1063/1.1619206

Zhang, Y. P., Qiu, S. Z., Su, G. H., & Tian, W. X. (2010). Analysis of safety margin of in-vessel retention for AP1000. *Nuclear Engineering and Design*, *240*(8), 2023–2033. http://doi.org/10.1016/j.nucengdes.2010.04.020

Zhong, D., Meng, J., Li, Z., & Guo, Z. (2015). International Journal of Heat and Mass Transfer Critical heat flux for downward-facing saturated pool boiling on pin fin surfaces, *87*, 201–211.

Zuber, N. (1959). *Hydrodynamic Aspects of Boiling Heat Transfer*. University of California.

Zuhairi Sulaiman, M., Takamura, M., Nakahashi, K., & Okawa, T. (2013). Boiling Heat Transfer and Critical Heat Flux Enhancement of Upward- and Downward-Facing Heater in Nanofluids. *Journal of Engineering for Gas Turbines and Power*, *135*(7), 72901. http://doi.org/10.1115/1.4023688

Nomenclature

A	the surface area of the heated surface
A_w	the contact area between honeycomb porous plate and heated the surface
C	the concentration of nanofluid
d_v	the width of vapor escapes channel in honeycomb porous plate
$f(\theta)$	the function of heater orientation in degree
g	acceleration due to gravity
h	the heat transfer coefficient
h_{fg}	latent heat of vaporization
K	permeability coefficient
L_{h}	heater size
L'	dimensionless heater length
P	pressure
R	ideal gas constant
S	thermal effusivity
q	heat flux
$q_{\mathrm{CHF,exp}}$	critical heat flux
$q_{\mathrm{CHF},0^\circ}$	critical heat flux at upward facing 0°
$q_{\mathrm{CHF,PS},\theta}$	critical heat flux of plain surface at heater orientation θ
$q_{\mathrm{CHF,Zuber}}$	critical heat flux obtained using Zuber's model

r_{eff}	the effective pore radius
T	temperature
t	time
V_p	the volume of liquid contained in honeycomb porous plate

Greek Symbols

β	static contact angle
δ	capillary length
δ_c	thickness of liquid macrolayer
δ_h	the height of honeycomb porous plate
δ_s	the wall thickness of honeycomb porous plate
ε	the porosity of honeycomb porous plate
ρ	density
τ_d	hovering period of coalesced bubble
λ_m	modulation wavelength
λ_c	Rayleigh-Taylor critical wavelength
λ_D	most dangerous wavelength
λ_H	Helmholtz instability wavelength
σ_{sv}	interfacial tension between solid and vapor
σ_{sl}	interfacial tension between solid and liquid
σ_{lv}	interfacial tension between liquid and vapor
$\dot{\gamma}$	shear rate
μ	viscosity

Subscripts

l	liquid

p	porous
sat	saturation
sub	subcooled
v	vapor

Acknowledgements

Firstly, I would like to express my sincere gratitude to my supervisors, Associate Prof. Shoji Mori and Prof. Kunito Okuyama for the continuous support of my Ph.D. study and related research, for their patience, motivation, and immense knowledge. Their guidance helped me in all the time of research and writing of this thesis. I could not have imagined having a better advisor and mentor for my Ph.D. study.

Besides my advisor, I would like to thank the rest of my thesis committee: Prof. Hitoshi Habuka, Prof. Meguru Kaminoyama, and Associate Prof. Kazuho Nakamura, for their insightful comments and encouragement to improve the thesis writing which incented me to widen my research from various perspectives.

I thank my fellows at the Okuyama and Mori Laboratory for the stimulating discussions especially colleagues in the same research theme group: Aduki Ogoshi, Osa Ryunosuke, Maruoka Naru, Sakakibara Fumiki, Imai Ryosuke, Yanagisawa Ryuta, Taira Takafumi, Yokomatsu Fumihisa, Kobayashi Satoshi, Muta Akihiro and Wilton Santos. All of you has always been a source of strength for me to overcome any difficulties in experimental works. Not to forget, YNU staffs: Mrs. Kojima, Mrs. Isono and everyone I have encountered during my candidacy for helping me in any process related.

Studying and living in Japan could not be possible without financial support. As such, I want to thank the Japanese government for the scholarship (Monbukagakusho Scholarship) I received here. Also, a special thank you to the International Islamic University Malaysia for the allowances to support my family here.

I am greatly indebted to all my Japanese and Malaysian friends in Kantou area mainly, for the friendship, helping hands and warm welcomes. I have truly enjoyed every time we have spent together. Also, I thank my friends in YOKOMS (Yokohama National University Muslim Society) for their support and encouragement during my hectic life in school. Not to forget all my friends in Malaysia and around the globe whom I seek advice or help to review my work during this journey.

I would like to express gratitude and appreciation to my beloved wife who is always on my side during ups and downs in this journey. Thank you for the all sacrifices you have made including bringing up our two wonderful kids. To my two adorable sons, Affan Nufail and Nazif Fawwaz, thank you for giving me strength and motivation to finish what I have started. Ayah loves you both very much and hopes both of you would excel in this life in any field that you wanted to pursue in and the hereafter.

Last but not the least, I would like to say thank you to my parents (Mt Aznam Bin Kasim and Suriana Binti Abdul Salim) and my parents-in-law (Abdullah Bin Haji Zakaria and Besah@Natrah Binti Wan Husin) for your prayers, my siblings for supporting me spiritually throughout writing this thesis and my life in overall.